MUELLER CHARACTERIZATION FOR PARTIAL POLARIMETRY

by

Quinn Tyler Jarecki

_____

A Dissertation Submitted to the Faculty of the

JAMES C. WYANT COLLEGE OF OPTICAL SCIENCES

In Partial Fulfillment of the Requirements
For the Degree of

DOCTOR OF PHILOSOPHY
WITH A MAJOR IN OPTICAL SCIENCE

In the Graduate College

THE UNIVERSITY OF ARIZONA

2024

THE UNIVERSITY OF ARIZONA
· GRADUATE COLLEGE

As members of the Dissertation Committee, we certify that we have read the dissertation prepared by **Quinn Tyler Jarecki**, titled *Mueller Characterization for Partial Polarimetry,* and recommend that it be accepted as fulfilling the dissertation requirement for the Degree of Doctor of Philosophy.
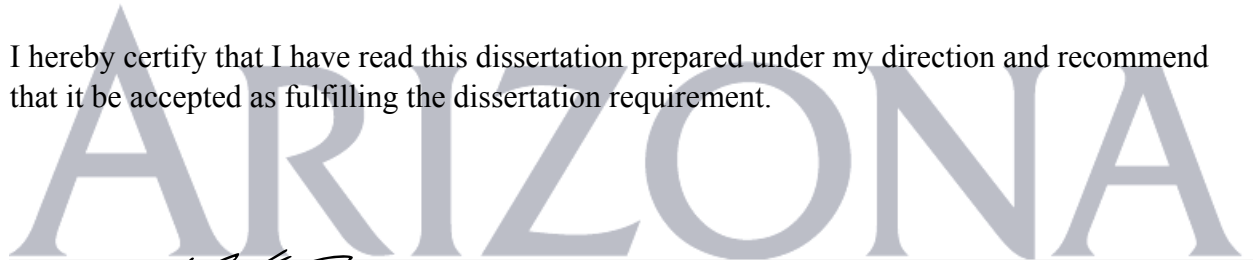
_____ Date: _____
Professor Meredith K. Kupinski

_____ Date: __5/8/2024___
Professor Stanley K. H. Pau

_____Russell A. Chipman_____ Date: __5/8/2024_____
Professor Russell A. Chipman

Final approval and acceptance of this dissertation is contingent upon the candidate's submission of the final copies of the dissertation to the Graduate College.

I hereby certify that I have read this dissertation prepared under my direction and recommend that it be accepted as fulfilling the dissertation requirement.

_____ Date: _____
Professor Meredith K. Kupinski
Dissertation Committee Chair
Wyant College of Optical Sciences

ACKNOWLEDGEMENTS

LAND ACKNOWLEDGEMENT

The work contained in this dissertation was conducted on the land and territories of Indigenous peoples. Today, Arizona is home to 22 federally recognized tribes, and an unknown number of tribes which remain federally unrecognized. Tucson and the University of Arizona exist on the land of the Tohono O'odham and the Yaqui.

As a person whose work has benefited from the University of Arizona Land-Grant Institution, I recognize that these efforts were done on land which was stolen from Indigenous peoples who have cared for and inhabited these spaces in perpetuity. It is my hope and must be our sincere and collective action to prioritize reflection on this history of displacement and wrongdoing, and the enduring legacy of Indigenous peoples – past, present, and future.

DEDICATION

To my family, friends, and vending machines who supported me and made it so that actually doing the research was the only hard part.

TABLE OF CONTENTS

TABLE OF CONTENTS – *Continued*

TABLE OF CONTENTS – *Continued*

LIST OF FIGURES

LIST OF FIGURES – *Continued*

LIST OF TABLES

ACRONYMS

DoP degree of polarization

AoLP angle of linear polarization

MM Mueller matrix

JM Jones matrix

MJM Mueller-Jones matrix

PSG polarization state generator

PSA polarization state analyzer

TD triple degenerate

DRR dual-rotating-retarder

DoFP division-of-focal-plane

COTS commercial-off-the-shelf

pBRDF polarized bidirectional distribution function

RMSD root-mean-squared-deviation

ABSTRACT

Polarization carries information about the geometry, texture, and material of a light-matter interaction beyond what is available through purely radiometric measurements. This information is contained in the Mueller matrix (MM) for a linear light-matter interaction. Characterizing the complete MM requires a minimum of 16 linearly independent polarization measurements, though more measurements are commonly performed for improved robustness to measurement noise. However, limiting the quantity of polarization measurements can reduce complexity, cost, time, and thereby make polarization information accessible to broader applications. This dissertation explores the utilization of *a priori* knowledge of the subset of MMs that will be measured in a given application for the purpose of designing effective partial polarimeters. This *a priori* information can come in the form of an initial MM characterization of the exact scene to be measured again later or as a more general representation of the polarized scattering response of a material.

The contributions of this doctoral research are enumerated below:

1. Optimization of polarization generator and analyzer states for maximizing contrast in polariscopic images of birefringent targets which is demonstrated on *in vivo* human eyes,

2. A method for efficiently acquiring and representing empirical MM data as a function of scattering geometry which requires 37% fewer goniometric measurements and stores 3 times fewer MMs per wavelength than the state-of-the-art,

3. An original polarized scattering model which both decouples depolarization and mixes first-surface with diffuse polarized reflection as a function of scattering geometry, with an average diattenuation orientation error of $10.9°$ and magnitude error of 8.3% when compared to measured data, and

4. A partial polarimetric method for estimating depolarization magnitude and extrapolating MM, which resulted in an average error in depolarization magnitude of 7.6%

and simulated polarimetric measurement error of 6.0% despite a $10\times$ reduction in number of measurements.

These contributions represent different efforts to reduce some of the complexities of polarimetric imaging. Through these simplifications, insights from polarimetric information may be more easily accessed in a variety of applications.

CHAPTER 1

Introduction

Like wavelength and brightness, polarization is a fundamental physical property of light. The polarization of light is the preferential direction of oscillation of the electric field vector. Therefore, the polarization carries directional information about the source and subsequent light-matter interactions. Polarization measurements of light-matter interactions can provide information about the geometry, shape, and texture of a material beyond what is available from radiometry alone. A complete characterization of a polarized light-matter interaction requires a full Mueller matrix (MM) measurement. However, when MM imaging is prohibitively complex, expensive, or even unnecessary, partial polarimetry (*i.e.*, fewer than 16 measurements) can be used to extract useful polarimetric information. If some amount of information is known *a priori* about the subset of MMs to be measured, it becomes possible to compare different partial polarimeter designs. In this dissertation, the substantial contributions from three peer-reviewed publications and one prepared publication regarding polarimetric characterization and partial polarimetry are presented. In Chapter 2, the foundational physics and mathematical formalisms utilized in the work are discussed. The subsequent chapters demonstrate different applications of Chapter 2.

In Chapter 3, a method for determining the optimal polarized illumination and analysis states to maximize contrast in a spatially varying birefringent target is presented. Contrast is defined as the difference in measured irradiance between two regions of interest. This method is demonstrated by performing optimizations using initial MM imaging of *in vivo* human eyes. The eye MM image acquisition takes place over 15 seconds during which the eye may be subject to random unconscious movements. These small movements are what motivate the development of a partial polarimeter with snapshot operation. MM imaging shows that the birefringent cornea exhibits spatially-varying patterns of retardance exceeding half of a wave with a fast-axis varying from linear, to circular, and intermediate

elliptical states. Based on the retardance found during MM characterization, polariscopic pairs of polarization state generator (PSG) and polarization state analyzer (PSA) states are optimized for maximizing contrast. The closed-form solution for optimal contrast is general for any two pure retarder MMs. For a pair of retarder MMs, there is a family of PSG/PSA solutions that maximize contrast. This range of solutions creates an opportunity to use a distance metric on the as a criterion to adjust polarimetric hardware architecture. The optimization approach is demonstrated by performing both Mueller and polariscopic imaging of an *in vivo* human eye at 947 nm using a dual-rotating-retarder (DRR) polarimeter. Polariscopic images are simulated from Mueller measurements of 19 other human subjects to test the robustness of this optimal solution.

In Chapter 4, a original representation of empirical isotropic polarized bidirectional distribution function (pBRDF) is introduced to improve the efficiency of parameterization and acquisition so that extensive material libraries can become readily-available. Performing Mueller measurements at many scattering geometries and wavebands requires considerable acquisition time and storage resources. Isotropic pBRDFs are parameterized by three angles from the coordinate system introduced by Rusinkiewicz. This work introduces a cylindrical, rather than Cartesian, interpretation of the Rusinkiewicz angles to tabulate scattering geometries. The advantages of discrete cylindrical pBRDF tabulation are compactness and increased convexity. There is a factor of three reduction in the quantity of pBRDF samples in the cylindrical compared to Cartesian tabulation. No information is lost in the pBRDF cylindrical table because only non-physical and redundant geometries are excluded. The convexity, which is desirable for interpolation, is increased from 67.3% to 85.7%. The compact representation is then used to determine an efficient set of goniometric camera positions at which to sample the pBRDF of a sphere. The percentage of discrete geometries which are sampled at least once is used as a figure of merit to compare goniometric sets. For the particular size of sphere and camera parameters of our polarimeter, there are diminishing returns on fill percentage after 92 goniometer positions, where 82% of the discrete geometries are sampled. This optimized pBRDF sampling and tabulation was performed for a 3D printed sphere and the cylindrical coordinate representation is used to visualize the pBRDF as a function of scattering geometry.

In Chapter 5, analytic pBRDF models are discussed, including a original model which combines specular and diffuse polarization scattering. First-surface Fresnel reflection, diffuse partial polarization, and ideal depolarization are popular terms used in closed-form pBRDF representations. The relative contributions of these terms are highly dependent on material, albedo/wavelength, and scattering geometry. Complicating matters further, current pBRDF representations incoherently combine MM for Fresnel and polarized diffuse terms which couples into depolarization. In this work, a closed-form pBRDF representation is introduced where first-surface Fresnel reflection and diffuse polarization are coherently combined using Jones calculus to avoid affecting depolarization. This new pBRDF has only six physically meaningful parameters: the scalar-valued depolarization parameter and average reflectance which are geometry-dependent and four geometry-independent material constants. The model demonstrates performance to predict MM image measurements of a sphere and a Stanford bunny at different geometries and wavebands. The RMSD in diattenuation orientation for the modeled versus measured averaged over acquisition geometry was 7.49° and 14.29° at 451 nm (low albedo) and 662 nm (high albedo), respectively. The RMSD in diattenuation magnitude averaged over acquisition geometry was 4.96% at 451 nm and 11.73% at 662 nm.

In Chapter 6, a method for linear estimation of depolarization magnitude from four polarization measurements is presented. The linear estimator is based on an assumption of a triple degenerate (TD) depolarization structure of the material and makes use of the pBRDF models from the previous Chapter. A TD MM assumption reduces the degrees of freedom from sixteen to eight: one for reflectance, six for non-depolarizing properties, and one for depolarization. When the non-depolarizing dominant process is known or assumed, the degrees of freedom are further reduced to two. For a given material, if the TD model is appropriate and the dominant non-depolarizing process is known, then these two degrees of freedom can be estimated from as few as two polarimetric measurements. Thus, the MM can be extrapolated from a reduced number of measurements. MM extrapolations from single snapshot acquisitions with a Sony Triton 5.0MP Polarization Camera are performed at 30 acquisition geometries and two wavelengths on an ensemble of LEGO bricks treated to have varying surface roughness. Averaged over 30 geometries,

the simulated polarimetric measurement error mean and mode are 11.06% and 1.03%, respectively, despite a $10\times$ reduction in the number of polarimetric measurements. For a 3D printing material, using the mixed polarization model to estimate depolarization magnitude resulted in RMSD values of 11.11% at 451 nm and 4.24% at 662 nm.

CHAPTER 2

Polarization and Polarimetry

2.1 Jones Calculus

Light is an electromagnetic wave which propagates through space and time. The direction in which the electric field component preferentially oscillates is known as the polarization of light. The electric field vector of a monochromatic plane wave,

$$\mathbf{E}(\mathbf{r}, t) = \mathrm{Re}\left\{\mathbf{E}_0 \exp\left[i\left(\frac{2\pi}{\lambda}\widehat{\mathbf{k}} \cdot \mathbf{r} - \omega t - \phi_0\right)\right]\right\}, \tag{2.1}$$

has a well-defined complex polarization vector $\mathbf{E}_0 = (E_{0,x}, E_{0,y}, E_{0,z})$, which is perpendicular to the propagation vector $\widehat{\mathbf{k}} = (k_x, k_y, k_z)$. The plane which contains $\mathbf{E}$ (and is perpendicular to $\widehat{\mathbf{k}}$) is known as the transverse plane. The electric field varies as a function of position $\mathbf{r} = (x, y, z)$ and time t based on its angular frequency ω, wavelength λ, and a constant phase offset ϕ_0.

When rotated into a coordinate system where $\widehat{\mathbf{k}} = (0, 0, 1)$, $\mathbf{E}_0$ is constrained to be in the x-y plane. In this case, $E_{0,z}$ must be zero and the polarization vector can be reduced to a 2×1 Jones vector. The transformation of polarization state is described with a 2×2 complex-valued matrix Jones matrix $\mathbf{J}$,

$$\mathbf{E}_0' = \mathbf{J}\mathbf{E}_0 = \begin{bmatrix} j_{xx} & j_{xy} \\ j_{yx} & j_{yy} \end{bmatrix} \begin{bmatrix} E_{0,x} \\ E_{0,y} \end{bmatrix}. \tag{2.2}$$

The matrix for the rotation of a polarization element or rotation of the transverse plane is simply the 2×2 rotation matrix,

$$\mathbf{R}(\alpha) = \begin{bmatrix} \cos(\alpha) & -\sin(\alpha) \\ \sin(\alpha) & \cos(\alpha) \end{bmatrix}, \tag{2.3}$$

where α is the angle of counter-clockwise rotation.

The polarization-dependence of reflection at the first surface of a material is given by the Fresnel reflection coefficients,

$$r_s(n, \theta_d) = \frac{\cos(\theta_d) - n\sqrt{1 - \frac{\sin^2(\theta_d)}{n^2}}}{\cos(\theta_d) + n\sqrt{1 - \frac{\sin^2(\theta_d)}{n^2}}}, \quad r_p(n, \theta_d) = \frac{n\cos(\theta_d) - \sqrt{1 - \frac{\sin^2(\theta_d)}{n^2}}}{n\cos(\theta_d) + \sqrt{1 - \frac{\sin^2(\theta_d)}{n^2}}}, \quad (2.4)$$

where θ_d is the angle of incidence onto the surface and n is the ratio of the effective refractive index of the material to the index of the incident medium. The subscript s refers to s-polarization, which is perpendicular to both the incident propagation vector $\widehat{\mathbf{k}}$ and the plane of incidence which is spanned by $\widehat{\mathbf{k}}$ and the surface normal vector $\widehat{\mathbf{n}}$. The subscript p refers to p-polarization which is perpendicular to $\widehat{\mathbf{k}}$ and $\widehat{\mathbf{s}}$. Further details regarding the s- and p-polarization basis vectors are provided in Appendix A. For homogeneous, isotropic dielectric surfaces, r_s has a larger magnitude than r_p, so first-surface reflections tend to be s-polarized.

2.2 Mueller Calculus

2.2.1 Stokes Vectors

For polarization analysis of optical systems, Jones calculus (and its 3D extensions) are used.[2,15,18,109–111] However, in everyday environments which more often feature polychromatic, incoherent, and/or partially polarized light, Jones calculus is insufficient. Instead, the polarization state of light is described by a 4×1 real-valued Stokes vector. The elements of the Stokes vector have phenomenological definitions based on sums and differences of polarimetric measurements P

$$\mathbf{S} = \begin{bmatrix} P_H + P_V \\ P_H - P_V \\ P_{45} - P_{135} \\ P_R - P_L \end{bmatrix} = \begin{bmatrix} S_0 \\ S_1 \\ S_2 \\ S_3 \end{bmatrix} = S_0 \begin{bmatrix} 1 \\ s_1 \\ s_2 \\ s_3 \end{bmatrix}. \quad (2.5)$$

where S_0 is the total flux, S_1 is the difference in horizontally and vertically polarized measurements, S_2 is the difference in 45° and 135° polarized measurements, and S_3 is the
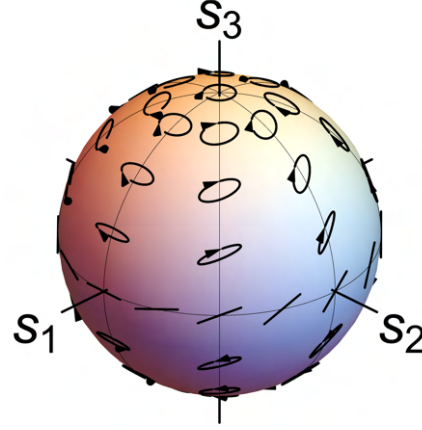
Figure 2.1: The Poincaré sphere with fully polarization states shown on the surface. The Poincaré sphere is a geometric representation of normalized Stokes vectors.

difference in right and left circularly polarized measurements. Polarimetric measurements are elaborated on in Sect. 2.3.1. On the right-hand side of Eq. 2.5, S_0 has been factored out to produce a normalized Stokes vector. The triplet (s_1, s_2, s_3) can be interpreted as a Cartesian point in 3D. The set of (s_1, s_2, s_3) for physically realizable normalized Stokes vectors is called the Poincaré sphere, shown in Fig. 2.1. On the Poincaré sphere, circular states exist at the poles and linear states exist along the equator. Elliptical states exist between the equator and the poles. The degree of polarization, DoP, describes whether a Stokes vector represents fully polarized, partially polarized, or unpolarized light and is calculated

$$DoP = \frac{\sqrt{S_1^2 + S_2^2 + S_3^2}}{S_0}. \tag{2.6}$$

The DoP ranges from 0 to 1, where 0 corresponds to unpolarized light and 1 is fully polarized light. Fully polarized states exist on the surface of the Poincaré sphere, partially polarized states exist within the sphere, and unpolarized light is represented by the center of the sphere. The orientation of linear polarization is described by the angle of linear polarization, $AoLP$, and is calculated

$$AoLP = \frac{1}{2} \arctan\left(\frac{S_2}{S_1}\right). \tag{2.7}$$

For elliptically polarized light, the $AoLP$ corresponds to the orientation of the major axis of the ellipse.

2.2.2   Mueller Matrices

The linear transformation of a Stokes vector upon interaction with a medium is described by a 4×4 real-valued MM written as

$$\mathbf{M} = \begin{bmatrix} M_{00} & M_{01} & M_{02} & M_{03} \\ M_{10} & M_{11} & M_{12} & M_{13} \\ M_{20} & M_{21} & M_{22} & M_{23} \\ M_{30} & M_{31} & M_{32} & M_{33} \end{bmatrix} = M_{00} \begin{bmatrix} 1 & m_{01} & m_{02} & m_{03} \\ m_{10} & m_{11} & m_{12} & m_{13} \\ m_{20} & m_{21} & m_{22} & m_{23} \\ m_{30} & m_{31} & m_{32} & m_{33} \end{bmatrix}. \tag{2.8}$$

From the sixteen matrix elements, sixteen degrees of freedom that are associated with physical quantities can be calculated: one for average throughput, three for diattenuation, three for retardance, and nine for depolarization.[14,17] In the right-hand side of Eq. 2.8, the average reflectance M_{00} is factored out to normalize the MM. This is routinely performed when the value of M_{00} is much larger than the other matrix elements in order to decouple polarimetric behavior from purely radiometric behavior for analysis. Polarization transformations via diattenuation, retardance, and/or depolarization are used to relate polarimetric measurements to the physical properties of objects such as texture, albedo, and geometry.[47,67]

Diattenuation describes the polarization-dependence of the reflectance and is calculated from elements in the top row of the MM. Diattenuation magnitude is calculated as $D = \sqrt{M_{01}^2 + M_{02}^2 + M_{03}^2}/M_{00}$ and linear diattenuation orientation is calculated as $\psi = 1/2 \arctan(M_{02}/M_{01})$. When an optical element has $D = 1$, it is referred to as a polarizer. The MM for a linear polarizer oriented at ψ is given by

$$\mathbf{M}_{LP}(\psi) = \frac{1}{2} \begin{bmatrix} 1 & \cos(2\psi) & \sin(2\psi) & 0 \\ \cos(2\psi) & \cos^2(2\psi) & \sin(2\psi)\cos(2\psi) & 0 \\ \sin(2\psi) & \sin(2\psi)\cos(2\psi) & \sin^2(2\psi) & 0 \\ 0 & 0 & 0 & 1 \end{bmatrix} \tag{2.9}$$

Retardance describes the polarization-dependence of phase. Practically, this results in a transformation of polarization without changing the total amount of light, S_0, or DoP.

The MM for a pure elliptical retarder is given by

$$\mathbf{M}_{ER}(\vec{\boldsymbol{\delta}}) = \begin{bmatrix} 1 & 0 & 0 & 0 \\ 0 & \frac{\delta_H^2+(\delta_{45}^2+\delta_R^2)C}{\delta^2} & \frac{\delta_{45}\delta_H T}{\delta^2} + \frac{\delta_R S}{\delta} & \frac{\delta_H \delta_R T}{\delta^2} - \frac{\delta_{45} S}{\delta} \\ 0 & \frac{\delta_{45}\delta_H T}{\delta^2} - \frac{\delta_R S}{\delta} & \frac{\delta_{45}^2+(\delta_R^2+\delta_H^2)C}{\delta^2} & \frac{\delta_R \delta_{45} T}{\delta^2} + \frac{\delta_H S}{\delta} \\ 0 & \frac{\delta_H \delta_R T}{\delta^2} + \frac{\delta_{45} S}{\delta} & \frac{\delta_R \delta_{45} T}{\delta^2} - \frac{\delta_H S}{\delta} & \frac{\delta_R^2+(\delta_{45}^2+\delta_H^2)C}{\delta^2} \end{bmatrix} = \begin{bmatrix} 1 & \vec{\mathbf{0}}^{\intercal} \\ \vec{\mathbf{0}} & \mathbf{V}(\vec{\boldsymbol{\delta}}) \end{bmatrix}, \quad (2.10)$$

where $\vec{\boldsymbol{\delta}} = [\delta_H, \delta_{45}, \delta_R]$, $\delta = |\vec{\boldsymbol{\delta}}|$, $C = \cos(\delta)$, $S = \sin(\delta)$, and $T = 1 - \cos(\delta)$. Retarder vector elements δ_H, δ_{45}, and δ_R are the components of retardance for each of the Stokes basis states. In the right-hand side of Eq. 2.10, $\vec{\mathbf{0}}$ is a 3×1 vector of zeros and the lower-right 3×3 elements of the MM are written as a unitary matrix $\mathbf{V}(\vec{\boldsymbol{\delta}})$.

Depolarization is the randomization of polarization state with respect to position, angle, time, and/or wavelength that is unresolvable to the particular detector in use.[9] This results in a decrease in the DoP calculated in Eq. 2.6. The ideal depolarizer, which reduces the DoP of every polarization state to zero, has the MM

$$\mathbf{M}_{ID} = \begin{bmatrix} 1 & 0 & 0 & 0 \\ 0 & 0 & 0 & 0 \\ 0 & 0 & 0 & 0 \\ 0 & 0 & 0 & 0 \end{bmatrix}. \quad (2.11)$$

For partially depolarizing MMs, depolarization is coupled among the Mueller elements so it is not easily extracted. Therefore, several MM decomposition techniques, such as the Lu-Chipman decomposition, matrix roots, and integral decomposition, exist. There are also several depolarization summary metrics, such as the depolarization index, average degree of polarization, and the coherency eigenvalues.[16,31,59,68,69,73,75] The MMs studied in the work presented are all strongly depolarizing. As depolarization increases, a first-order depolarization approximation becomes appropriate. Therefore, this dissertation employs such an approximation to reduce the degrees of freedom for depolarization from nine to one. This enables several partial polarimetric analyses. This approximation is called the triple-degenerate assumption and is discussed in the following section.

2.2.3 Triple-Degenerate Mueller Matrices

The eigenvectors of a MM do not strictly correspond to physical Stokes parameters. Instead, eigenanalysis is performed on the linearly-related coherency matrix.[20–22, 42, 46, 87, 88] The coherency matrix $\mathbf{C}$ is calculated from the MM by

$$\mathbf{C} = \frac{1}{2} \sum_{i,j=0}^{3} M_{ij} \mathbf{U} \left[\boldsymbol{\sigma}_i \otimes \boldsymbol{\sigma}_j^* \right] \mathbf{U}^\dagger \qquad (2.12)$$

where M_{ij} are the elements of $\mathbf{M}$, $\boldsymbol{\sigma}_i$ and $\boldsymbol{\sigma}_j$ are the Pauli spin matrices,

$$\boldsymbol{\sigma}_0 = \begin{bmatrix} 1 & 0 \\ 0 & 1 \end{bmatrix}, \boldsymbol{\sigma}_1 = \begin{bmatrix} 1 & 0 \\ 0 & -1 \end{bmatrix}, \boldsymbol{\sigma}_2 = \begin{bmatrix} 0 & 1 \\ 1 & 0 \end{bmatrix}, \boldsymbol{\sigma}_3 = \begin{bmatrix} 0 & -i \\ i & 0 \end{bmatrix}, \qquad (2.13)$$

and the $\mathbf{U}$ matrix is given by

$$\mathbf{U} = \frac{1}{\sqrt{2}} \begin{bmatrix} 1 & 0 & 0 & 1 \\ 1 & 0 & 0 & -1 \\ 0 & 1 & 1 & 0 \\ 0 & i & -i & 0 \end{bmatrix}. \qquad (2.14)$$

The elements of each of the four eigenvectors of the coherency matrix, $\mathbf{c}_n$, can be used to calculate a Jones matrix

$$\begin{aligned} \mathbf{J}_n &= \begin{bmatrix} c_{n,0} + c_{n,1} & c_{n,2} - ic_{n,3} \\ c_{n,2} + ic_{n,3} & c_{n,0} - c_{n,1} \end{bmatrix} \\ &= c_{n,0}\boldsymbol{\sigma}_0 + c_{n,1}\boldsymbol{\sigma}_1 + c_{n,2}\boldsymbol{\sigma}_2 + c_{n,3}\boldsymbol{\sigma}_3. \end{aligned} \qquad (2.15)$$

These Jones matrices can then in turn be used to calculate their equivalent MMs

$$\widehat{\mathbf{M}}_n = \mathbf{U} \left(\mathbf{J}_n \otimes \mathbf{J}_n^* \right) \mathbf{U}^{-1}. \qquad (2.16)$$

A MM with an equivalent Jones matrix is referred to as a Mueller-Jones matrix (MJM), and has no depolarization. MJMs are differentiated from depolarizing MMs with the hat notation $\widehat{\cdot}$. The four MJMs calculated from the four eigenvectors form an orthonormal basis set for the original depolarizing MM,

$$\mathbf{M} = \sum_{n=0}^{3} \xi_n \widehat{\mathbf{M}}_n, \qquad (2.17)$$
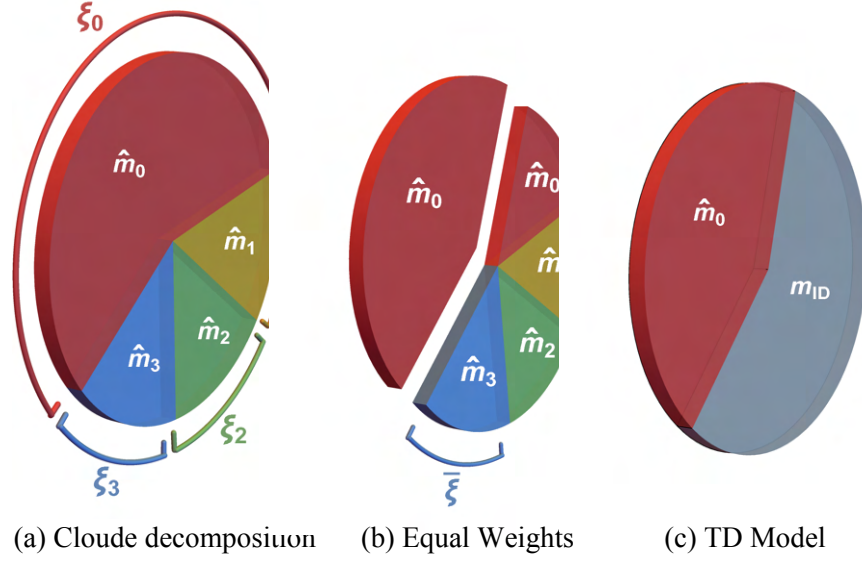
Figure 2.2: Visualization of expressing a MM with a TD model. In (a), a depolarizing light-matter interaction is decomposed into a convex sum of four non-depolarizing MJMs. The sum is a parallel decomposition, so it is depicted as a pie-chart with four wedges that represent the four MJMs. The size of each wedge corresponds to the coherency eigenvalues that control the weights in the convex sum. In (b), it is assumed that $\xi_1 = \xi_2 = \xi_3 = \overline{\xi}$ (a triple-degeneracy) so $\widehat{\mathbf{m}}_1$, $\widehat{\mathbf{m}}_2$, and $\widehat{\mathbf{m}}_3$ have equally-sized wedges in the pie-chart. A portion of $\widehat{\mathbf{m}}_0$ equal to $\overline{\xi}$ is separated from ξ_0. In (c), the property of the Cloude decomposition that an equal sum of the four MJMs results in the ideal depolarizer is used to write the original sum as one MJM plus the ideal depolarizer.

where the weights in the sum, ξ_n, are the eigenvalues of the coherency matrix ordered from largest to smallest. This is known as the Cloude spectral decomposition.[20,22] When the eigenvalues are normalized such that $\sum_{n=0}^{3} \xi_n = 1$ (equivalent to the normalization in the right-hand side of Eq. 2.8), each eigenvalue ξ_n represents the fraction of light which is transformed by the MJM $\widehat{\mathbf{M}}_n$ as shown in Fig. 2.2a. The set of four MJMs in this decomposition are orthonormal in the sense that $\frac{1}{2}\mathrm{tr}(\mathbf{J}_n^{\dagger}\mathbf{J}_m) = \delta_{nm}$ and $\frac{1}{4}\sum_{n=0}^{3} \widehat{\mathbf{M}}_n = \mathbf{M}_{ID}$.

A useful special case of the Cloude spectral decomposition is for a TD eigenspectrum ($\xi_1 = \xi_2 = \xi_3 = \overline{\overline{\xi}}$), where $\overline{\overline{\xi}} = (1-\xi_0)/3$ as in Fig. 2.2b. In the TD case, the depolarizing MM can be written as the convex sum of a MJM and an ideal depolarizer

$$\mathbf{M} = \frac{4M_{00}}{3}\left[\left(\xi_0 - \frac{1}{4}\right)\widehat{\mathbf{M}}_0 + (1 - \xi_0)\,\mathbf{M}_{ID}\right], \tag{2.18}$$

where ξ_0 is the largest eigenvalue, $\widehat{\mathbf{M}}_0$ is the dominant MJM, and $\mathbf{M}_{ID}$ is the ideal depolarizer from Eq. 2.11. The model in Eq. 2.18 is represented by the pie chart in Fig. 2.2c. The TD model is also a special case of the integral decomposition of a MM.[73]

In a TD-MM model, the degrees of freedom are reduced from sixteen to eight: one for throughput, one for depolarization ξ_0, and six for the dominant MJM $\widehat{\mathbf{M}}_0$ which describes the diattenuation and retardance. The single degree of freedom for the magnitude of depolarization is ξ_0, which controls the relative weight between an ideal depolarizer and a MJM in Eq. 2.18. The largest eigenvalue is bounded in the range $0.25 \leq \xi_0 \leq 1.0$, where $\xi_0 = 0.25$ means the MM is the ideal depolarizer and $\xi_0 = 1.0$ means the MM is a MJM. In a TD-MM model, the depolarization index DI is monotonically related to ξ_0 by the equation $DI = (4\xi_0 - 1)/3$. Diattenuation and retardance orientations match those of $\widehat{\mathbf{M}}_0$ and are invariant to ξ_0. The maximum diattenuation and retardance magnitudes in a TD-MM match those of $\widehat{\mathbf{M}}_0$ when $\xi_0 = 1$, but are reduced as ξ_0 approaches 0.25 where $\mathbf{M}_{ID}$ dominates the sum.

2.3 Polarization Imaging

2.3.1 Polarimetric Measurement Equation

For a sample described by $\mathbf{M}$, the measured irradiance from the nth polarimetric measurement is

$$P_n = \mathbf{a}_n^\dagger \mathbf{M} \mathbf{g}_n = \mathbf{w}_n \mathbf{m}, \tag{2.19}$$

where $\mathbf{w}_n = \mathbf{a}_n \otimes \mathbf{g}_n^\dagger$ and $\mathbf{m}$ is the 16×1 vector of the MM elements. For each n of N measurements, these states are used to calculate $\mathbf{w}_n$ which are then used as the rows of the polarimetric measurement matrix $\mathbf{W}$. The measurement matrix, $\mathbf{W}$, can be derived by fitting calibration measurements to MM models of the PSG and PSA or by using the eigenvalue calibration method which does not require a prior model.[14,23] The psuedoinverse of the measurement matrix, $\mathbf{W}^+$, is applied to the vector of N polarimetric measurements $\mathbf{P}$ to reconstruct an estimate of the MM elements $\widetilde{\mathbf{m}} = \mathbf{W}^+ \mathbf{P}$, where the tilde $\widetilde{\cdot}$ is used to indicate an estimated quantity. This calculation is performed at each pixel of the image taken at each goniometer position.

The pseudoinverse is chosen as the reconstruction algorithm because it provides the minimum-norm least squares solution to Eq. 2.19. This matrix-vector product is performed pixel-wise to form a MM image. The condition number, defined as the ratio of the largest to the smallest singular value, of $\mathbf{W}$ is used as a metric for the performance of a polarimeter.[89, 100, 102]

2.3.2 Partial and Complete Polarimetry

For a general MM, $\mathbf{W}$ must be rank sixteen to perform a complete reconstruction. This dissertation work makes use of a DRR Mueller polarimeter, shown in Fig. 2.3, called the RGB950.[5, 58] The RGB950 operates at four wavebands: 662 ± 11 nm, 524 ± 17 nm, 451 ± 19 nm, and 947 ± 20 nm. It is a DRR polarimeter as shown in Fig. 2.3a, where the PSG consists of a light source, a fixed linear polarizer and a rotating linear retarder (see Eqs. 2.9 and 2.10). The PSA consists of a rotating linear retarder followed by a fixed linear polarizer and the detector. The RGB950 typically performs 40 polarimetric measurements n with different PSG and PSA states, producing a measurement matrix, $\mathbf{W}_{40}$. For the eye measurements in Chapter 3, this was reduced to 25 measurements. These measurement matrices are overdetermined for MM polarimetry.

In this dissertation, partial polarimetry refers to a system which performs fewer than 16 linearly independent polarimetric measurements. This definition would include full Stokes polarimetry, which involves only four linearly independent polarimetric measurements. Partial polarimetry can be employed effectively when fewer than 16 degrees of freedom are needed for a particular application.[70, 71, 82] Two partial polarimeters are used in this work. The first is simply the RGB950 set to take fewer than 16 measurements. Using the RGB950 in this way as a partial polarimeter has the benefit of self-consistency when comparing MM image results to partial polarimetric results. The second partial polarimeter is a commercial-off-the-shelf (COTS) Sony Triton 5.0MP Polarization Camera shown in Fig. 2.3e. The Sony polarization camera is a division-of-focal-plane (DoFP) polarimeter. This camera has an array of micropolarizers in front of the detector elements so 4 polarimetric measurements (three of which are linearly-independent) are taken simultaneously at the cost of spatial resolution. This results in a measurement matrix $\mathbf{W}_4$. The

rank of this matrix is three, making it underdetermined for full Mueller polarimetry, but potentially suitable for partial polarimetric experiments.

(a) RGB950 polarimeter schematic

(b) RGB950 eye measurement

(c) RGB950 orange ball measurement

(d) LEGO bricks Mueller measurement

(e) LEGO bricks Stokes measurement
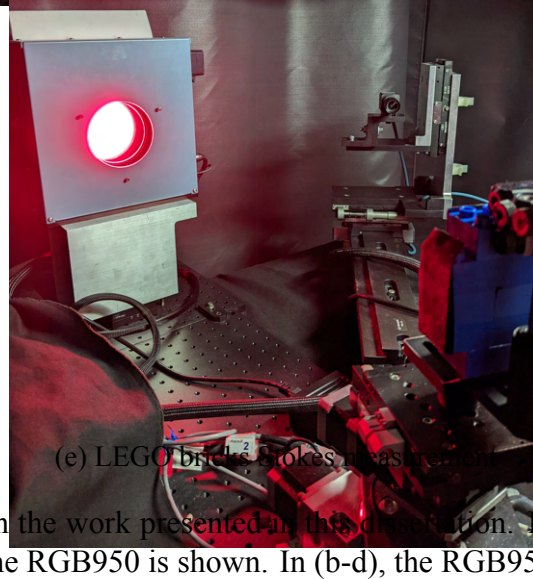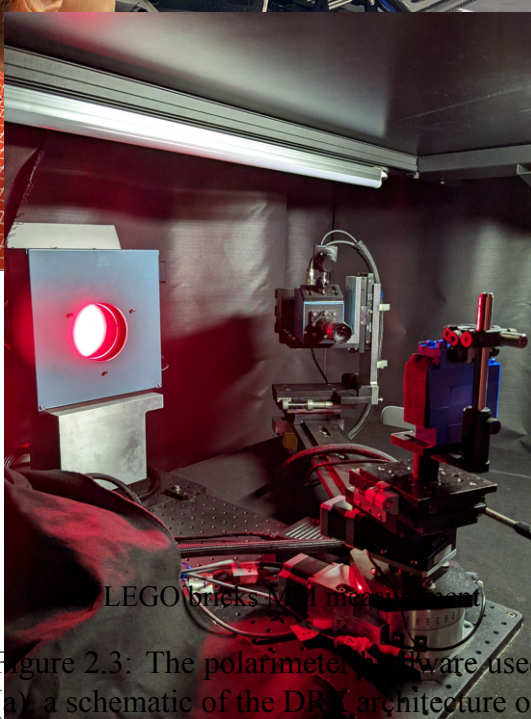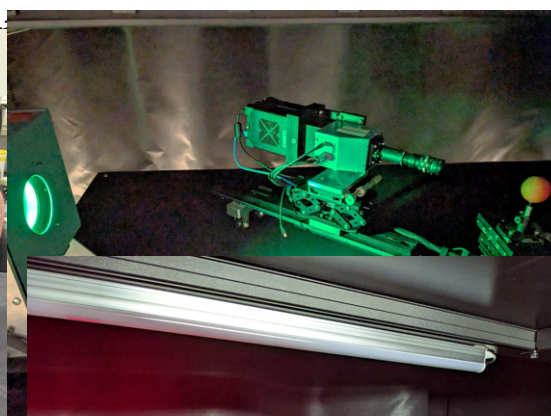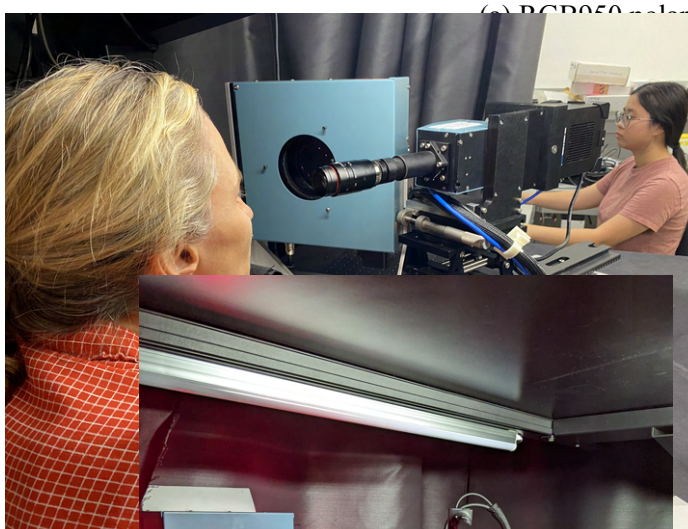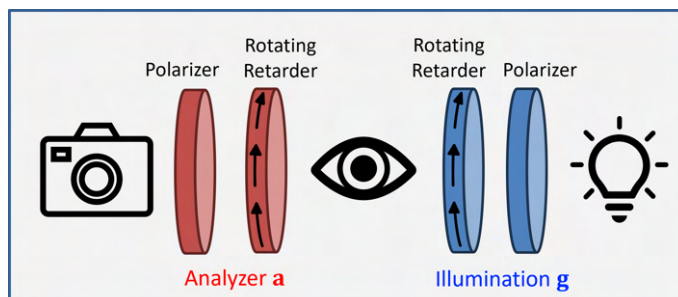
Figure 2.3: The polarimeters/software used in the work presented in this dissertation. In (a), a schematic of the DRR architecture of the RGB950 is shown. In (b-d), the RGB950 is shown performing measurements. In (e), the RGB950 camera is replaced with a Stokes camera for partial polarimetry.

CHAPTER 3

Polariscopic Measurement of Birefringent Samples

3.1   Polariscopic Imaging

The simplest sample-measuring partial polarimeter is a polariscope, where an object is illuminated by a fixed PSG and imaged through another, generally differently oriented, fixed PSA. polariscopic measurements are commonly used for analyzing birefringence in crystals, stress induced by the photoelastic effect in transparent materials, and the concentration of chiral molecules in liquids.[14]

Methods for numerical optimization of the PSG and PSA can be found in the literature.[33,49] For example, an analytic solution for optimizing the contrast in polariscopic measurements between an object and its background has been studied.[104] Upadhyay et al. analyzed the PSG and PSA for MMs with the same retarder fast-axis but varying retardance magnitude and for MMs with the same diattenuation magnitude but varying diattenuation orientation. They point out that optimal PSG states are those which have maximal separation on the Poincaré sphere after the light-matter interaction. Specifically, they found that for retarder MMs which vary in only in retardance magnitude, the set of optimal PSG states exist along a great circle on the Poincaré sphere. The approach presented in this Chapter is consistent with their findings, but is generalized for application to any pair of retarder MMs which vary in retardance magnitude, orientation, or both.

3.2   Human Eyes as Polarization Targets

Much rigorous polarimetric measurement has been performed on the retina of the human eye, but the birefringence of the cornea offers an interesting and spatially-varying sample for polarimetric imaging.[51,52,101] Corneal birefringence resulting from the anisotropic collagen fibril orientation has been well studied and observed using multiple modalities,

including polarization-sensitive optical coherency tomography.[11,27–29,63,65,78,79,81,94] Of particular relevance is *in vivo* spatially-resolved polarization imaging between variously-oriented polarizers.[90–93] These works, as well as MM imaging, have been performed in visible wavebands.[13] Much of the literature indicates that the cornea exhibits linear retardance, with any circular retardance being relatively small if at all present.[13] However, near-infrared MM imaging of 20 human subjects' eyes performed as part of the presented work demonstrates the presence of significant circular retardance, which has not been reported before.[96] These Mueller eye measurements from 20 human subjects are used to demonstrate our approach for optimizing the contrast between two elliptical non-depolarizing pure retarder MMs.

With respect to polariscopic imaging of corneal birefringence, the approach presented in this Chapter may be useful for applications such as eye segmentation or eye tracking. The spatially-varying birefringence in the cornea is turned into spatially-varying brightness features, and maximizing the contrast could make such features easier to track.

3.3 Contrast Optimization

3.3.1 Mueller Analysis of Eye Measurements

The initial MM eye images were taken using the RGB950 as shown in Fig. 2.3b. The near-infrared waveband, centered at 947 nm with a full-width half max of 20 nm, was used in this work. The human subjects were illuminated with 0.0315 W/m^2. The eyes were measured in a reflective double-pass configuration where light transmitted through the cornea, reflected off the iris, and transmitted back through the cornea a second time. Over the course of 15 seconds, 25 polarimetric images with different PSG/PSA pairs were used to reconstruct the MM image. Image registration was performed on the 25 images before the MM reconstruction to mitigate the effects of unconscious random movements of the eye. The reconstructed MM image from one of 20 human subjects is shown in Fig. 3.1a. Remaining motion artifacts, on the order of several pixels, are to be expected but more slowly-varying polarimetric patterns are also observed. The inability to measure an *in vivo* human eye for an appreciable time duration motivates the investigation of snapshot

polariscopic eye imaging.

(a) Full MM

(b) TD approximation

(c) Dominant MJM

(d) Pure retarder
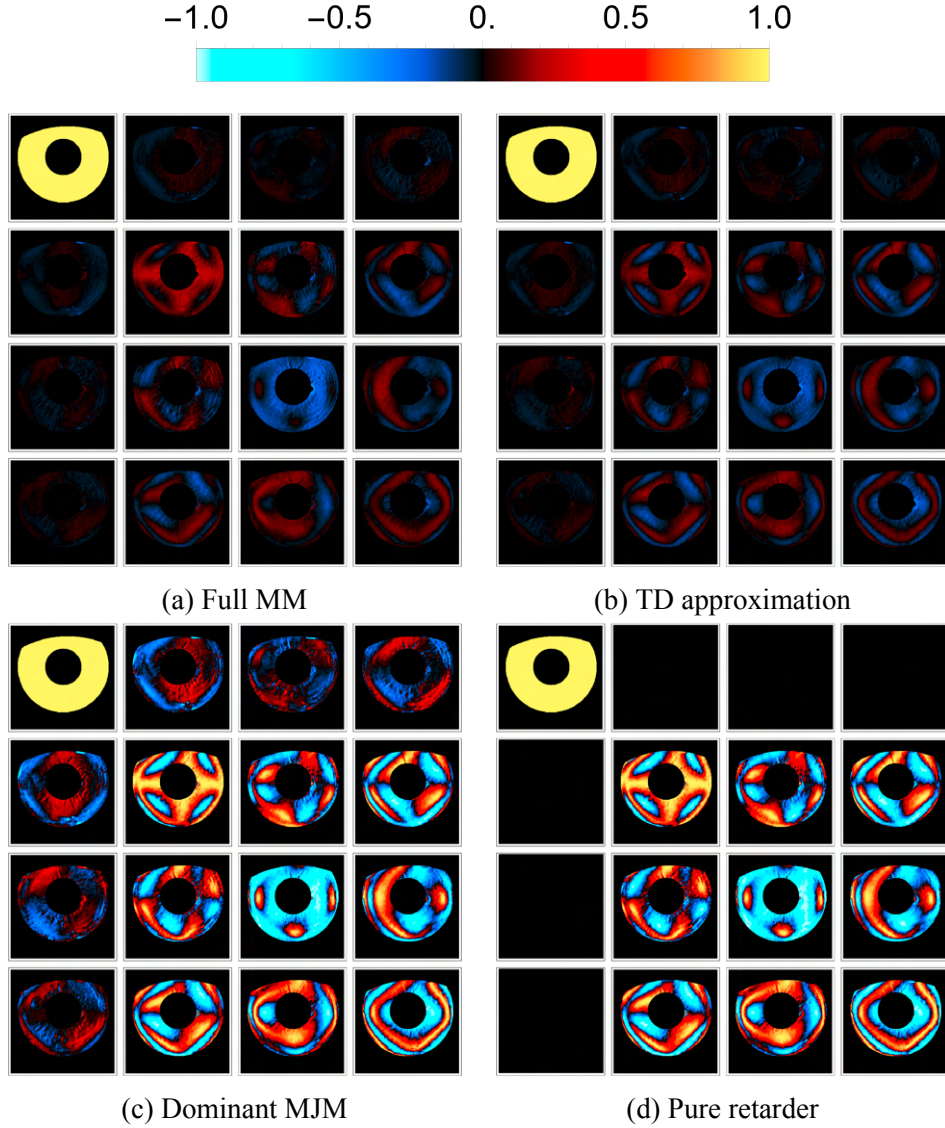
Figure 3.1: Near-infrared MM measurements of an *in vivo* human eye, masked to the region of the cornea where light is reflected back from the iris. In (a), the image is normalized such that $M_{00} = 1$ to visualize the spatially-varying polarization properties. In (b), the MM measurement is approximated as TD using Eq. 2.18 with (c) being the dominant MJM $\widehat{\mathbf{M}}_0$. In (d), the dominant MJM is further approximated as an elliptical pure retarder MJM, see Eq. 2.10.

The measured MM image in Fig. 3.1a has both depolarization and a small amount of diattenuation, so a series of approximations are performed in order to apply the optimiza-

tion. The TD approximation of the near-infrared eye MM image is shown in Fig. 3.1b with the dominant MJM image shown in Fig. 3.1c. The appropriateness of a TD approximation for these measurements is discussed in Sect. 3.5. To simplify the optimization of PSG and PSA states, the eye MM is further approximated as having a dominant MJM, $\widehat{\mathbf{M}}_0$, which is a pure retarder, see Fig 3.1d. The retarder MM is separated from the diattenuation by taking the unitary part from the polar decomposition of the dominant MJM. A general elliptical retarder MM, see Eq. 2.10, is characterized by its retardance vector $\vec{\boldsymbol{\delta}} = [\delta_H, \delta_{45}, \delta_R]$, where the magnitude of the vector is the retardance magnitude and the direction of this vector is the fast-axis on the Poincaré sphere. Due to phase wrapping, the retarder vector calculated from a MM is non-unique. For integers q, the retarder vector $\vec{\boldsymbol{\delta}}^q = \left(2\pi q + \|\vec{\boldsymbol{\delta}}\|\right) \vec{\boldsymbol{\delta}}/\|\vec{\boldsymbol{\delta}}\|$ will produce the same MM as $\vec{\boldsymbol{\delta}}$. In this work, q is assigned pixel-wise to produce smoothly-varying retardance vectors over the image. The specific value of q does not affect the optimization of the PSG/PSA states.

Images of each retardance component are shown in Fig. 3.2 for a single human subject's eye. The first two retarder vector components, shown in Fig. 3.2a-b, correspond to the linear retardance. For the majority of the unmasked area, the δ_H term has greater magnitude than the δ_{45} term. Therefore, the linear retardance is primarily horizontally or vertically oriented (where δ_H is positive or negative, respectively). The circular component, in Fig. 3.2c, shows significant circular retardance which has not been previously reported. The change from positive to negative values in δ_R indicates a change in the helicity of the fast-axis of retardance. The retardance magnitude in Fig. 3.2d, which is the norm of the retardance vector, shows two minima on the left and right of the masked region and a maximum at the bottom of the eye. A second maximum likely appears at the top of the eye but is obscured by the eyelid in this image. Not all of the observed retardance is the result of anisotropic structures within the eye. When light reverses direction, as it does when reflected from the iris, 45° and 135∘ linear polarization appear to flip, as well as the handedness of circular polarization. This is due to geometric phase, however in the MM image, this appears as π radians of horizontal linear retardance. This geometric phase is present in the MM image and in the retardance vector, however the retardance from structural anisotropy is also present.

(a) δ_H (b) δ_{45} (c) δ_R

(d) Retardance magnitude   (e) Retarder space
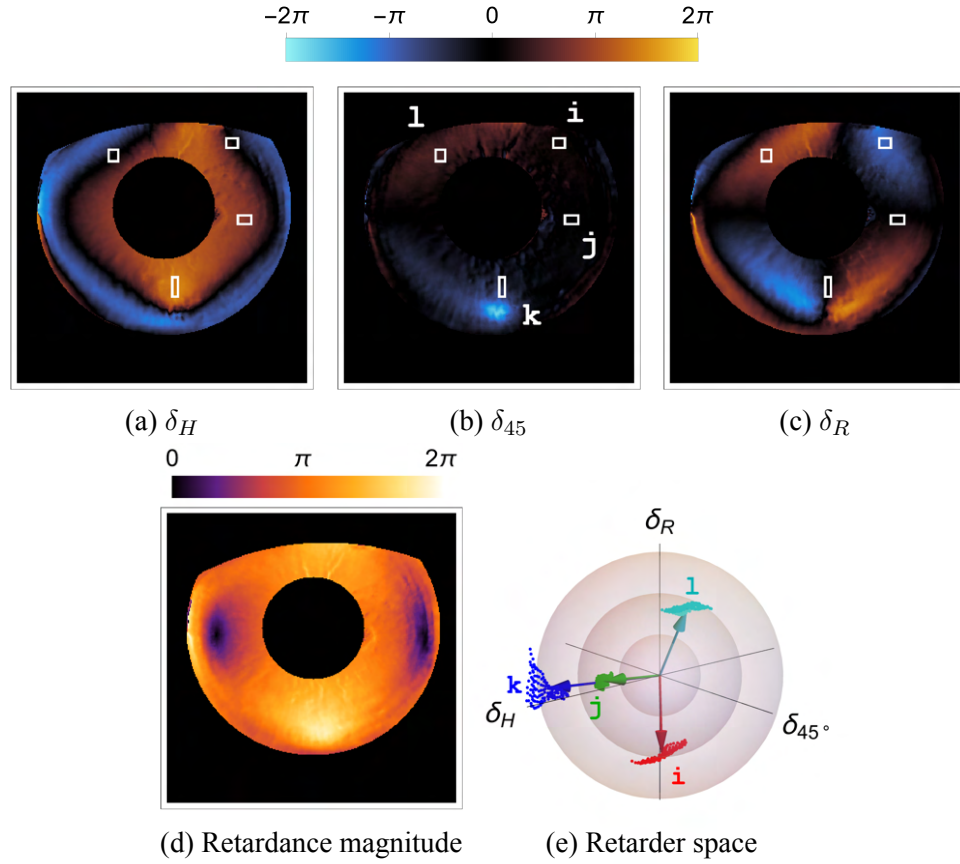
Figure 3.2: The horizontal, diagonal, and circular retardance computed from a measured MM are shown in (a), (b), and (c), respectively. The total retardance magnitude is shown in (d). ROIs are designated i-l. In (e), the retardance vectors within each ROI are plotted in 3D, where the concentric spherical surfaces denote $\pi/2$, π, and $3\pi/2$ radians of retardance. The point clouds represent the per-pixel retardance vectors and the arrows indicate the average retardance vector for each ROI. Average values are listed in Tab. 3.1.

The circular retardance result highlights the importance of performing the MM characterization as an initial step in the optimization described in the following section. Without first performing the Mueller image characterization, the purely linear retardance assumption found in the literature would have been used for the optimization. Trying to perform the optimization of the polariscopic pairs based on an assumed MM without the circular retardance would have resulted in non-optimal pairs. It should be noted that for this work, the net MM of the double-pass through the cornea is the desired quantity for optimizing the polariscopic pairs. The net MM describes the transformation of polarization which a

Table 3.1: Components and magnitudes of the average retarder vectors from the four ROIs shown in Fig. 3.2 in units of radians. Retardance magnitudes are known up to the order of retardance, where $2\pi q$ for integers q can be added to the magnitude without changing the resulting MM.

Region	δ_H	δ_{45}	δ_R	$\|\vec{\delta}\|$
i	0.256385	0.423876	-3.04746	3.08746
j	2.66172	-0.126005	0.25092	2.67649
k	4.48508	-1.23254	0.0570402	4.6517
l	-0.164669	1.38322	2.86614	3.18672

polariscope would image. In order to extract structural properties of the eye tissue, the ray paths and other geometric considerations would need to be characterized.

To reduce the impacts of measurement noise on the PSG/PSA optimization, the retarder vectors were averaged over each of the regions of interest (ROIs) shown as white boxes in Fig. 3.2. The average retarder vectors appear in Tab. 3.1. The retarder vectors were averaged rather than the MJMs because the addition of different MMs introduces depolarization which is undesirable in this application. ROIs i and j were chosen for use in the following optimization because they have different retardance orientations. The optimization could still be performed for ROIs with similar retardance vectors, such as j and k, but the maximum achievable contrast would be lower.

3.3.2 Optimal polariscopic Configurations

The contrast between polarimetric measurements of two MMs is defined as the magnitude of the measurement difference. This contrast ΔP is written

$$\Delta P = ||\mathbf{a}^\dagger(\mathbf{M}_i - \mathbf{M}_j)\mathbf{g}||, \tag{3.1}$$

where $\mathbf{M}_i$ and $\mathbf{M}_j$ are unique, *e.g.* different pixels or regions of a MM image. The maximum achievable contrast between two polarization states increases as their distance on the Poincaré sphere increases.[104] Therefore, the optimal PSG states $\mathbf{g}$ are those for which, $\mathbf{s}_i = \mathbf{M}_i\mathbf{g}$ and $\mathbf{s}_j = \mathbf{M}_j\mathbf{g}$, are exitant Stokes vectors with the greatest angle possible between them on the Poincaré sphere. Assuming that $\mathbf{M}_i$ and $\mathbf{M}_j$ are pure retarders (see

Sect. 3.5), maximizing this angle is equivalent to minimizing the inner product

$$\vec{\mathbf{s}}_j^\dagger \vec{\mathbf{s}}_i = (\mathbf{V}_j \vec{\mathbf{g}})^\dagger (\mathbf{V}_i \vec{\mathbf{g}}) = \vec{\mathbf{g}}^\dagger \left(\mathbf{V}_j^\dagger \mathbf{V}_i \vec{\mathbf{g}} \right) \tag{3.2}$$

where the vector arrow notation indicates a 3×1 vector quantity on the Poincaré sphere, as opposed to a 4×1 Stokes vector (*i.e.*, $\mathbf{g} = S_0[1, s_1, s_2, s_3] = S_0[1, \vec{\mathbf{g}}]$) and $\mathbf{V}$ are 3×3 unitary matrices from Eq. 2.10. As shown in Eq. 3.2, the inner product is invariant to multiplying both $\vec{\mathbf{s}}_j$ and $\vec{\mathbf{s}}_i$ by the unitary transform $\mathbf{V}_j^\dagger$, resulting in an inner product between the original PSG vector $\vec{\mathbf{g}}$ and that PSG vector after transformation by the new matrix $\mathbf{V}_j^\dagger \mathbf{V}_i$. This relation is shown graphically on the Poincaré sphere in Fig. 3.3a and b, where a retarder behaves as a rotation. The composition of two rotations is another rotation, so $\mathbf{V}_j^\dagger \mathbf{V}_i$ can be analyzed as any other elliptical retarder matrix as shown in Fig. 3.3c.

Points which are further from the rotation axis are rotated a greater distance. Polarization states on the surface of the Poincaré sphere which are 90° from the fast-axis of the composite retarder are rotated the most and therefore are the optimal PSG states. If the composite retarder $\mathbf{V}_j^\dagger \mathbf{V}_i$ has a retarder vector $\vec{\boldsymbol{\delta}}_{ji} = [\delta_H, \delta_{45}, \delta_R]$, then the great circle on the Poincaré sphere containing the optimal PSG states $\vec{\mathbf{g}}$ is defined as points satisfying the equation

$$\vec{\boldsymbol{\delta}}_{ji}^\dagger \vec{\mathbf{g}} = \delta_H \cos(2\theta) \cos(\eta) + \delta_{45} \sin(2\theta) \cos(\eta) + \delta_R \sin(\eta) = 0, \tag{3.3}$$

where θ and η are the coordinates on the Poincaré sphere corresponding to the major axis orientation and ellipticity of polarization states.

For each $\vec{\mathbf{g}}$ on this great circle, there are two antipodal analyzers which maximize ΔP as calculated in Eq. 3.1. These solutions can be found with the following geometric construction on the Poincaré sphere, shown graphically in Fig. 3.4. For the two states found by transforming the chosen PSG state with the different MMs $\vec{\mathbf{s}}_i$ and $\vec{\mathbf{s}}_j$, calculate their unit bisector

$$\vec{\mathbf{b}} = \frac{\vec{\mathbf{s}}_i + \vec{\mathbf{s}}_j}{\|\vec{\mathbf{s}}_i + \vec{\mathbf{s}}_j\|} \tag{3.4}$$

shown in purple on Fig. 3.4, and a unit vector perpendicular to their span

$$\vec{\mathbf{c}} = \frac{\vec{\mathbf{s}}_i \times \vec{\mathbf{s}}_j}{\|\vec{\mathbf{s}}_i \times \vec{\mathbf{s}}_j\|} \tag{3.5}$$

(a) Rotations applied separately

(b) Composite rotation

(c) Equivalent single rotation
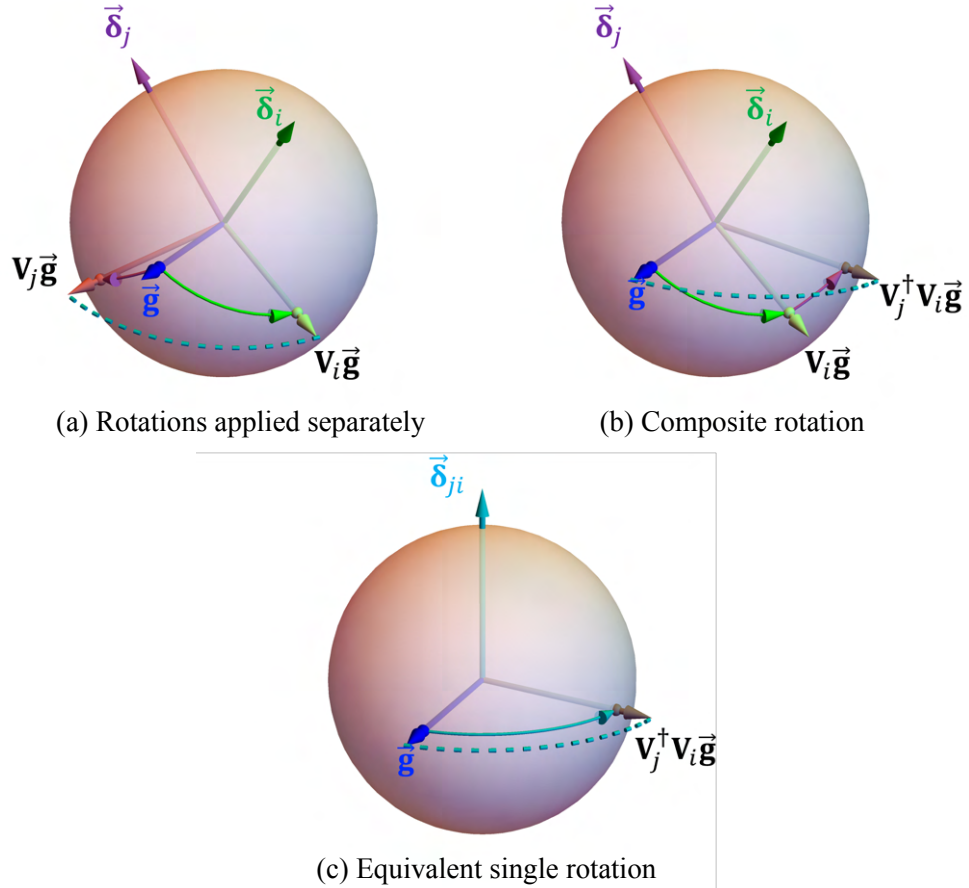
Figure 3.3: Geometric construction on the Poincaré sphere showing one optimal PSG state for a pair of retarder MMs with retardance vectors $\vec{\delta}_i$, shown in green, and $\vec{\delta}_j$, shown in purple. In (a), the PSG state $\vec{g}$ shown in blue undergoes rotation about the two retarder fast axes separately. This corresponds to what physically happens to polarization states in the two different regions of the image. The resultant states are separated by an angle shown with the dashed cyan line. In (b), the rotation about axis $\vec{\delta}_j$ is applied with the opposite handedness to the already-transformed state $\mathbf{V}_i\vec{g}$. The angle between the initial state $\vec{g}$ and the state after two rotations is the same as the angle in (a), see Eq. 3.2. In (c), the composite rotation from (b) is represented by a single rotation about axis $\vec{\delta}_{ji}$. Polarization states on the great circle perpendicular to this axis have the greatest angle on the Poincaré sphere after rotation, so they are the set of optimal PSG states, see Eq. 3.3.

shown in green. The PSA states which maximize the measurement difference between $\mathbf{s}_i$ and $\mathbf{s}_j$ are then found using the cross product of the bisector and normal of the span

$$\vec{a} = \pm \vec{b} \times \vec{c}, \tag{3.6}$$
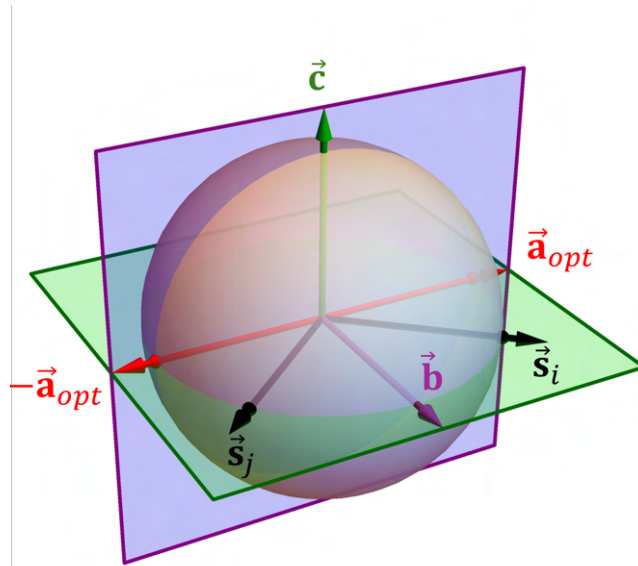
Figure 3.4: Geometric construction on the Poincaré sphere showing the optimal PSA states for two polarization states $\vec{s}_i$ and $\vec{s}_j$. The purple plane is normal to the vector $\vec{b}$ which bisects $\vec{s}_i$ and $\vec{s}_j$. The green plane is the span of $\vec{s}_i$ and $\vec{s}_j$, and is normal to $\vec{c}$. The optimal PSA states shown in red are found on the intersection of these two planes, and are calculated using Eq. 3.6.

and are shown in red on Fig. 3.4. A polariscopic configuration with $-\vec{a}$ will have reversed contrast from a configuration with $\vec{a}$, *i.e.*, bright regions in the image will become dark and vice versa.

The set of optimal PSG and PSA states for comparing $\mathbf{M}_i$ and $\mathbf{M}_j$ found using Eqs. 3.3-3.6 are shown in Fig. 3.5a. The set of PSA states associated with the different PSG states trace out a different great circle. A polariscopic image taken using any optimal $\mathbf{g}$ with an optimal $\mathbf{a}$ will have the same ΔP between the two MM pixels used in the optimization. The family of optimal polariscopic pairs are therefore indistinguishable for measurements comparing two pixels. However, the rest of the polariscopic image will generally be different for states chosen from this family of polariscopic pairs.

3.4 Polariscopic Measurements

For regions i and j, the compound retarder from Eq. 3.2 has $\vec{\delta}_{ji} = [-0.080, -3.108, 0.292]$. Optimal polarimetric pairs from Eq. 3.3 given $\vec{\delta}_{ji}$ are compared to the states constrained by the RGB950 hardware is shown in Fig. 3.5.

The PSG optics of the RGB950 consist of a fixed linear polarizer which defines the orientation of horizontal polarization and a rotating linear retarder, and the PSA consists of a rotating retarder and fixed polarizer as shown in Fig. 2.3a.[58] The rotating retarders have variable orientation, but fixed retardance magnitude for a given wavelength, so the states available for the PSG and PSA are constrained. The set of polarization states available from rotating the retarders trace out figure-eights on the surface of the Poincaré sphere, see Fig. 3.5b. The great circle of optimal PSG states intersects the figure-eight of available PSG states for all of the pairs of birefringent regions considered. However, the figure-eight of PSA states constrained by the rotating retarder polarimeter will not necessarily intersect the optimal PSA associated with the selected PSG state.

The spherical distance from the PSG great circle to the PSG figure-eight and the smaller of the spherical distances from the two associated PSA states to the PSA figure-eight are used to select the polarimeter configurations. The root sum of squares of these distances was used as a figure of merit for how close an available polariscopic pair was to optimal. This was performed numerically by discretizing the great circles into 360 equal segments and discretizing the figure-eights into $0.25°$ step rotations of the retarders. The root sum of squares distance from each (arbitrarily parameterized) point on the great circles to the figure-eights is shown in Fig. 3.5c. The three minima at positions 62, 184, and 307 (denoted I, II, and III) were selected for further analysis.

The modulation pattern was calculated by applying the chosen polariscopic pairs (*e.g.* states $\mathbf{g}$ and $\mathbf{a}$) to the pure retarder approximation of $\widehat{\mathbf{M}}_0$ at each pixel according to Eq. 2.19. The expected modulation patterns for the three selected optimal pairs are shown in Fig. 3.6a. Region i and region j (see Fig. 3.2) appear as dark and bright, respectively, in the modulation patterns computed for all three polariscopic pairs. However, the pattern over the rest of the image varies slightly between the three pairs, with I and III having a more rounded central bright region and II having a more distinct "plus sign" bright region. The polariscopic images shown in Fig. 3.6b are stills taken from real-time video captures. The rounded bright region expected in the center of images performed with polariscopic pairs I and III, and the bright "plus sign" in the image with pair II are visually apparent. The pattern in measurement III is less obvious, but this is consistent with pair
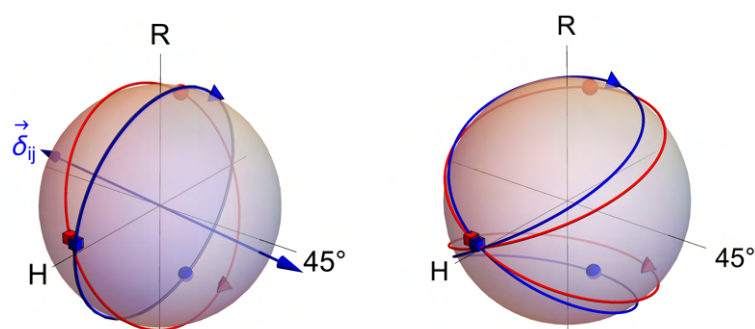
(a) Optimal Pairs　　　　　(b) Constrained Pairs
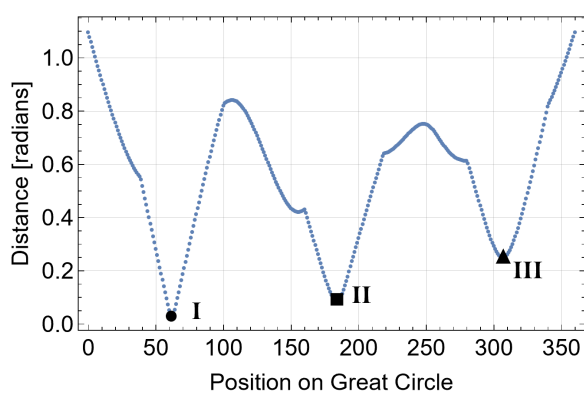
(c) Selected Pairs I, II, and III

Figure 3.5: On the Poincaré sphere, the set of optimal PSG states are shown in (a) as a blue great circle perpendicular to the $\vec{\delta}_{ji}$ axis shown with a blue arrow. The red great circle in (a) shows the set of optimal PSA states. The states constrained by the RGB950 hardware are shown in (b), with the set of PSG states shown on the blue figure-eight and the set of PSA states shown on the red figure-eight. In (c) there are three pairs: I, II, and III, where the optimal and hardware-constrained states are closest, in terms of a root sum of squared distance. In (a) and (b), the I, II, and III polariscopic pairs are shown with a circle, square, and triangle, respectively.
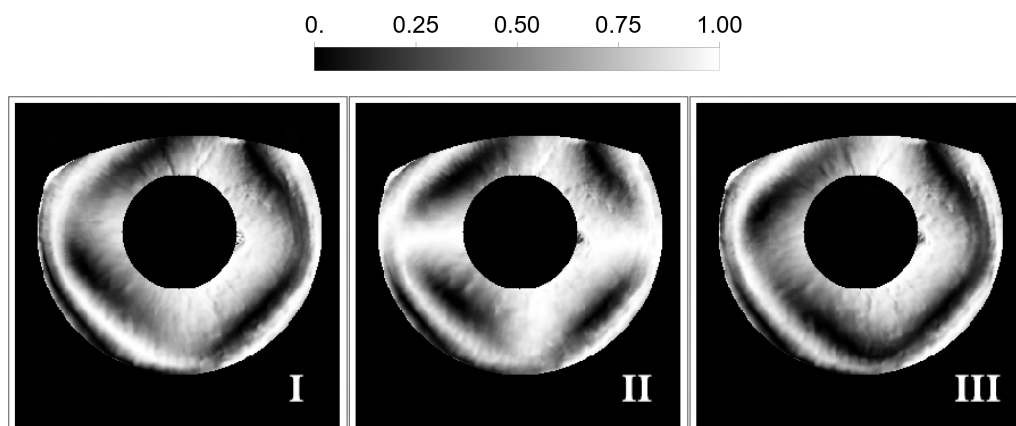
(a) Modulation computed from MM images for three different polariscopic pairs
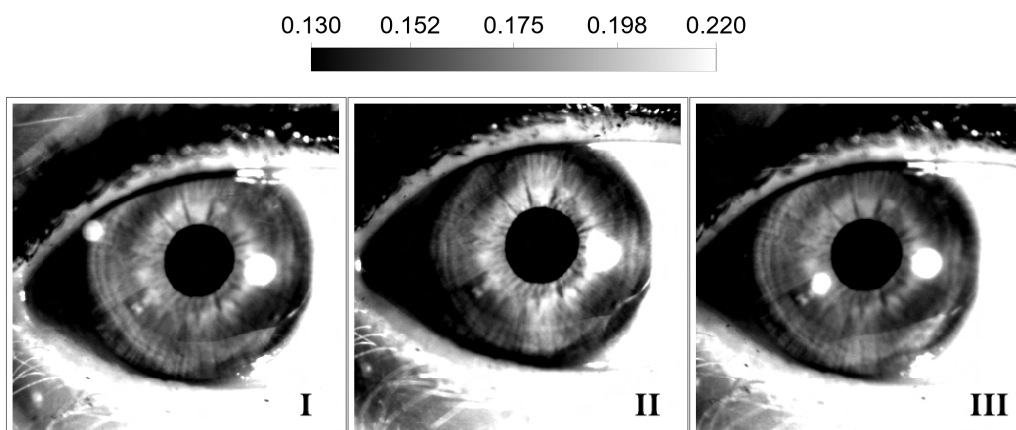
(b) Polariscopic measurements performed at three different polariscopic pairs

Figure 3.6: Simulated spatial modulation patterns (a) using three optimal polariscopic pairs and measurements (b) with the nearest available pairs in the RGB950. The simulated results are calculated using Eq. 2.19 and the pure retarder component from the TD approximation of the MM images. The spatially-varying patterns shown in simulation (a) are apparent in the measured results (b), though the presence of depolarization reduced the magnitude of the modulation. For this reason, the dynamic range of the measured polariscopic images was clipped to emphasize the modulation. The measurements in (b) are stills taken from real-time videos which can be found in the supplementary material for Reference.[38]

III being further from optimal as compared to I and II. Pixel-wise quantitative comparison is not performed here due to the challenges of low repeatability in the positioning of the human subjects' eyes. It should be noted that the three different polariscopic pairs shown

in Fig. 3.6 are optimal for the same pair of regions (i and j) and therefore are expected to only have minor differences in the modulation pattern over the rest of cornea. polariscopic pairs optimized for different ROIs would produce different modulation patterns. For example, when i and j are used in the optimization, i and l have similar responses. If the contrast between i and l were optimized, these ROIs would necessarily have different responses.

The presence of depolarization reduced the magnitude of modulation for the polariscopic images in Fig. 3.6b. The depolarization index (which ranges from 0 for the ideal depolarizer to 1 for a MJM) had an average value of 0.157 over the unmasked region of the MM measurement. The reduced modulation due to depolarization means that the dark regions of the pattern are not completely black in the measurement. Therefore, the dynamic range of the images in Fig. 3.6b was clipped in post-processing to make the polarimetric modulation pattern more visually apparent. This gives the appearance of overexposure in the sclera (white of the eye) to the right of the cornea and on the skin of the lower eyelid. The bright spot to the right of the pupil is glare reflected from the first surface of the eye. During MM acquisition, this spot is overexposed so the reconstructed MM value is inaccurate. Additionally, the light from the spot did not transmit into the eye and through the cornea, so the polarimetric response would not be well-represented by the birefringent model used for the cornea.

Over the unmasked region of the MJM image, the diattenuation magnitude had an average value of 25.5% which is fairly significant though the polarimetric behavior is dominated by retardance. The differences between the dominant MJM as calculated from the original MM and the pure retarder can be seen Fig. 3.1c and Fig. 3.1d.

The modulation patterns for polariscopic pair II were calculated for 19 other human subjects based on their eye MM images from the dataset of 20 MM measurements.[96] These patterns are shown in Fig. 3.7. The bright central "plus sign" appears for all individuals suggesting that the solution optimized for one human subject is robust to many more, though parts of the pattern may be obscured by the eyelid or pupil.
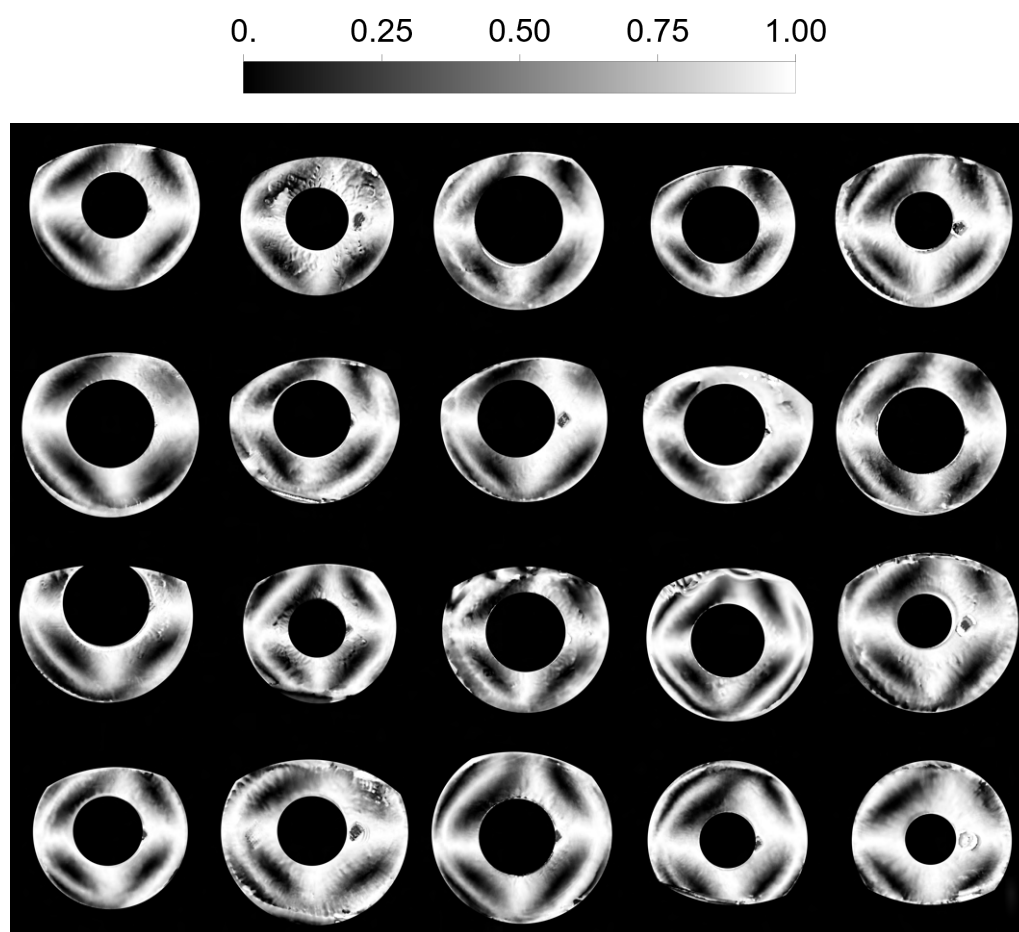
Figure 3.7: Modulation patterns for polariscopic pair II simulated from the MM images of 20 different individuals' eyes measured for this work. Configuration II was optimized for the first image (top-left), but qualitatively similar modulation patterns appear for all 20 eyes found in Dataset 1.[96]

3.5   Discussion

This Chapter presented a closed-form solution for maximizing the contrast between two retarder MMs in a polariscope imaging design. The method is general for any pair of elliptical retarders, and can be easily extended to depolarizing MMs that are well-approximated using a TD model. The wide range of observed retardance orientations, from purely linear to purely circular, observed across an individual's eye suggests that polariscopic imaging can be optimized to effectively identify different regions. To demonstrate the method,

the family of optimal PSG and PSA states was computed for two ROIs in the MM image of an *in vivo* human cornea. From this family of solutions, three polariscopic pairs were selected that were as close as possible to states available in an existing polarimeter.

The expected modulation pattern of these three optimal polariscopic pairs was compared to measurements using existing polarimeter hardware. The PSG and PSA for configuration II are both approximately horizontal linear polarization, which is a measurement performed by Sobzcak et al.[90] The modulation pattern observed in our simulation and measurement of configuration II is similar to the patterns reported in their work. The consistency between their measurements and our simulation based on MMs with elliptical retardance suggests that the significant ellipticity of the birefringence human cornea has been overlooked in other works. Notably, elliptical retardance can be created from stacking linear retarders with unaligned fast axes. The stroma is organized in about 200–500 fibrous lamellae and preferential orientation of collagen fibrils is known to be spatially-varying.[76] In the center of the cornea the lamellae orientations are expected to be one of two perpendicular directions which would not produce circular retardance. This is consistent with the MM measurements in the center of the cornea that appear in the literature.[13] Further from the center as the cornea curves to meet the sclera at the limbus, a greater degree of misalignment in the lamellae is expected which could produce elliptical and circular net birefringence.[65] Further analysis is required to support or refute a hypothesis that the elliptical and circular retardance we observed in MM human eye measurements are the result of fibril orientation.

Sources of disagreement between the polariscopic images, see Fig. 3.6a, and the modulation pattern computed from MM image, see Fig. 3.6b, are:

- The assumption of a TD eigenspectrum,

- The assumption of a pure retarder $\widehat{\mathbf{M}}_0$,

- The assumptions of uniformity of ξ_0 and M_{00},

- Motion artifacts in the MM measurement because it is reconstructed from 25 images acquired over 15 seconds,

- Blurring in individual polarimetric images due to the exposure time,

- Challenges with repeatability in the subject's eye position between measurements, and

- Measurement noise

These sources of disagreement are elaborated on below.

In a TD MM, the three smallest eigenvalues of the coherency matrix are degenerate.[55] If all four eigenvalues are normalized to sum to unity, then taking the smaller three eigenvalues $[\xi_1, \xi_2, \xi_3]$ as 3D rectilinear coordinates forms the natural depolarization space.[75] In this space, the Euclidean distance from $[\xi_1, \xi_2, \xi_3]$ to the TD point $\frac{1-\xi_0}{3}[1, 1, 1]$ is

$$\Delta\xi_{TD} = \sqrt{6\left[\left(\xi_1 - \frac{1-\xi_0}{3}\right)^2 + \left(\xi_2 - \frac{1-\xi_0}{3}\right)^2 + \left(\xi_3 - \frac{1-\xi_0}{3}\right)^2\right]}, \qquad (3.7)$$

where the factor of $\sqrt{6}$ is included to normalize the TD distance to range from 0 to 1, with 0 being exactly TD and 1 being as far from TD as possible. Figure 3.8a shows $\Delta\xi_{TD}$ calculated over the MM image of the cornea and Fig. 3.8d shows the same data summarized in a histogram. $\Delta\xi_{TD}$, which has a mean value of 0.151 and a standard deviation of 0.029, is assumed to be low enough for the MM image to be accurately approximated as TD.

For any combination of PSG/PSA, the polarimetric measurement of the ideal depolarizer is constant $\mathbf{aM}_{ID}\mathbf{g} = \frac{1}{2}$. Modulation in a polarimetric measurement of a TD MM is therefore only the result of $\mathbf{a}\widehat{\mathbf{M}}_0\mathbf{g}$, with M_{00} and ξ_0 determining the overall brightness and the constant offset, respectively. The average reflectance M_{00} and depolarization parameter ξ_0 are shown as images in Fig. 3.8 b and c, respectively, and summarized as histograms in Fig. 3.8d. The standard deviation of ξ_0 is 0.023 and the standard deviation of M_{00} is 0.042, so these parameters are assumed to be uniform such that their influence on a polarimetric measurement P is the same over the cornea. Therefore, M_{00} and ξ_0 are assumed to be uniform such that their influence on a polarimetric measurement P is the same for any two pixels.

The optimization is affected by measurement noise to the extent that the initial MM characterization is affected. For this reason, the optimization was performed based on

(a) $\Delta\xi_{TD}$ image (b) ξ_0 image (c) M_{00} image

(d) Histogram of polarization parameters
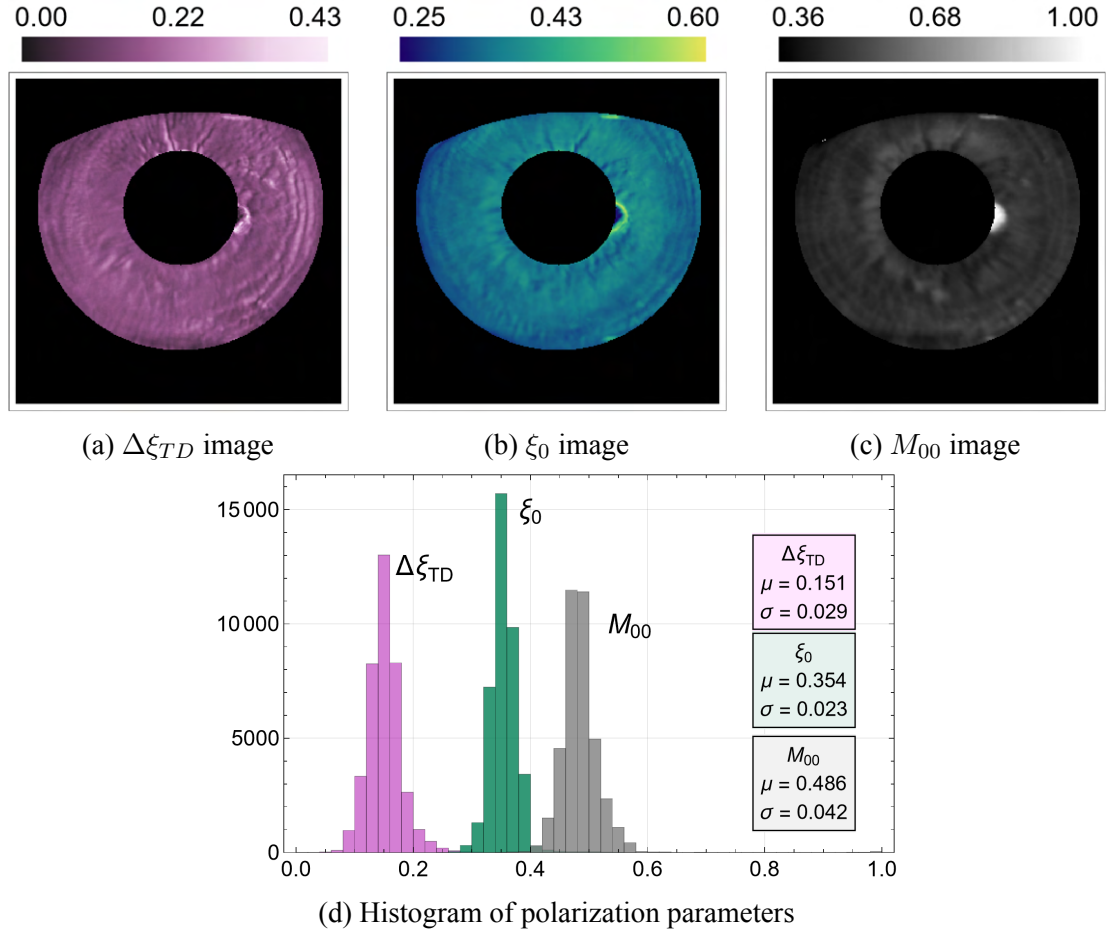
Figure 3.8: Images (a-c) and histograms (d) of quantities derived from the MM image of an *in vivo* human cornea. $\Delta\xi_{TD}$, calculated according to Eq. 3.7, (a) describes how close the coherency matrix eigenspectrum is to being TD. $\Delta\xi_{TD}$ is assumed to be low enough for the MM image to be approximated as TD. The mean and standard deviation of the TD distance are 0.151 and 0.029, respectively. ξ_0 (b) is the parameter which controls the amount of depolarization in a TD MM. The mean and standard deviation of ξ_0 are 0.355 and 0.023, respectively. M_{00} (c) is the overall reflectance, here normalized by the brightest pixel in the image. The mean and standard deviation of M_{00} are 0.485 and 0.042, respectively. ξ_0 and M_{00} are assumed to be uniform over the cornea such that they do not contribute to differences in polarimetric measurement across the image.

retardance vectors averaged over ROIs. These optimized measurements are invariant to calibration errors in the retardance magnitude or rotational offset of the waveplates because the same instrument was used to perform the initial MM characterization as the subsequent polariscopic images. Even if the reported optimal states do not accurately de-

scribe the real PSG and PSA states, the contrast would still be maximized. However, if we perform the optimization based on MM data with calibration issues and then performed the polariscopic images from a different polarimeter, the calibration issues would manifest as reduced contrast.

It is worth noting that while our method maximizes the contrast between two retarder MMs, the method does not guarantee that the two chosen MMs will be the brightest or darkest in the polarimetric image of an object with spatially varying birefringence. For example, if two MMs are chosen which have similar retardance orientations and magnitudes, the maximum achievable contrast between those two MMs may be lower than the maximum contrast imaged for another pair of regions. Furthermore, the choice of ROIs in the image also affects the specific spatial modulation patterns created by polariscopic imaging. This is an additional design variable as some patterns may be preferable depending on the application.

The use of an existing dual-rotating-retarder polarimeter constrained the polariscopic pairs that could be measured. If a polarimeter is designed for polariscopic eye imaging, then the PSG and PSA states can be optimized for this task. Consequently, this polariscopic demonstration does not achieve an upper contrast limit. Increased modulation and different spatial distributions are potentially possible if a near-infrared polariscopic imaging system is designed for *in vivo* human eyes. DoFP polarization cameras, which acquire images through four different linear polarizers simultaneously at the cost of spatial resolution, have been used in the literature to improve polarimetric measurement speed.[35,56] Simultaneous image capture for the different PSA states is of particular interest for measurements of eyes. However, this would be a fundamentally different optimization problem than is explored in this work.

CHAPTER 4

pBRDF Acquisition and Representation

4.1 Empirical Polarized Scattering Models

pBRDF material representations are utilized in many computer vision and physics-based rendering applications.[44,48,66] For the forward problem of polarized image rendering, the pBRDF for each material in a scene is required to determine how polarization is transformed at each light-matter interaction. For the inverse problems, the pBRDF is used to relate polarized measurements to scene attributes. Analytic pBRDFs eliminate the need to store and interpolate MMs.[7,30,39,45] However, empirical models are more realistic and can aid the development and validation of analytic models.[25]

An empirical pBRDF consists of measured MMs that are tabulated to characterize the ray direction dependency with a discrete number of scattering geometries. Sufficiently many geometries must be sampled for the empirical pBRDF to accurately represent variations in the polarimetric scattering from the material. The requirement on accuracy is application-dependent. Due to the sheer number of geometries typically needed, image-based techniques are employed to capture multiple geometries simultaneously.[8,26,60,62] For example, a sphere has rapidly but smoothly varying geometry over an image so a large number of unique geometries can be sampled at a time. This imaging is then performed using a goniometric camera stage to sample the full range of possible scattering geometries. Despite this, not all geometries are sampled in a given sequence of goniometric positions. The unmeasured geometries may be interpolated from the measured MMs in a step known as inpainting.[8] The term inpainting is used to differentiate this preliminary interpolation step from interpolation that is performed during a ray trace. During rendering a given simulated ray direction is likely to be interstitial to tabulated geometries, thus requiring interpolation to evaluate the MM. In practice, the tolerance on inpainting and interpolation depend on both the application and optical properties of the material. MM

interpolation is not only computationally expensive but also can introduce artifacts such as spurious depolarization or non-physical MM solutions.[72]

The database from the Korea Advanced Institute of Science and Technology (KAIST) contains 25 samples and is the only publicly-available set of measured pBRDFs for indoor materials known to the author.[8] The acquisition protocol for pBRDFs in the KAIST database is reported to make use of 147 goniometer positions at five wavelengths which requires 2.5 days of imaging per material. The KAIST pBRDF database, as well as many scalar BRDF databases (such as the database from Mitsubishi Electronics Research Laboratory (MERL) which contains 100 materials[61]), parameterize scattering geometries in terms of a coordinate system devised by Rusinkiewicz.[84] For isotropic surfaces, the pBRDF depends on only three of the four Rusinkiewicz angles. The three remaining Rusinkiewicz angles are interpreted as linear dimensions in a Cartesian space. MM (KAIST) or scalar reflectance (MERL) measurements are then associated with discrete points on the Cartesian grid. This grid includes redundant triplets of Rusinkiewicz angles (*i.e.*, corresponding to the same physical scattering geometry) as well as triplets which correspond to transmission geometries rather than reflection. Data are associated with discrete points over a of volume $15.503 rad^3$, but the reflection region only has a volume of $9.567 rad^3$. It is important to note that here, isotropic materials are isotropic in both effective refractive index as well as in surface texture. An example of an indoor material which has isotropic index but anisotropic surface texture would be brushed stainless steel. Such a material would require parameterization by four angles to indicate azimuthal orientation relative to the direction of anisotropy.

In this work, we interpret the three Rusinkiewicz angles for isotropic pBRDFs as the radial, azimuthal, and axial coordinates in a cylindrical space. This eliminates redundant coordinates and makes the subspace corresponding to reflection geometries more compact. The details of this representation are described in Sect. 4.2. In Sect. 4.3, we then demonstrate the use of the fill fraction of this subspace as a figure of merit to compare different sequences of goniometer positions to efficiently acquire an empirical pBRDF. In Sect. 4.4, the efficient goniometer protocol is performed on a sphere of a selective laser sintering 3D printing material at two visible wavelengths using the RGB950. The MM

data in the pBRDF are then visualized as cross-sections of the cylindrical representation.

4.2 Ray Geometry Parameterization

Polarized and scalar BRDFs are functions of illumination and observation ray directions $\widehat{\omega}_i$ and $\widehat{\omega}_o$, respectively, as shown in Fig. 4.1. These two directions can be parameterized in spherical coordinates by four angles with respect to the object's surface normal $\widehat{\mathbf{n}}$ as zenith. In this parameterization, θ_i and θ_o are the zenith angles. Reflection geometries, defined as having external scattering, are constrained to have zenith angles less than $\pi/2$. Isotropic surfaces are defined by pBRDF invariance to rotations of the material about its surface normal. This assumption reduces dependence to three angles since the pBRDF is only a function of the difference of azimuth angles, ϕ_i and ϕ_o in Fig. 4.1. A further insightful parameterization of the ray directions is provided by Rusinkiewicz.[84] Many BRDFs and pBRDFs make use of microfacet theory, where light scattering occurs at sub-resolution surfaces which satisfy the law of reflection.[10, 12, 34, 40, 55, 80, 105] Rusinkiewicz parameterized BRDFs using spherical coordinates relative to the microfacet's surface normal which bisects $\widehat{\omega}_i$ and $\widehat{\omega}_o$, denoted $\widehat{\mathbf{h}}$ in Fig. 4.1. The angle of incidence onto the microfacet is θ_d. The angle between the microfacet and the object's surface normal, is denoted θ_h. This is the angle between $\widehat{\mathbf{n}}$ and $\widehat{\mathbf{h}}$ in Fig. 4.1, and can be interpreted as the degree to which a scattering geometry deviates from obeying the law of reflection with respect to $\widehat{\mathbf{n}}$. The range of both θ_d and θ_h is 0 to $\pi/2$. The third Rusinkiewicz angle is an azimuthal angle denoted ϕ_d which is the angle between two planes: the scattering plane (spanned by $\widehat{\omega}_i$ and $\widehat{\omega}_o$) and the plane spanned by $\widehat{\mathbf{n}}$ and $\widehat{\mathbf{h}}$. The value of ϕ_d can range between $-\pi$ and π. When π is added to ϕ_d, the scattering plane is unchanged but $\widehat{\omega}_i$ and $\widehat{\omega}_o$ are swapped such that the light travels in the reversed direction. For a MM representing a light-matter interaction $\mathbf{M}$, the MM for the reversed light path is calculated $\mathbf{O}\mathbf{M}^{\intercal}\mathbf{O}^{-1}$, where $\mathbf{O}$ is a diagonal matrix with diagonal elements $(1, 1, -1, 1)$.[32, 85, 86] This reciprocity would suggest that the range of ϕ_d containing unique information is 0 to π. However measured data can be subject experimental conditions which break reciprocity.[7, 19, 53] We therefore do the same as the KAIST pBRDF database and use the full range of $-\pi$ to π for ϕ_d.[8]
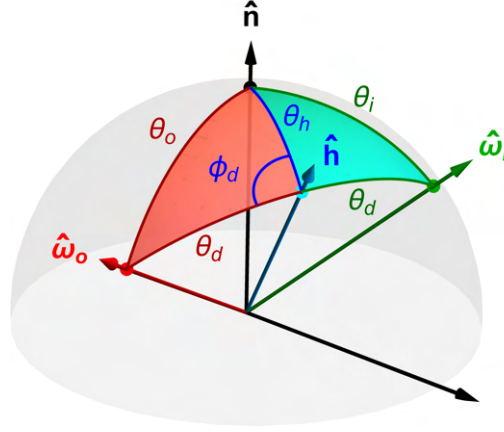
Figure 4.1: Scattering geometry showing paramterization with both spherical coordinates about the surface normal $\widehat{\mathbf{n}}$ and Rusinkiewicz coordinates. The spherical triangles with vertices $\{\widehat{\mathbf{n}}, \widehat{\boldsymbol{\omega}}_o, \widehat{\mathbf{h}}\}$ (red), and $\{\widehat{\mathbf{n}}, \widehat{\mathbf{h}}, \widehat{\boldsymbol{\omega}}_i\}$ (green) are used to determine the conditions for whether a scattering geometry parameterized with Rusinkiewicz coordinates is a reflection geometry.

A given Rusinkiewicz triplet $(\theta_d, \phi_d, \theta_h)$ may not correspond to a physical ray geometry of external reflection. The condition for ray direction zenith angles (θ_i and θ_o) both being less than $\pi/2$ must still be satisfied. In Fig. 4.1, spherical triangles with vertices $\{\widehat{\mathbf{n}}, \widehat{\boldsymbol{\omega}}_o, \widehat{\mathbf{h}}\}$ and $\{\widehat{\mathbf{n}}, \widehat{\mathbf{h}}, \widehat{\boldsymbol{\omega}}_i\}$ are used with the spherical law of cosines to derive the relation between Rusinkiewicz angles and the zenith angles θ_i and θ_o,

$$\cos(\theta_i) = \cos(\theta_h) \cos(\theta_d) - \sin(\theta_h) \sin(\theta_d) \cos(\phi_d), \tag{4.1}$$

and

$$\cos(\theta_o) = \cos(\theta_h) \cos(\theta_d) + \sin(\theta_h) \sin(\theta_d) \cos(\phi_d). \tag{4.2}$$

For a ray geometry to satisfy external reflection, the cosine of zenith angles for both the incoming and outgoing rays must be between zero and one.

4.2.1 Cartesian Coordinate Representation

In the 3D space of points $(\theta_d, \phi_d, \theta_h)$, setting Eqs. 4.1 and 4.2 equal to zero defines two surfaces which together enclose the region of reflection geometries. Figure 4.2a shows this region of reflection geometries when $(\theta_d, \phi_d, \theta_h)$ are interpreted as Cartesian coordinates. Existing empirical databases use a Cartesian interpretation when tabulating the

measured pBRDFs. Each dimension is discretized to produce a 3D rectangular grid of points representing the scattering geometry, then measured MM data is associated with the points on this grid. The base of the region, where $\theta_h = 0$, is the plane of scattering geometries where $\widehat{\mathbf{h}}$ and $\widehat{\mathbf{n}}$ are collinear. In other words, Rusinkiewicz angles on the base of the pBRDF region are those which satisfy the law of reflection and are referred to as specular geometries. The vertical planes where $\phi_d = 0$ and $\phi_d = \pm\pi$ represent geometries where the surface normal $\widehat{\mathbf{n}}$ is within the scattering plane spanned of $\widehat{\boldsymbol{\omega}}_i$ and $\widehat{\boldsymbol{\omega}}_o$. For this reason, these geometries are referred to as in-plane scattering.

The Cartesian interpretation is convenient for its simplicity but has several drawbacks. It is not obvious from Fig. 4.2a that ϕ_d is 2π-periodic, which is to say that the in-plane scattering geometries at $\phi_d = \pi$ are equivalent to the geometries at $\phi_d = -\pi$. Additionally, when $\theta_d = 0$, the vectors $\widehat{\boldsymbol{\omega}}_i$, $\widehat{\boldsymbol{\omega}}_o$, and $\widehat{\mathbf{h}}$ are all collinear so they do not span a plane and the scattering geometry is invariant to ϕ_d. This fact is not accounted for in the Cartesian representation, resulting in degenerate triplets of Rusinkiewicz angles. In the tabulated pBRDFs in the KAIST database, data is saved for every triplet of Rusinkiewicz angles where θ_d is on the interval $[0, \pi/2]$, ϕ_d is on the interval $[-\pi, \pi]$, and θ_h is on the interval $[0, \pi/2]$, forming a rectangular parallelepiped which encloses the reflection region. The reflection region has a volume of $9.567rad^3$ and only occupies 61.7% of the rectangular parallelepiped, so 38.3% of the saved data is unused. Convexity is desirable for both inpainting and interpolation since the line connecting any two samples remains within the set. A convex hull is the smallest convex shape which encloses a given region. The percent of the convex hull which is occupied by the enclosed region serves as a figure of merit for convexity, with 100% meaning the region itself is convex. The convex hull which encloses the reflection region in Cartesian coordinates has a volume of $14.217rad^3$ meaning that only 67.3% of the convex hull is filled.

4.2.2 Cylindrical Coordinate Representation

This work introduces the interpretation of Rusinkiewicz triplets as cylindrical coordinates where θ_d is the radial distance, ϕ_d is the azimuth angle, and θ_h is the height. The region of reflection geometries for the cylindrical coordinate interpretation is shown in Fig. 4.2b.

(a) Cartesian coordinates   (b) Cylindrical coordinates
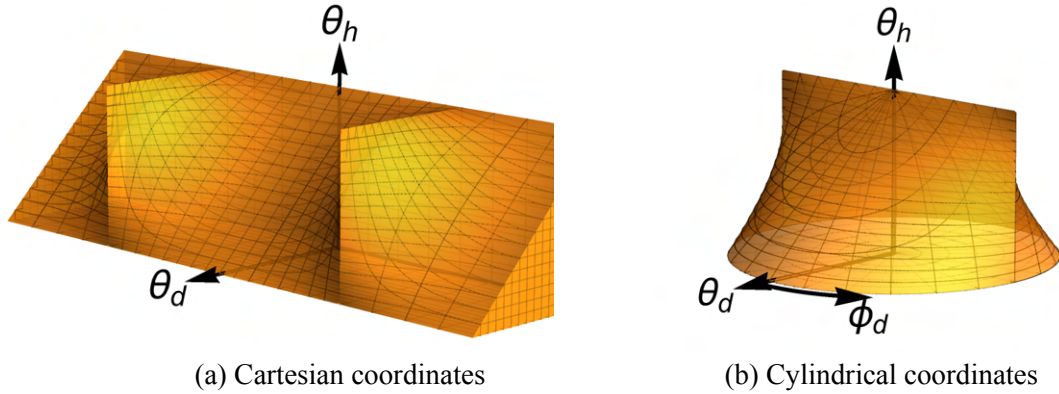
Figure 4.2: Enclosed region of Rusinkiewicz triplets for reflection geometries interpreted as (a) Cartesian coordinates and (b) cylindrical coordinates. Equations 4.1 and 4.2 define the bounding surface shown in orange. The reflection region has a different shape in Cartesian versus cylindrical coordinates. The volume and convexity of these regions are compared in Tab. 4.1

The cylindrical coordinate parameterization offers several benefits over the Cartesian parameterization. Using ϕ_d as the azimuth angle in cylindrical coordinates captures its 2π-periodic behavior, and in fact the in-plane scattering geometries all exist on a single planar cross section. The $\theta_d = 0$ plane in Cartesian coordinates collapses to a line in cylindrical coordinates, eliminating the degeneracies with respect to ϕ_d. At the top of the region, where $\theta_h = \pi/2$, the enclosing surfaces converge to a the line where $\phi_d = \pm\pi/2$. Here, the scattering plane is perpendicular to $\widehat{\mathbf{n}}$, so any perturbation in ϕ_d results in either $\widehat{\boldsymbol{\omega}}_i$ or $\widehat{\boldsymbol{\omega}}_o$ violating the condition for external reflection.

Is it notable that the cylindrical coordinate system reduces the volume of the Cartesian representation even before non-reflected geometries are omitted. The enclosing cylinder's volume $12.176 rad^3$, which is 79% of the volume of the enclosing enclosing parallelepiped for Cartesian coordinates. Further reductions are possible by omitting non-reflection geometries since the reflection region is a subset of the enclosing volume. For cylindrical coordinates the reduced volume is $5.686 rad^3$. The volume of the reflection region in cylindrical coordinates is only 37% of the volume of the enclosing parallelepiped in Cartesian coordinates used in the state-of-the-art. Rejecting non-reflection geometries is not a process unique to the cylindrical representation, however in Cartesian coordinates

this process results in a reduction only to 62% as many samples. For uniform sampling, this means that either fewer MM measurements are required in cylindrical coordinates to achieve comparable sampling density as Cartesian or that the same number of MM measurements can be taken to produce finer sampling. In this way, the cylindrical representation of the pBRDF is more efficient. The region in cylindrical coordinates also becomes closer to convex, occupying 85.7% of its convex hull. The properties of the Cartesian and cylindrical coordinate representations are summarized in Tab. 4.1.

Table 4.1: Comparison of the Cartesian and cylindrical coordinate representations of reflection geometries in Rusinkiewicz angle space. MM data is associated with discrete points within Rusinkiewicz angle space. The cylindrical representation decreases the volume and increases the convexity of the region which must be populated with MM data.

	Cartesian	Cylindrical
Volume of basic enclosing solid	15.503	12.176
Volume of reflection region	9.567	5.686
Volume of convex hull	14.2168	6.6325
Number of bins with area $1° \times 1°$ in the θ_d-ϕ_d plane	32,851	25,653
Total bins including transmission geometries	2,989,441	2,334,423
Total reflection bins for linear θ_h sampling	1,838,964	1,086,904

One of the trade-offs of using the cylindrical representation is the increased complexity in discretization. For the sake of comparison, we chose to discretize the cylindrical representation such that each bin occupies the same volume as in the Cartesian representation (equivalent to $1°$ cubed). In cylindrical coordinates, the volume of a bin with a fixed azimuthal interval and a fixed radial interval increases with radial position. In order to maintain a fixed volume even as the radial coordinate, θ_d, increases, the azimuthal and radial intervals change. This results in an irregularly spaced set of discrete Rusinkiewicz triplets. Discretization strategies with variable bin volume but fixed azimuthal and radial spacing are also possible. We also exclude Rusinkiewicz triplets which are outside the reflection region. This could also be done with the Cartesian representation to improve tabulation efficiency, so it is not a unique advantage of the cylindrical representation. This omission of non-reflection geometries is likely not done for the KAIST database because simplicity is one of the main benefits of the Cartesian representation. Discretization of the

cylinder which would enclose the reflection region shown in Fig. 4.2b would result in 2.3 million bins, of which only 1.1 million would contain tabulated MM data.

Our cylindrical discretization makes use of 107 bins of θ_d (the radial coordinate) indexed with integers i between 0 and 106. The first bin, where $i = 0$, is centered at $\theta_d = 0$ where ϕ_d is undefined, so the bin is a circle of radius $\sqrt{1°/\pi}$ such that it has an area of $1° \times 1°$. For the $i \neq 0$ cases, the bins are segments of cylindrical shells where the azimuth coordinate ϕ_d is discretized into an integer number of bins of width given by

$$\Delta\phi_d^i = \frac{90°}{7 + i}. \tag{4.3}$$

The denominator offset of seven is chosen to split the 2π range into 32 segments for $\Delta\phi_d^1$. Given an azimuth bin width $\Delta\phi_d^i$, the ith radial bin width for $1 \leq i \leq 106$ is

$$\Delta\theta_d^i = -\theta_d^{i-1} + \sqrt{\frac{2A}{\Delta\phi_d^i} + (\theta_d^{i-1})^2} \tag{4.4}$$

where A is the area in the θ_d-ϕ_d plane and is assigned the value $1° \times 1°$. The original number of 107 θ_d bins was chosen so that the $i = 106$ radial position, as determined by Eqs. 4.3 and 4.4 falls on $\theta_d = \pi/2$. The height coordinate is linearly discretized with bin size given by $\Delta\theta_h = 1°$. To form bins in the θ_d-ϕ_d plane which have constant area, $\Delta\theta_d^i$ depends on both the size of the azimuthal bin $\Delta\phi_d^i$ as well as the previous radial position θ_d^{i-1}. As θ_d increases, $\Delta\phi_d$ gets smaller.

When tabulating the pBRDF, care should be taken such that data are reported with an unambiguous definition for horizontal and vertical. This is because a MM maps input polarization to output polarization and these states are defined in reference to some implicit basis of horizontal and vertical in the plane perpendicular to the propagation direction (referred to as the transverse plane). For a microfacet Fresnel reflection model, the conventional definitions of horizontal and vertical come from the eigenpolarizations.[14] These eigenpolarizations are found using the scattering plane spanned by $\widehat{\omega}_i$ and $\widehat{\omega}_o$. For a measured MM, the implicit definitions of horizontal and vertical come from $\mathbf{g}_n$ and $\mathbf{a}_n$ of the polarimeter. Naively applying MMs taken from a measurement to any particular application without reconciling the transverse plane basis can result in inaccurate results. Further details regarding the transverse plane bases are provided in Appendix A.
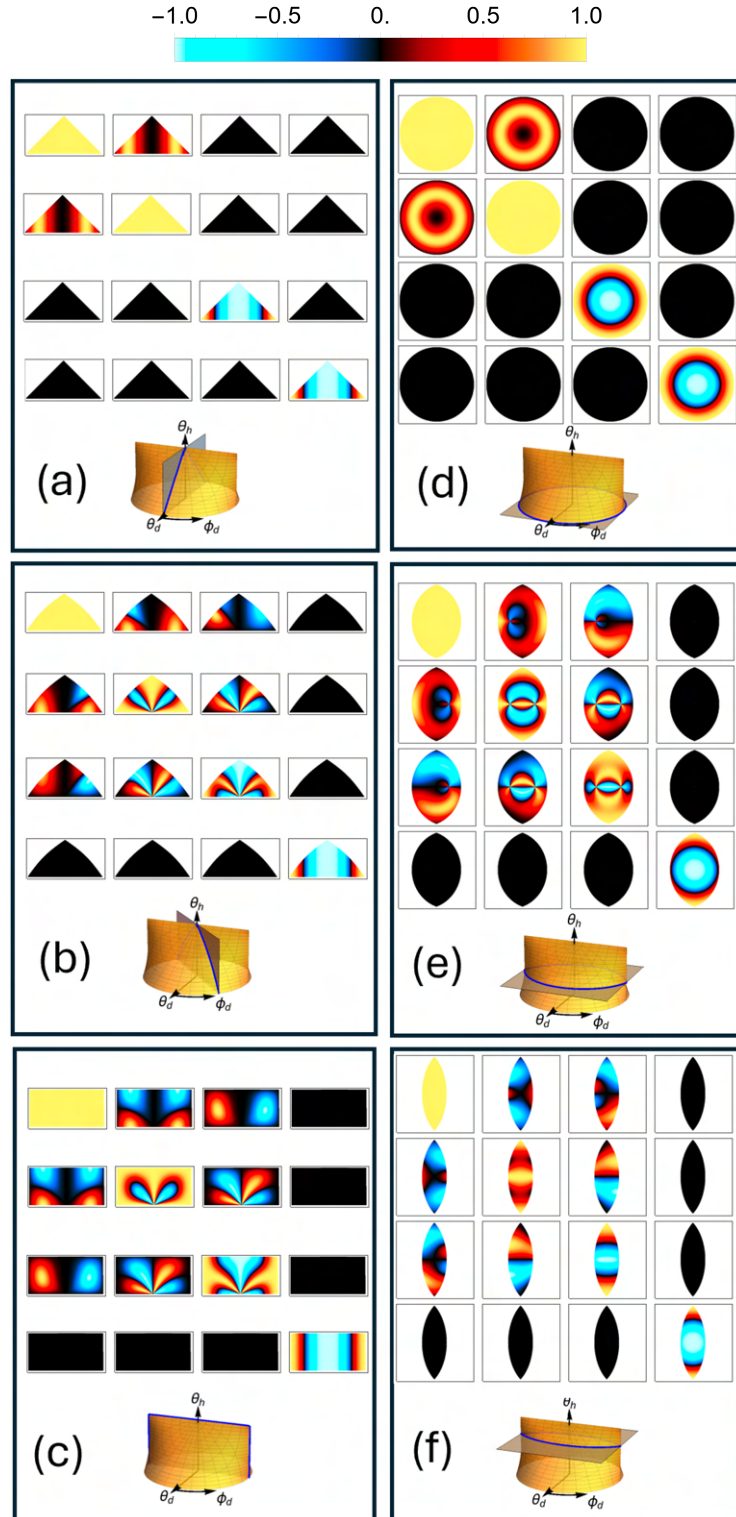
Figure 4.3: Cross sections of a simulated pBRDF for Fresnel reflection based on micro-facet theory displayed as MM images for the planes where (a) $\phi_d = 0$ and π, (b) $\phi_d = \pi/4$ and $5\pi/4$, (c) $\phi_d = \pi/2$ and $3\pi/2$, (d) $\theta_h = 0$, (e) $\theta_h = \pi/6$, and (f) $\theta_h = \pi/3$.

Figure 4.3 shows the normalized pBRDF simulated for Fresnel reflection based on microfacet theory on various cross sections of the reflection region in cylindrical coordinates. The Fresnel coefficients were calculated using θ_d as the angle of incidence for an interface between air and a medium with refractive index $n = 1.5$. Figures 4.3a-c are cross sections of the pBRDF on vertical planes for different values of ϕ_d. The cross section shown in Fig. 4.3a, where $\phi_d = 0$ and π, is the in-plane scattering geometries. Here, the surface normal $\widehat{\mathbf{n}}$ is within the scattering plane spanned by $\widehat{\boldsymbol{\omega}}_i$ and $\widehat{\boldsymbol{\omega}}_o$. Along this cross section, the pBRDF support region is a triangle. As the cross sectional plane rotates to other values of ϕ_d, the support region increases size as in Fig. 4.3b until $\phi_d = \pi/2$ and $3\pi/2$ in Fig. 4.3c. In Fig. 4.3c, the support becomes rectangular. Figure 4.3d-f are horizontal slices for different constant values of θ_h. Figure 4.3d is the plane where $\theta_h = 0$, and the support is a full circle. As θ_h increases in Figs. 4.3e and f, the support in the $\phi_d = 0$ and π directions decreases.

In Fig. 4.3a and Fig. 4.3d, Brewster's angle in θ_d can clearly be seen where the diattenuation magnitude reaches unity and the sign on the lower two diagonal Mueller elements shifts from negative to positive. These two planes have the most familiar interpretation. The interpretation of other pBRDF cross sections is made more complicated by the transverse plane rotations into the local basis. However, features from one planar cross section can be identified in others, such as the ring of high diattenuation near Brewster's angle in θ_d from Fig. 4.3d showing up at the base of each cross section in Figs. 4.3a-c. The features shown in Fig. 4.3c can also be seen along the vertical line through each of the cross sections in Figs. 4.3d-f.

In all of the cross sections, MMs which have the same θ_h and θ_d coordinates but ϕ_d related by $\pm\pi$ obey the reciprocal relation described in Sect. 4.2. In the cross sections in Figs. 4.3a-c, such geometries are mirrored left-to-right about the center vertical axis. In Figs. 4.3d-f, these reciprocal geometries are mirrored through the origin.

4.3   Evaluation of Acquisition Protocols

An efficient pBRDF acquisition captures MM data at as many unique scattering geome-
tries as possible with as few angular steps of the goniometer as possible. The discretized
scattering geometries sampled at each goniometer position can be calculated before image
acquisition in order to compare different protocols for a given object shape. The camera
and goniometer parameters for the RGB950 were used for the pre-acquisition evaluation
and optimization of scattering geometries and subsequent measurement demonstration.[58]
Parameters for the simulated image acquisition are listed in Tab. 4.2.

Table 4.2: Rusinkiewicz triplets in Fig. 4.4 depend on the imaging polarimeter and object.

Instrument	Focal length	Pixel pitch	Source distance	Camera distance
	19.61 mm	11.00 microns	90.00 cm	16.48 cm
Object	Sphere radius	Cylinder radius	Cylinder length	Plane edge length
	2.54 cm	2.54 cm	12.70 cm	10.16 cm

Figure 4.4 shows the sampling of scattering geometries for various object shapes when
the camera and light source are separated by $\Omega = 55°$. The central three columns show θ_h,
θ_d, and ϕ_d as they are sampled in the image plane of the camera. The rightmost column
shows how those sampled populate the reflection region. The sphere, plane, and cylinder
were used because they have simple analytic solutions for intersecting their surfaces with
rays. It is clear from Fig. 4.4a that the sphere image has the most unique Rusinkiewicz
angles. This conclusion is consistent with the literature and is the justification for using
spherical targets in image-based scalar and polarized BRDF acquisition.[8,61] Additionally,
the rotational symmetry of the sphere removes the need to carefully orient the sample
(positioning relative to the rotation axis of the goniometer is still necessary). It can be
challenging to find perfect spheres of many materials of interest however, such as paper.
In the case of such materials, it may be necessary to use another target shape at the cost
of requiring more goniometer measurements.

Figure 4.4b shows the Rusinkiewicz angles captured in an image of a planar sample.
Despite filling a greater part of the field of view as compared to the sphere, significantly
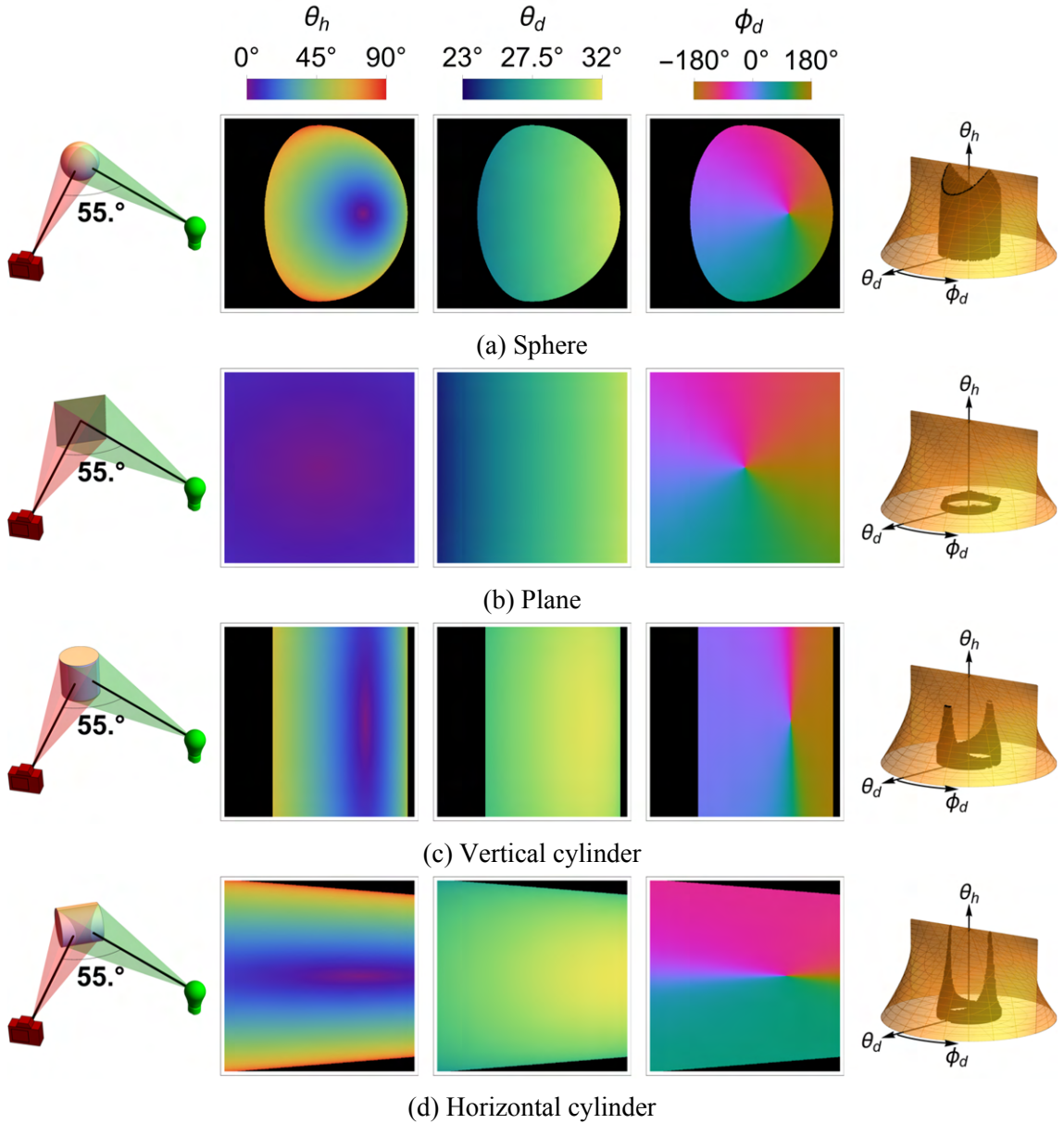
Figure 4.4: At goniometer position $\Omega = 55°$, the per-pixel Rusinkiewicz triplets for (a) sphere, (b) flat square, (c) vertical cylinder, and (d) horizontal cylinder target shapes. The diagrams showing the capture setup (left column) show the correct orientation of each object but are not to scale. The central three columns show θ_h, θ_d, and ϕ_d as they are sampled in the image plane. The discrete geometries with at least one sample are shown populating the reflection region (right column). The sphere provides the most unique geometries within a single image while the plane provides the fewest. The cylinders provide an intermediate number of unique geometries. Parameters for the simulated capture setups are listed in Tab. 4.2.

fewer unique scattering geometries are sampled due to the slow variation in θ_h. Fully populating the reflection region would require performing multiple measurements at the same goniometer position but with the plane's surface normal at different orientations. Figures 4.4c and 4.4d show the Rusinkiewicz angles imaged for a cylinder with two different orientations. An image of the cylinder populates more points in the reflection region than the plane, but not as many as the sphere. A single image of a cylinder has greater variation in θ_h than the plane but multiple cylinder orientations at each goniometer position are still required to fully populate the reflection region. A cylindrical target may be a useful alternative to a plane for materials which cannot be made into spheres.

The particular shapes for which Rusinkiewicz angle images were calculated are those which have simple analytic equations for intersecting rays with their surfaces. Polarization imaging with structured light can simultaneously retrieve polarization data as well as shape information, which can facilitate the pBRDF measurements from objects with more general shapes.[57]

For the pBRDF presented in this work, we use a red 3D printed sphere as the material sample. The sphere was 3D printed using selective laser sintering. Variations in surface texture and deviations from being perfectly spherical are potential sources of error discussed in the measurement results. To compare different goniometer sequences, goniometer positions Ω from 20° to 160° are evenly spaced and the percent of discretized geometries in the reflection region which have at least one MM measurement is calculate. The RGB950 camera cannot get closer than $\Omega = 20°$ from the source, so about 3.6% of the volume is inaccessible. For RGB950 measurements of the 2 inch diameter sphere, the largest possible goniometer angle is $\Omega = 160°$ where the view of the sphere is almost completely in shadow.

Figure 4.5 shows the percentage of the total discretized geometries which have at least one measured MM for different number of goniometer positions. Fill factor increases roughly linearly at a rate of 0.95% per additional geometry until around 90 where the rate transitions to 0.035% per additional geometry. Based on the diminishing returns, we selected 92 measurements as the number of evenly-spaced goniometer positions.

It is worth reiterating that this result is based on the size of the sphere, the distances
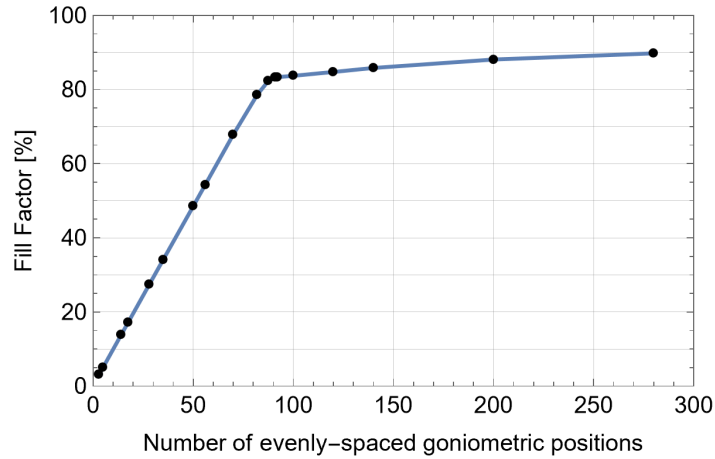
Figure 4.5: Fraction of discretized geometries filled for a given number of sphere measurements at evenly spaced goniometric steps from $\Omega = 20°$ to $160°$. The slope starts out at 0.95% per additional goniometer position, then becomes 0.035% per additional goniometer position after 92 positions.

from the camera and source to the sphere, and the effective focal length of the camera, reported in Tab. 4.2. Another polarimeter setup could potentially achieve a higher fill fraction in the same number or fewer goniometer positions. For example, moving the source closer to the object is expected to increase the range of θ_d appearing within a given image. Changing the distance from the object to the camera (as well as the magnification to properly fill the image) would also affect the sampled Rusinkiewicz angles. In these cases, the same method of calculating the point of diminishing returns could be applied to determine an efficient goniometric measurement protocol. The method could also be applied to a non-uniform discretization of the reflection region. Such non-uniform discretizations are advantageous for efficiently sampling pBRDFs which have rapidly varying scattering behavior near certain geometries (*e.g.* specular reflection) but slowly varying behavior for other geometries.[8,26,61] However, for non-uniform discretizations, uneven goniometer spacing may be required to efficiently sample the denser regions.

4.4 Measurement Demonstration

The pBRDF acquisition protocol described in the previous section was performed for a red 3D printed sphere. Data were taken at two of the RGB950's visible wavebands: 451 ± 19

nm and 662±11 nm.[58] These data are available in Dataset 2.[41]

Figures 4.6 and 4.7 show measured normalized MM data at 662 nm and 451 nm, respectively, on the same cross sections of the reflection region in Fig. 4.3. These MMs were rotated from the polarimeter transverse plane basis into the local basis using Eq. A.15. Unmeasured geometries were inpainted using trilinear interpolation for simplicity. In future work, customized techniques to inpaint/interpolate natively in cylindrical coordinates could be developed. At 662 nm, the majority of the Mueller elements have very low values due to strong depolarization. This is an expected result for a red object under red illumination per Umov's effect, where depolarization trends positively with albedo.[103] In all of the cross sections, larger Mueller element magnitudes appear toward the edges of the space. At 451 nm, Umov's effect predicts less depolarization for the red object which is evident from the larger Mueller element values. The pBRDF behaves much more like Fresnel reflection from microfacets as shown in Fig. 4.3. In the $\theta_h = 0$ plane in Fig. 4.7d, the peak in diattenuation and the sign flip in the lower two diagonal elements again show a Brewster's angle effect with respect to θ_d.

For geometries where θ_d is around $10°$ or less, there are no MM samples. These are geometries near retroreflection, which are not measurable in the RGB950 due to the RGB950 hardware preventing Ω from going less than $20°$. In the pBRDF, this region is populated only with inpainted data. For the 662 nm pBRDF in Fig. 4.6, this is less of a severe limitation because the MM elements are both lower in magnitude due to depolarization and more slowly varying. This is a more severe limitation for the 451 nm pBRDF in Fig. 4.7, where higher frequency variations such as in the center of the m_{11} and m_{22} elements in Fig. 4.3c are not captured. In the m_{11} and m_{22} elements of Fig. 4.7a, the inpainting artifacts produce regions with the incorrect sign. This result highlights the fact that the measurement protocol designed in the previous section, which prioritized fill factor, is most appropriate when the pBRDF is either slowly varying or when there is no prior knowledge about the frequency content of the pBRDF.

The empirical pBRDFs at both wavelengths show unexpected variations for higher values of θ_h. These are evident to visual inspection on Fig. 4.7c near the top of each Mueller element where the sign changes rapidly. These errors may be due to the fact
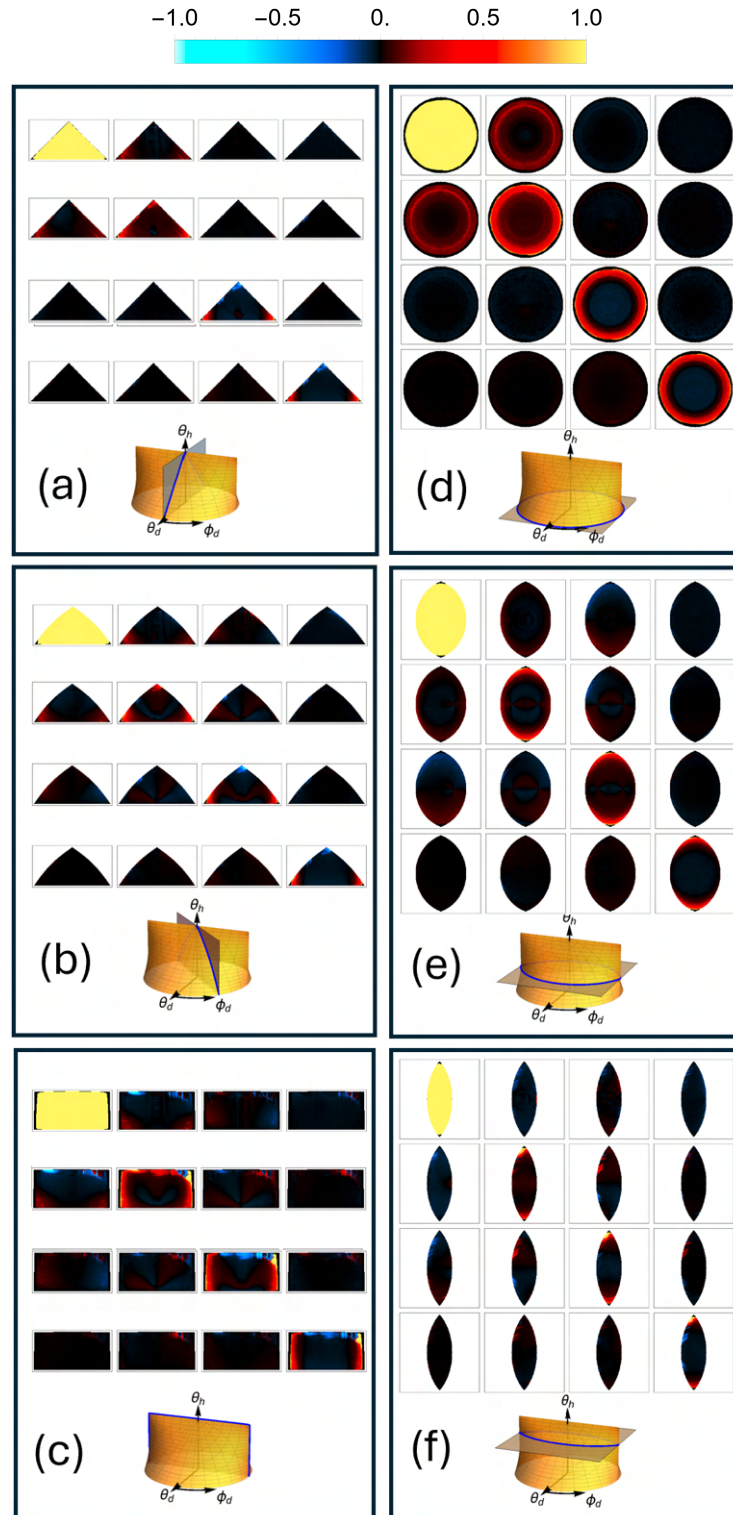
Figure 4.6: Cross sections of the measured 662 nm pBRDF displayed as MM images for the planes where (a) $\phi_d = 0°/180°$, (b) $\phi_d = 45°/225°$, (c) $\phi_d = 90°/270°$, (d) $\theta_h = 0°$, (e) $\theta_h = 30°$, and (f) $\theta_h = 60°$. The region of the pBRDF where $\theta_d < 10°$ is inpainted due to the polarimeter being unable to measure geometries at or near retroreflection.
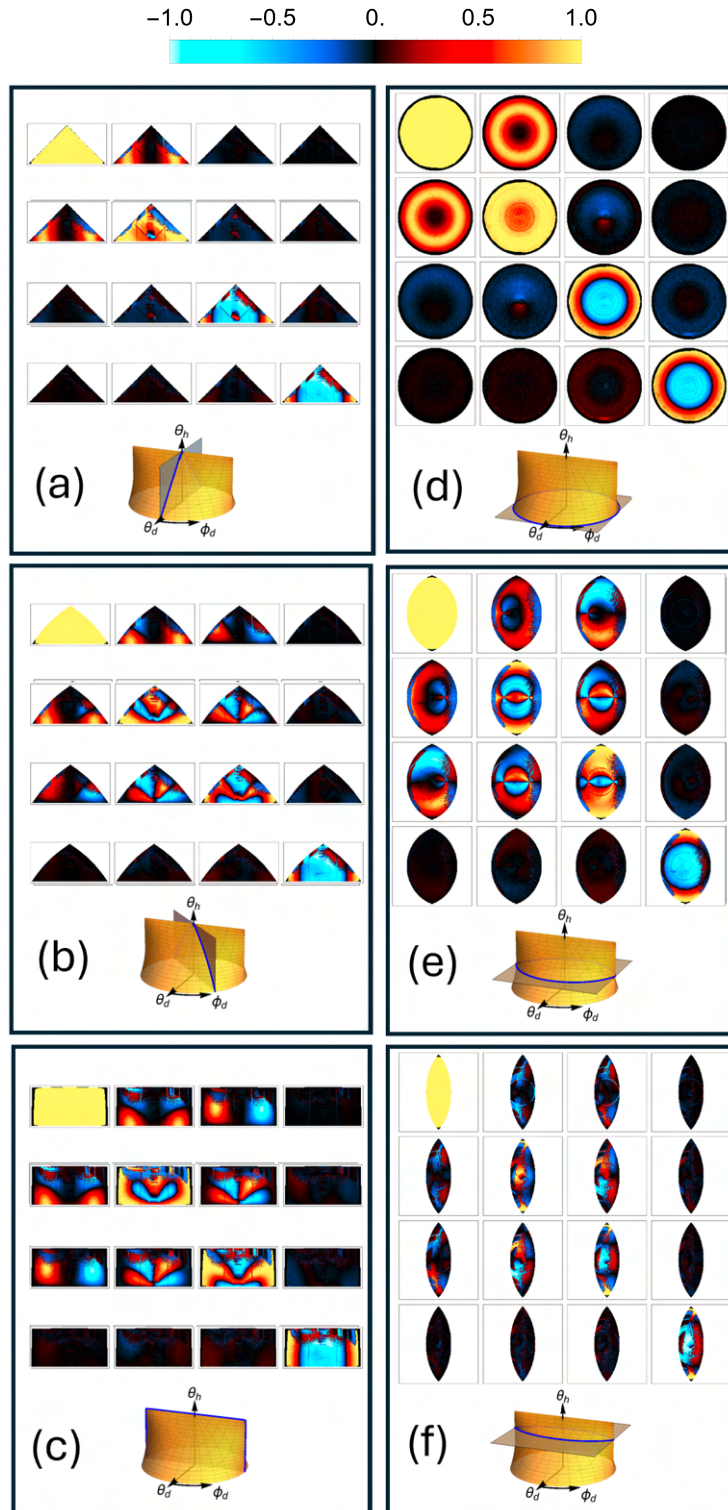
Figure 4.7: Cross sections of the measured 451 nm pBRDF displayed as MM images for the planes where (a) $\phi_d = 0°/180°$, (b) $\phi_d = 45°/225°$, (c) $\phi_d = 90°/270°$, (d) $\theta_h = 0°$, (e) $\theta_h = 30°$, and (f) $\theta_h = 60°$. The region of the pBRDF where $\theta_d < 10°$ is inpainted due to the polarimeter being unable to measure geometries at or near retroreflection.

that the large values of θ_h exist near the edges of the illuminated part of the sphere, see Fig. 4.4a. The association of calculated Rusinkiewicz angles to measured image data is most sensitive to errors in object shape and positioning near these edges. These regions also have the fewest MM samples during the goniometer position sequence based on how little of the image they subtend. Pixels may be misregistered due to the object not being perfectly spherical or positioned at the center of goniometric rotation. These errors are most severe for geometries which are sampled at the edges of the sphere in the image. In the most extreme case, data may be collected from pixels which do not see the object at all. The quantity of erroneous MM samples may compounded during inpainting. The severity of these artifacts on data quality could be assessed with respect to physics-based rendering but there is currently no rendering engine which can accept as input the pBRDF in cylindrical coordinates. It is also worth noting that these errors are those which cause the most deviation from the pBRDF exhibiting the reciprocal behavior described in Sect. 4.2. In principle, some of the erroneous data points could be replaced with data from the reciprocal positions in the pBRDF but prior knowledge would be required to determine which data points need correction.

4.5   Conclusions

In this work we presented a new approach to tabulation of empirical pBRDFs of isotropic surfaces. In principle, this approach would offer benefits to scalar-valued BRDFs as well. The tabulation is used to compare and select the sampling of scattering geometries. Acquiring an empirical pBRDF involves MM measurements at many scattering geometries and wavebands. The significant time and storage resources required to measure and tabulate this data motivates the development of efficient representation and acquisition protocols.

The conventional approach for tabulating the MM measurements is to interpret the three Rusinkiewicz angles which parameterize the pBRDF as forming a Cartesian space, see Fig. 4.2a. MM data samples are associated with discrete points on the Cartesian space, however this representation contains redundant points which correspond to the same phys-

ical scattering geometry as well as points which do not correspond to external reflection. Rather than interpret the three Rusinkiewicz angles as Cartesian coordinates, we interpret them as cylindrical coordinates, see Fig. 4.2b. This has the benefit of increasing the compactness and convexity of the region of reflection geometries. When changing from Cartesian to cylindrical coordinates, the volume of the reflection region is reduced by 40%, see Tab. 4.1. This reduction in volume is most efficiently leveraged by omitting non-reflection geometries. Going from the enclosing parallelepiped (the state-of-the-art) to the enclosing cylinder reduces the volume by 21% and staying in Cartesian coordinates but excluding non-reflection geometries reduces the volume by 38%. Going from the enclosing parallelepiped to cylindrical coordinates with non-reflection geometries reduces the volume by 63%. It is also worth noting that, by enforcing reciprocity the pBRDF becomes π-periodic in ϕ_d and the reflection region can be made even smaller in cylindrical coordinates by taking the azimuth angle to be $2\phi_d$.

While multiple approaches for non-uniform BRDF and pBRDF techniques appear in the literature, uniform pBRDF sampling is performed to facilitate comparison to the KAIST database of indoor materials.[8,26,61] To determine an efficient uniform sampling protocol, we used the percentage of discrete geometries which were sampled at least once during a set of goniometric MM measurements. The choice to use the number of evenly spaced goniometric positions where the fill percentage began to have diminishing returns was application-agnostic and only served to maximize unique geometries while minimizing measurement time. Practically, the requirement on sampling density depends on the optical properties of the material and the robustness of the polarimeter to noise. For a slowly-varying pBRDF, fewer geometries may be sampled with an acceptable loss of accuracy during inpainting. For a rapidly varying pBRDF, more goniometric positions may be required than the presented method suggests. Finer sampling of scattering geometries will improve the accuracy of the inpainted result if the measurement noise is appreciable.

CHAPTER 5

pBRDF Models

5.1 Analytic Polarized Scattering Models

Scattering by optical components is generally minimized by design, but everyday materials such as fabric or opaque plastics tend to have strongly diffuse scattering properties. Depolarization, which is closely related to scattering, is therefore a useful property to consider when studying such materials.

Both BRDF and pBRDF models frequently contain a specular component that describes light scattered from the surface of a material and a diffuse component attributed to light scattered from within the material.[107] The polarization of the specular component, more accurately called the first-surface reflection component, is commonly modeled as Fresnel reflection from hypothetical sub-resolution microfacets.[48, 64, 80, 97] Early work on polarized light scattering assumed that the diffuse component becomes completely depolarized such that diffuse contributions to reflection can be eliminated by using a polarizer.[106] Although first-surface reflection tends to produce greater polarimetric modulation, it is generally incorrect to assume that diffuse reflection is completely depolarizing (*i.e.*, the degree of polarization, see Eq. 2.6, for any input state becomes zero).[4] Instead, the diffuse term may be partially polarizing. Many shape-from-polarization approaches consider both first-surface and diffuse polarized light scattering but use either a purely specular or purely diffuse pBRDF for a given material.[4, 24, 43] Data-driven models have had success with a decomposition into diffuse and specular terms as input into neural networks.[6, 108]

More rigorous pBRDF models characterize polarimetric light scattering in terms of a combination of first-surface and diffuse polarized components. The pBRDF model introduced by Baek et al. consists of a first-surface microfacet term and a polarized diffuse term.[7] The diffuse term describes Fresnel transmission into, depolarizing scattering within, and Fresnel transmission out of the material. In such a model, depolarization arises

from both the diffuse reflection term and the opposing polarizance orientations between the first-surface microfacet and diffuse terms. Kondo et al. extended this model by including an ideal depolarizer as an independent third term.[45]

The objective of this Chapter is to introduce a TD-MM model that efficiently describes measurements of spherical objects in a DRR Mueller polarimeter. The model is demonstrated performance to predict MM at different geometries and wavebands. In the subsequent Chapter, the accuracy of this model is assessed as performance in the task of estimating ξ_0 from an assumed form of $\widehat{\mathbf{M}}_0$ and partial polarimetric measurements.

5.2 Dominant Mueller-Jones Models

5.2.1 First-Surface Reflection Component

The first-surface reflection, frequently referred to as specular reflection, is commonly modeled as Fresnel reflection from a hypothetical sub-resolution feature called a microfacet (the term first-surface reflection will be used going forward so that specular may be reserved to describe scattering configurations where $\theta_h = 0°$).[80] The microfacet is oriented such that it satisfies the Law of Reflection for a given pair of input and output ray directions.

This model is conceptually simple, however, implementation is complicated by the need to consider rotations in the plane transverse to the direction of propagation. The orientations of s- and p-polarizations in space vary based on the scattering geometry, and the orientations of horizontal and vertical for both the input and output coordinate systems are implicit parameters of the Jones matrix (JM) or MM. The JM for Fresnel reflection from a microfacet $\mathbf{F}$ is

$$\mathbf{F}_{n_\lambda}(\widehat{\boldsymbol{\omega}}_i, \widehat{\boldsymbol{\omega}}_o) = \begin{bmatrix} \widehat{\mathbf{x}}_{PSA} \\ \widehat{\mathbf{y}}_{SA} \end{bmatrix} \begin{bmatrix} \widehat{\mathbf{s}}_o \\ \widehat{\mathbf{p}}_o \end{bmatrix}^\mathsf{T} \begin{bmatrix} r_s(n_\lambda, \theta_d) & 0 \\ 0 & r_p(n_\lambda, \theta_d) \end{bmatrix} \begin{bmatrix} \widehat{\mathbf{s}}_i \\ \widehat{\mathbf{p}}_i \end{bmatrix} \begin{bmatrix} \widehat{\mathbf{x}}_{PSG} \\ \widehat{\mathbf{y}}_{PSG} \end{bmatrix}^\mathsf{T} . \qquad (5.1)$$

Definitions for all of the vectors appearing in this equation can be found in Appendix A. The leftmost and rightmost pairs of matrices each combine to orthogonal matrices which represent rotations in the plane of the electric field. These are left in terms of vectors to

(a) First surface reflection MJM   (b) Diffuse polarization MJM
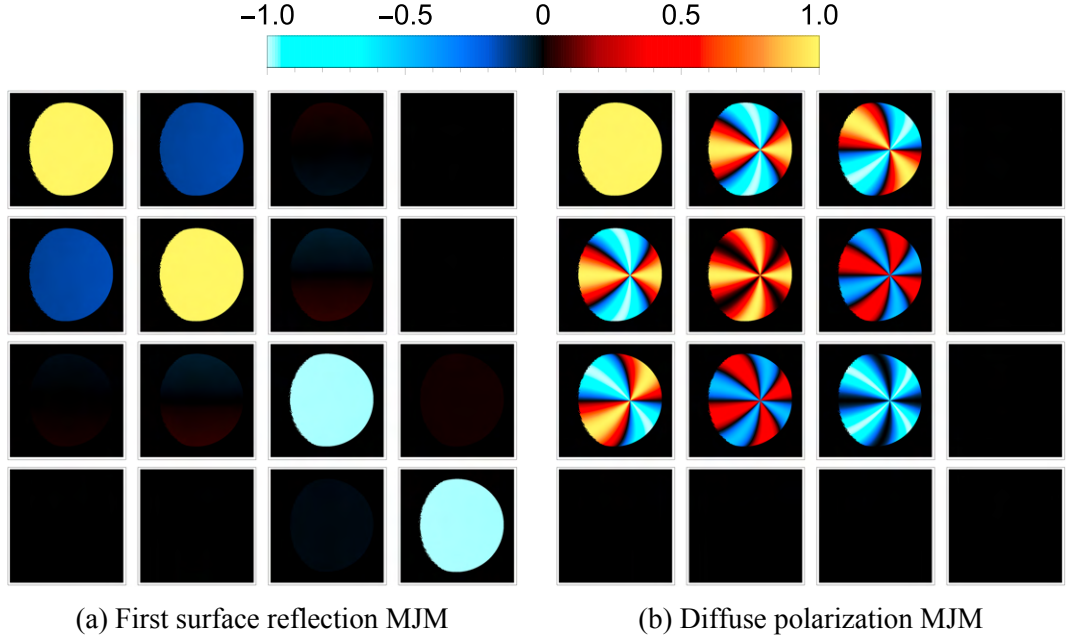
Figure 5.1: MM images of (a) the first-surface reflection model in Eq. 5.1 and (b) the diffuse model in Eq. 5.2 evaluated over a sphere in the same scattering configuration as in Fig. 5.2. The left side of the sphere is obscured by shadow. The first-surface reflection component is modeled as Fresnel reflection from microfacets, so the polarized scattering behavior does not depend directly on the surface normal. For this reason, the diattenuation and polarizance orientations do not follow the surface of the sphere. The non-zero values present in the m_{12} and m_{21} elements of (a) and (b) represent changes in the polarization state due to geometric effects rather than retardance.

emphasize the change in coordinate basis, but are commonly represented with conventional rotation matrices.[7,14,45,54] The Fresnel coefficients r_s and r_p, see Eq. 2.4, depend on the refractive index ratio n_λ and the angle of incidence onto the microfacet θ_d.[80] The values used for n_λ are presented in Tab. 5.1.

Equation 5.1 is invariant to the surface normal since Fresnel reflection is only defined for a normal vector that is halfway between the illumination and view vectors (*i.e.*, a microfacet). Instead, the Fresnel term only depends on the incident and scattered ray directions $\widehat{\omega}_i$ and $\widehat{\omega}_o$. The diattenuation magnitude depends only on θ_d, which is half of the angle between $\widehat{\omega}_i$ and $\widehat{\omega}_o$. The angle θ_d varies slowly over the sphere, as shown in the example geometry in Fig. 5.2, so the diattenuation magnitude also varies slowly. Variation in the diattenuation orientation is caused by variation in the orientation of *s*-

and p-polarizations relative to the input and output coordinate systems. Both the s- and p-directions and the input and output coordinate systems vary over the field of view. These coordinate transforms lead to coupling between linear polarization states which can be observed faintly in the center 2×2 elements of the MM image in Fig. 5.3a. This should not be confused with true circular retardance, as it results from geometric effects rather than a relative phase difference between polarization states. When the microfacet surface normal $\widehat{\mathbf{h}}$ and the macroscopic surface normal $\widehat{\mathbf{n}}$ are coplanar (and therefore also coplanar with $\widehat{\boldsymbol{\omega}}_i$ and $\widehat{\boldsymbol{\omega}}_o$), there is no coupling between linear states caused by geometric effects. This can be noted in the MM image of a purely Fresnel reflection $\widehat{\mathbf{M}}_0$ is shown in Fig. 5.1a, where there is a dark band through the center of the m_{12} and m_{21} elements. The geometries in this region are referred to as "in-plane" scattering.

It is more correct to think of $\mathbf{J}_s(\widehat{\boldsymbol{\omega}}_i, \widehat{\boldsymbol{\omega}}_o)$ as a first-surface reflection model rather than a microfacet model. This is because the distribution of microfacet normals and adjacency effects are not explicitly included in $\mathbf{J}_s(\widehat{\boldsymbol{\omega}}_i, \widehat{\boldsymbol{\omega}}_o)$. Conventional microfacet models use distributions on the orientations of the microfacets to model surface roughness.[3,10,12,105] Adjacency effects, specifically shadowing and masking, and the microfacet distribution can be interpreted as dictating the likelihood of an incident ray undergoing first-surface reflection toward the detector.[34] This likelihood corresponds to the relative contribution of first-surface reflection to other terms in the pBRDF model. In this work, the adjacency effects, microfacet distribution, and other properties due to texture are absorbed into other parameters in the model. Depolarization due to texture is captured by the dominant eigenvalue $\xi_0(\widehat{\boldsymbol{\omega}}_i, \widehat{\boldsymbol{\omega}}_o)$ from Eq. 2.18. The first-surface-to-diffuse weighting function captures texture-dependent non-depolarizing properties, and is discussed in Sect. 5.2.3.

5.2.2 Diffuse Reflection Component

The diffuse reflection component is modeled as

$$\mathbf{S}(\widehat{\boldsymbol{\omega}}_i, \widehat{\boldsymbol{\omega}}_o, \widehat{\mathbf{n}}) = \begin{bmatrix} 1 & 0 \\ 0 & -1 \end{bmatrix} \mathbf{R}(\phi_d) \begin{bmatrix} 1 & 0 \\ 0 & 0 \end{bmatrix} \mathbf{R}(-\phi_d), \tag{5.2}$$

where the rightmost three JMs represent a polarizer with unit diattenuation and a transmission axis oriented at ϕ_d. This matrix has a diattenuation orientation in the plane spanned by the surface normal $\widehat{\mathbf{n}}$ and $\widehat{\boldsymbol{\omega}}_o$, a pattern which is centered about the point on the sphere where $\theta_h = 0°$, as shown in Fig. 5.2a. When left multiplied by the reflection matrix, the $45°$ and $135°$ polarization states are reversed. This pattern being centered about $\theta_h = 0°$ is consistent with the $\widehat{\mathbf{m}}_0$ images observed from DRR measurements of spheres (see Fig. 5.3c); however, it does mark a departure from many other diffuse polarization models. In models such as the one proposed by Atkinson and Hancock, the orientation of the diffuse term is centered about the central camera axis.[4]

5.2.3 Mixed Dominant Mueller-Jones Matrix Model

Previous work demonstrated extrapolating MM images using a purely Fresnel reflection model for the dominant MJM, but this work was performed on flat objects which have a smaller range of scattering geometries.[36,40] The objects and scattering geometries described in this work require models for $\widehat{\mathbf{M}}_0$ that introduce a polarized diffuse reflection term. This term is characterized by a diattenuation orientation that depends on the surface normal. However, the dominant MJM necessarily must be non-depolarizing, and simply summing different MMs, in general, introduces depolarization.

To create a mixed polarization model without introducing depolarization, the individual first-surface and diffuse components are combined as Jones matrices as in

$$\mathbf{J}(\widehat{\boldsymbol{\omega}}_i, \widehat{\boldsymbol{\omega}}_o, \widehat{\mathbf{n}} | n_\lambda, a_\lambda, b_\lambda) = \mathbf{F}_{n_\lambda} + a_\lambda \sin^{b_\lambda}(\theta_h)\mathbf{S}(\widehat{\mathbf{n}}). \tag{5.3}$$

Here, the functional dependencies of $\mathbf{J}$ are separated into the scattering geometry and material parameters, with the separation notated by the vertical bar $|$. There are four material-dependent parameters which are constant for all scattering geometries: the real and imaginary components of the refractive index n_λ, and two parameters a_λ and b_λ, which control how the weight of the diffuse polarization term depends on scattering geometry. The four material parameters efficiently reduce the original six degrees of freedom for the diattenuation and retardance of the MJM. Both matrices on the right-hand-side depend on $\widehat{\boldsymbol{\omega}}_i$ and

Table 5.1: Material constants determined *ad hoc* to match the models to the observed MM measurements. These parameters are constant with respect to scattering geometry.

Material constants	451 nm	662 nm
$n_\lambda + i\kappa_\lambda$	$1.20 + 0.25i$	$1.30 + 0.08i$
a_λ	0.03	0.17
b_λ	2.5	2.0

$\widehat{\omega}_o$, but this has been dropped for brevity.

The surface normal of the material $\widehat{\mathbf{n}}$ (see Fig. 4.1) affects the diffuse but not Fresnel term. $\mathbf{F}(\widehat{\omega}_i, \widehat{\omega}_o, n_\lambda)$ is the first-surface reflection component modeled as Fresnel reflection based on refractive index ratio n_λ at wavelength λ, $\mathbf{S}(\widehat{\omega}_i, \widehat{\omega}_o, \widehat{\mathbf{n}})$ is the diffuse polarization term and is defined with unit throughput, so its relative weight as a function of scattering geometry is given by the sine function. $\mathbf{J}$ is converted to a MJM, normalized, and then used as $\widehat{\mathbf{M}}_0$ for a TD-MM model as in Eq. 2.18.

The values for the material properties are found in Tab. 5.1. These values, as well as the choice to use a sine function for the geometric dependence of the weight, were determined *ad hoc* to match the measurements. The weight function is modeled as only depending on θ_h because θ_h is a measure of deviation from a specular scattering configuration. The sine function was chosen for the weight functions based on the observation that Fresnel reflection-like behavior dominates for near-specular scattering geometries (where θ_h is small) and diffuse polarization behavior tends to become dominant away from specular geometries. The coefficients and powers in these equations were empirically chosen to match the diattenuation trends observed in measurements. The functional dependencies of parameters in the mixed model are summarized in Tab. 5.2.

5.3 Dominant MJM Measurement-Model Comparison

The measured and modeled $\widehat{\mathbf{M}}_0$ are compared by their diattenuation magnitudes D and orientations ψ. Diattenuation is represented in the top row of a MM. In Fig. 5.5 ψ and in Fig. 5.6 D are compared at $\Omega = 35°$ based on the Rusinkiewicz coordinates from the DRR measurements rather than with the look-up table method used in Sect. 6.4.2 because the

Table 5.2: Dependencies of parameters which appear in the TD mixed polarization model.

Parameter	Dependencies
ξ_0	$\widehat{\boldsymbol{\omega}}_i,\ \widehat{\boldsymbol{\omega}}_o,\ \widehat{\mathbf{n}},\ \lambda$
M_{00}	$\widehat{\boldsymbol{\omega}}_i,\ \widehat{\boldsymbol{\omega}}_o,\ \widehat{\mathbf{n}},\ \lambda$
$\mathbf{F}$	$\widehat{\boldsymbol{\omega}}_i,\ \widehat{\boldsymbol{\omega}}_o,\ n_\lambda,\ \kappa_\lambda$
$\mathbf{S}$	$\widehat{\boldsymbol{\omega}}_i,\ \widehat{\boldsymbol{\omega}}_o,\ \widehat{\mathbf{n}}$
$\widehat{\mathbf{m}}_0$	$\mathbf{S},\ \mathbf{F},\ \widehat{\boldsymbol{\omega}}_i,\ \widehat{\boldsymbol{\omega}}_o,\ \widehat{\mathbf{n}},\ a_\lambda,\ b_\lambda,\ n_\lambda,\ \kappa_\lambda$
$\mathbf{m}_{ID}$	n/a

(a) Sphere θ_h (b) Sphere θ_d (c) Sphere ϕ_d

(d) Bunny θ_h (e) Bunny θ_d (f) Bunny ϕ_d
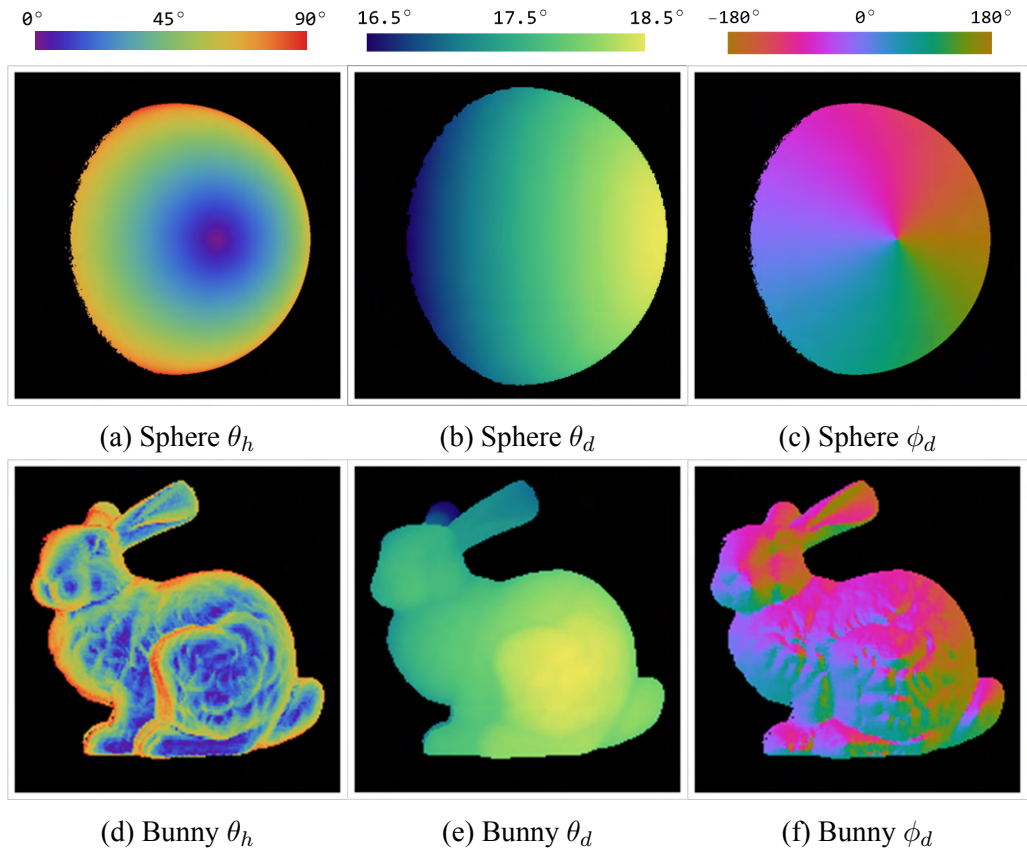
Figure 5.2: Rusinkiewicz coordinates θ_h, θ_d, and ϕ_d are shown in (a-c), respectively, for a spherical object where $\Omega = 35°$ and in (d-f), respectively, a Stanford bunny. The Rusinkiewicz definitions are shown in Fig. 4.1. The regions in (a) and (d) where θ_h is small correspond to near-specular geometries where Fresnel reflection dominates.

models can be evaluated at arbitrary scattering geometries. These images were masked based on an intensity threshold, so the left side of the sphere is obscured in shadow. For

(a) Measured 451 nm   (b) Modeled 451 nm

(c) Measured 662 nm   (d) Modeled 662 nm
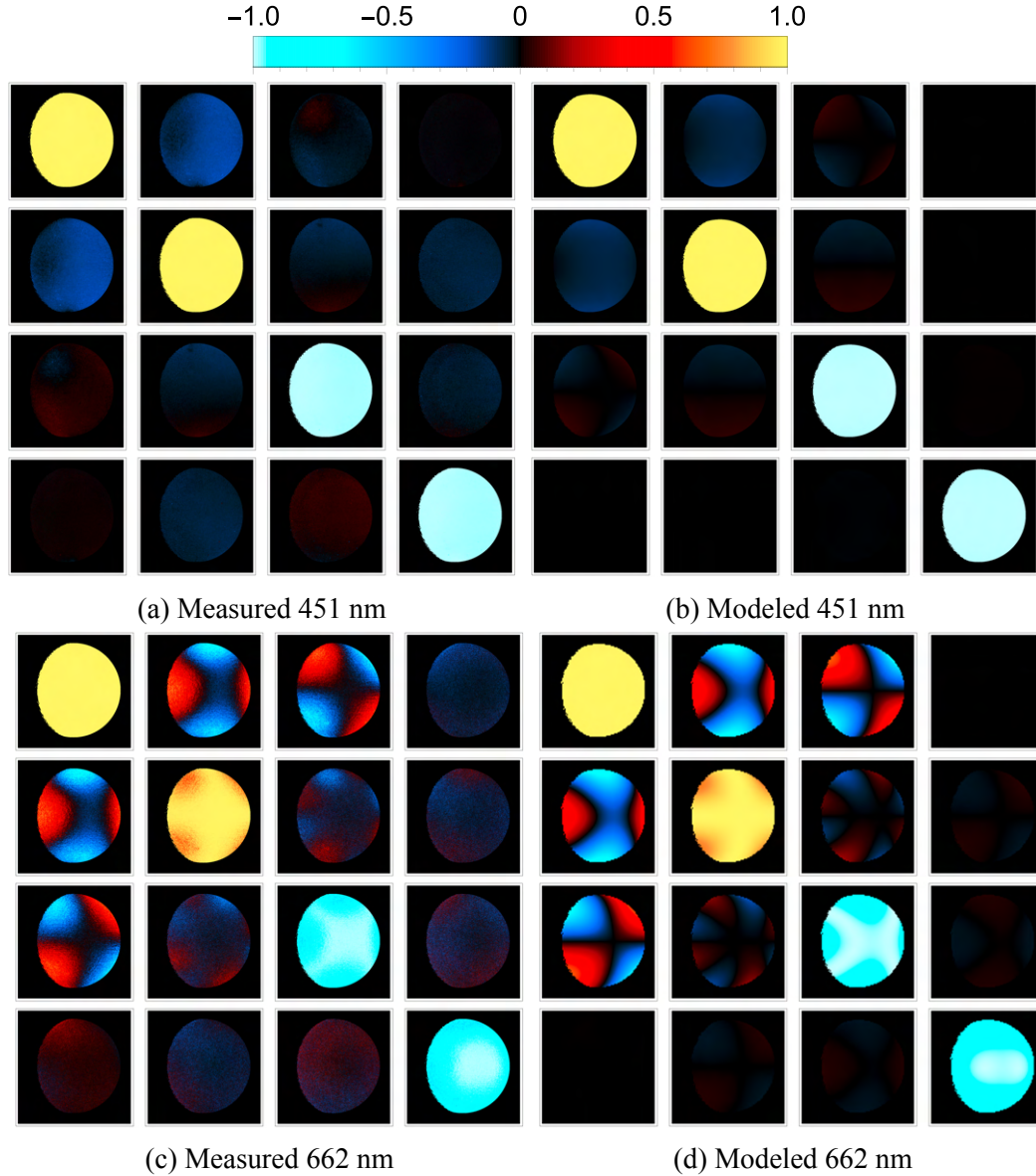
Figure 5.3: Comparisons of dominant MJM from DRR measurements at $\Omega = 35°$ and from the models (see Eq. 5.3) for a red sphere. At 451 nm (top) the low albedo creates lower diffuse scattering compared to 662 nm (bottom). Properties of the capture system are not included in the MJM images from the models, specifically the finite spatial and polarimetric resolutions. The raw measurements can be found in Dataset 3.[37]

higher values of Ω, more of the sphere is in shadow. Regions which are not in direct illumination are not expected to obey the simplified model presented in this work. In Fig. 5.5a and c, ψ is primarily vertical due to the low albedo case of 451 nm illumination

(a) Measured 451 nm

(b) Modeled 451 nm

(c) Measured 662 nm

(d) Modeled 662 nm
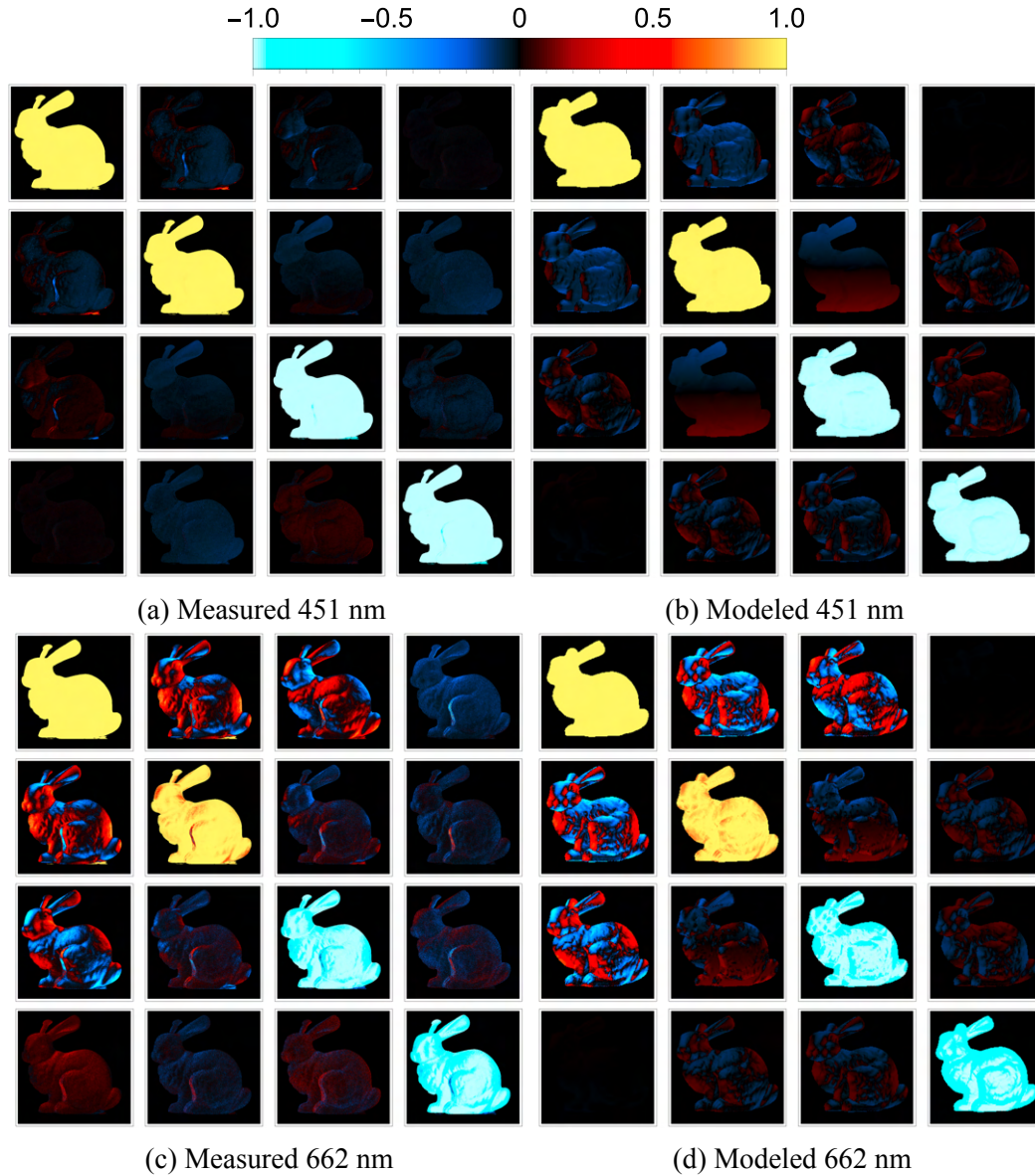
Figure 5.4: Comparisons of dominant MJM from DRR measurements at $\Omega = 35°$ and from the models (see Eq. 5.3) for a red bunny of the same material as the sphere. At 451 nm (top) the low albedo creates lower diffuse scattering compared to 662 nm (bottom). The model bunny MJM images are based on the geometry captured for the MM extrapolation from Stokes data experiment detailed in Chapter 6. There is therefore some inherent visual disagreement due to pose errors.

being dominated by Frensel reflection. In Fig. 5.5b and d, ψ is vertical in the center where Fresnel reflection dominates the near-specular geometries but the diffuse term dominates

away from specular, which is consistent with high albedo behavior.

(a) Measured ψ 451 nm   (b) Modeled $\widetilde{\psi}$ 451 nm   (c) ψ deviation 451 nm

(d) Measured ψ 662 nm   (e) Modeled $\widetilde{\psi}$ 662 nm   (f) ψ deviation 662 nm
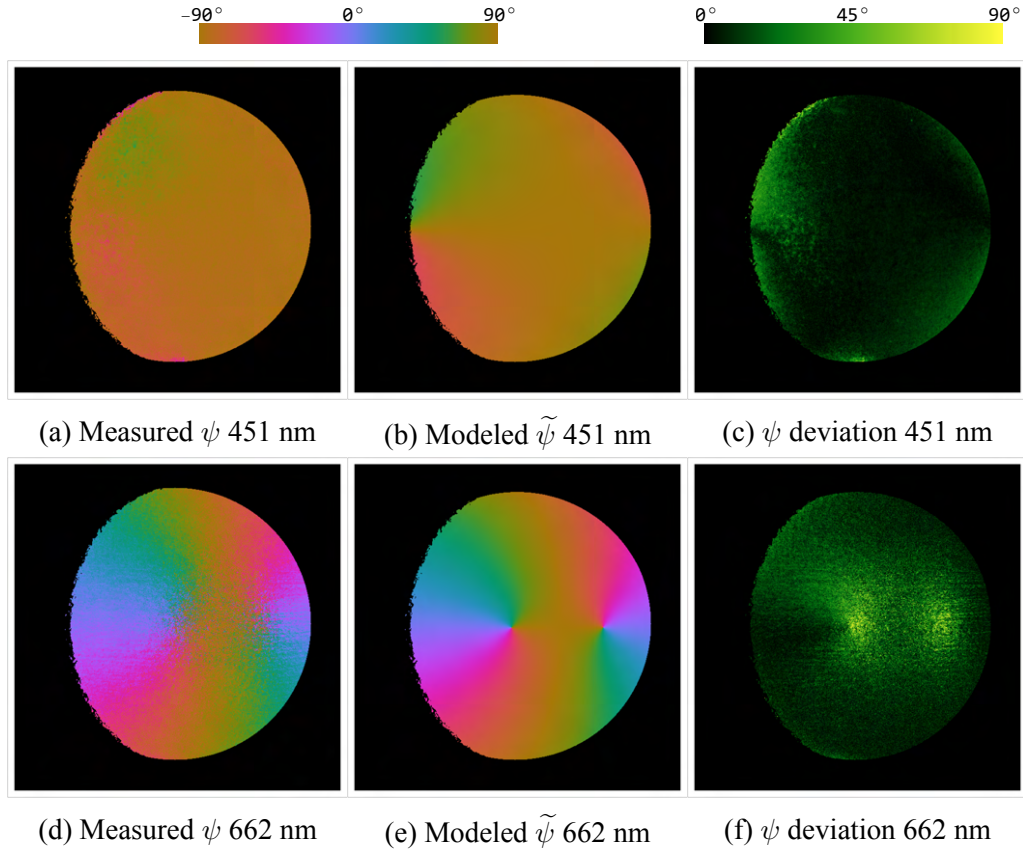
Figure 5.5: Diattenuation orientation ψ images of the $\widehat{\mathbf{m}}_0$ at $\Omega = 35°$ calculated from DRR MM polarimeter data at (a) 451 nm and at (d) 662 nm, and of the $\widehat{\mathbf{m}}_0$ models (b) 451 nm and at (e) 662 nm. The angle between the measured and modeled diattenuation orientations is shown in (c) and (f) for 451 nm and 662 nm respectively. The diattenuation orientation in (a) is primarily vertically oriented which is consistent with Fresnel reflection-dominated scattering as expected from a low albedo case. The orientation in (d) processes smoothly around the edge of the sphere which is consistent with diffuse polarization. This procession is radially oriented but with the 45°/135° components flipped due to the measurement being a reflection configuration. The center of the pattern shows vertically oriented diattenuation which suggests that Fresnel reflection dominates in that region. Agreement between the measurements and extrapolations is summarized according to Eq. 5.4 in Fig. 5.7a.

The agreement in ψ and D are summarized numerically in Fig. 5.7 according to their root-mean-squared-deviation (RMSD) values over the sphere at each acquisition geometry

(a) Measured D 451 nm   (b) Modeled $\widetilde{D}$ 451 nm   (c) D deviation 451 nm

(d) Measured D 662 nm   (e) Modeled $\widetilde{D}$ 662 nm   (f) D deviation 662 nm
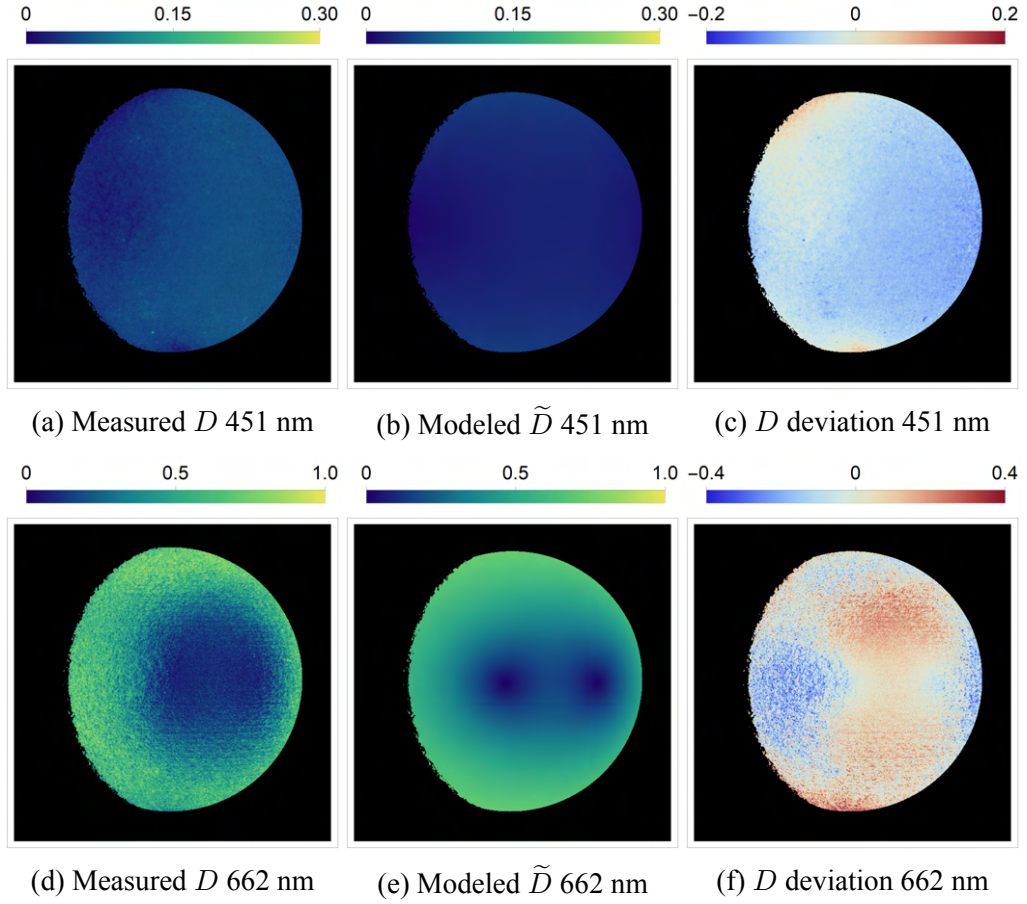
Figure 5.6: Diattenuation magnitude D images for the red sphere at $\Omega = 35°$. The ground truth from the DRR polarimeter measurements in (a) and the model in (b) at 451 nm are the low albedo case. The ground truth from the DRR measurements in (d) and the model in (e) at 662 nm are the high albedo case. The signed difference between measured and modeled D is shown in (c) and (f) for 451 nm and 662 nm, respectively. The agreement is summarized with respect to Ω in Fig. 5.7b. The two minima in (c) and (d), referred to as "neutral points," indicate the presence of at least two polarimetric processes which have comparable diattenuation magnitude and opposing orientations. These are hypothesized to be the first-surface and diffuse reflections.

Ω as in

$$
\begin{aligned}
\epsilon(\widetilde{\psi}, \psi) &= \sqrt{\frac{1}{K} \sum_{n=1}^{K} ||(\widetilde{\psi}_k - \psi_k)||^2} \\
&= \sqrt{\frac{1}{K} \sum_{n=1}^{K} \left[\frac{1}{2} \arccos\left(\widetilde{\mathbf{d}}_k \cdot \mathbf{d}_k \right) \right]^2},
\end{aligned}
$$

(5.4)

and

$$\epsilon(|\widetilde{D}|, |D|) = \sqrt{\frac{1}{K} \sum_{n=1}^{K} \left|\left||\widetilde{D}|_k - |D|_k\right|\right|^2} \tag{5.5}$$

where K is the total number pixels, and k is the pixel index. The dot product of the normalized linear diattenuation parameters, $\mathbf{d} = [D_1, D_2]/D$, is used to avoid angular phase wrapping effects caused by the fact that $\psi = 0°$ and $\psi = 180°$ describe the same orientation.

In Fig. 5.7a, the error in diattenuation orientation trends downward with Ω. The MJM term is dominated by first-surface reflection which has a simpler, easier to model orientation (primarily vertical). This is especially true for 451 nm, where first-surface reflection is overall more dominant due to its low albedo. The error for 451 nm hovers around $2°$ for large Ω. The more complicated diattenuation orientation pattern for diffuse reflection is matched less well as shown in the generally larger error for 662 nm. In Fig. 5.7b, the error in diattenuation magnitude is strictly lower for 451 nm than for 662 nm for all Ω. This is likely due to the simpler first-surface model dominating at 451 nm whereas the more complex diffuse model has a stronger contribution at 662 nm.

5.3.1 Sources of Disagreement

There are several potential sources of disagreement between the measurement and model as evaluated in the previous section. The first potential source is with respect to the model itself. The mixed polarized scattering model describes the dominant MJM in a TD model so there is no depolarization. However, if the measured MMs deviate significantly from TD, then the more complicated depolarization structure may be reflected in the MJMs in the Cloude decomposition described in Sect. 2.2.3. The terms in a general Cloude decomposition do not necessarily correspond to specific physical phenomenon.

Other potential sources of disagreement are related to the evaluation of the pBRDF model to generate the MM images. The response for each pixel is considered to behave as a single ray from the source which scatters from a perfect geometric sphere directly to the camera. In other words, the modeled MM images represent a point-wise evaluation of the pBRDF. In reality, the measurement by a single pixel is the sum of any inhomogene-

(a) Diattenuation orientation error

(b) Diattenuation magnitude error

(c) Average diattenuation magnitude
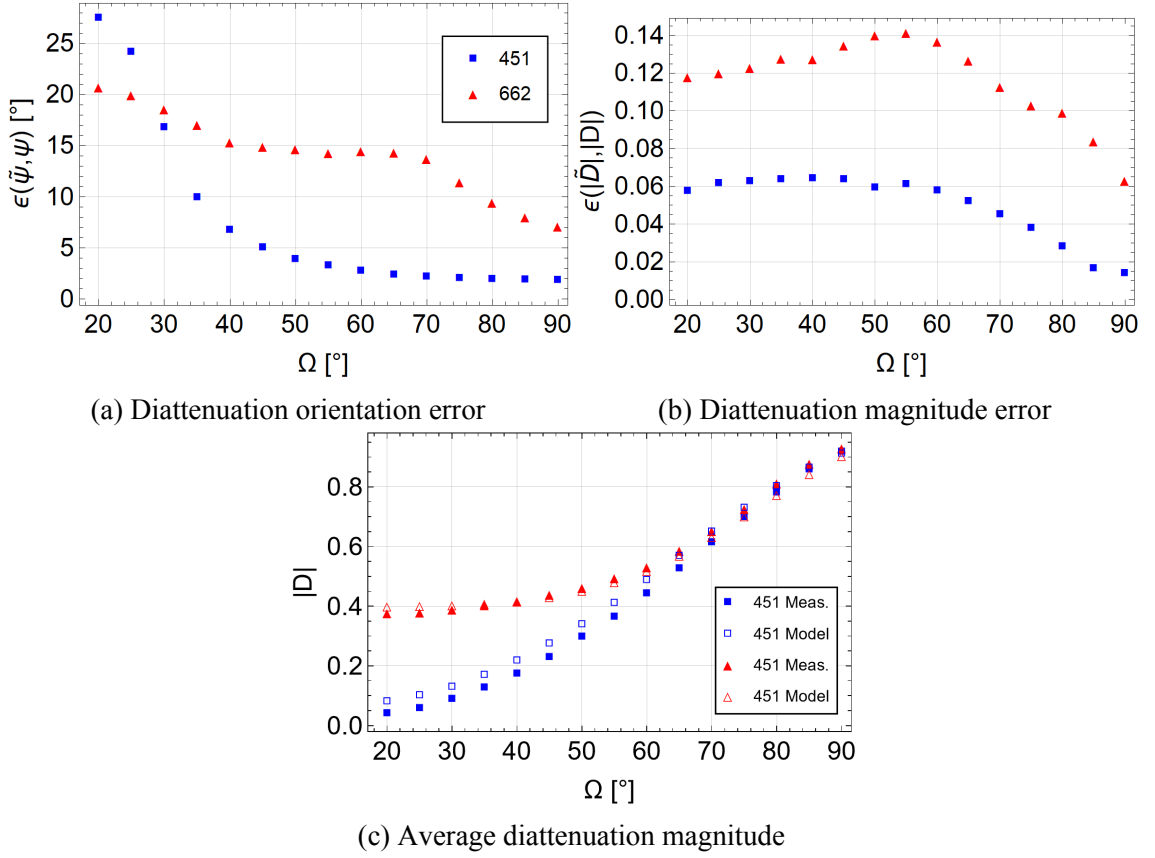
Figure 5.7: Error (a) in the diattenuation orientation $\widetilde{\psi}$ according to Eq. 5.4 and (b) in the diattenuation magnitude $\widetilde{D}$ according to Eq. 5.5 of the $\widehat{\mathbf{m}}_0$ models at 451 nm (blue squares) and 662 nm (red triangles). In (c), the diattenuation magnitude averaged over the image at each Ω for the measurements (solid markers) and models (open markers). The orientation error for 451 nm hovers around $2°$ for large Ω. The more complicated orientation pattern for diffuse reflection, which is more prominent at 662 nm, is matched less well as shown in the generally larger error for this high albedo case. The error in diattenuation magnitude is strictly lower for 451 nm than for 662 nm for all Ω. Again, this is likely due to the simpler first-surface model dominating at 451 nm whereas the more complex diffuse model has a stronger contribution at 662 nm. The errors shown in (a) and (b) are calculated per-pixel and then summarized with the RMSD whereas the magnitudes shown in (c) are averaged over the whole image.

ity over the instantaneous field-of-view of light that originated from an extended source. Some of the disagreement observable between the measured and modeled MM images in Fig. 5.4 may be explained by the rapid variation in geometry. Disagreement in the bunny MM images is also the result of pose issues exacerbated by the complex geometry.

The measured data are also affected by other real polarimeter properties such as measurement noise, finite bit depth, and polarimetric precision. In Fig. 5.5e, two singularities appear in the diattenuation orientation. At these exact points, the diattenuation magnitude shown in Fig. 5.6 are identically equal to 0, which is impossible to measure using a real optical system.

5.4   Conclusion

In contrast to precision optical components, depolarization is the dominant polarimetric property of everyday materials. The TD-MM pBRDF model lends itself to efficient descriptions for such depolarization-dominant materials. This work presents a closed-form Mueller-matrix valued pBRDF that is efficiently represented by a reduced parameter set: four wavelength-dependent material constants that define the polarization properties and a parameter for depolarization that depends on both geometry and wavelength. The material constants determine how the six degrees of freedom for diattenuation and retardance vary with geometry. This reduced parameterization assumes a TD coherency eigenspectrum and specifies two distinct non-depolarizing MJMs for first-surface and diffuse polarized light scattering. A microfacet Fresnel MJM is a popular polarized-light scattering model that is simple enough to describe first-surface scattering in many cases. However, polarization from diffuse scattering becomes non-negligible when a wider range of scattering geometries are considered.

In this work, the TD-MM pBRDF model is demonstrated over a large range of scattering geometries by combining polarized first-surface and diffuse contributions into a single MJM model. The first-surface MJM is Fresnel reflection based on microfacet theory, but purely radiometric effects such as shadowing and masking are ignored. The polarimetric properties of microfacet Fresnel reflections are invariant to the surface normal. However, the diffuse MJM is a diattenuator with orientation that strongly depends on the surface normal in a pattern centered where $\theta_h = 0°$ (*i.e.* specular reflection). This orientation is parallel to the plane of incidence with the caveat that $45°$ and $135°$ are flipped due to reflection. The magnitude of the diffuse contribution is determined by material constants.

The four material constants depend chiefly on the spectrally-dependent albedo of the material. The depolarization parameter depends on both the albedo and scattering geometry. The error in the TD assumption is inversely proportional to depolarization. For example, the red object used in this work is higher albedo at 662 nm compared to 451 nm, and the TD assumption is more appropriate for the high albedo case, as shown in Fig. 6.8.

Multi-angle MM measurements at two illumination wavelengths (for both high and low albedo conditions) of a red 3D printed material are compared to the original pBRDF model. The RMSD in diattenuation orientation for the modeled versus measured dominant MJM (see Fig. 5.7a) averaged over acquisition geometry was $7.49°$ and $14.29°$ at 451 nm (low albedo) and 662 nm (high albedo), respectively. The RMSD in diattenuation magnitude (see Fig. 5.7b) averaged over acquisition geometry was 4.96% at 451 nm and 11.73% at 662 nm. In the following Chapter, the MJM term of the original pBRDF model is evaluated at assumed values of the material constants, see Tab. 5.1, and the geometry-dependent depolarization parameter and the average reflectance are estimated from only linear Stokes images.

The TD-MM pBRDF model is intended to generalize to materials other than the red 3D printing material used for demonstration purposes in this work. By combining first-surface and diffuse polarized reflection in amounts that are material-dependent the model is designed to capture the most relevant features of polarized light scattering. To apply the model in Eq. 5.3 to a given material, the albedo-dependent material constants n_λ, a_λ, and b_λ must be determined. One method to estimate these values is MM imaging at a range of scattering geometries and least-squares fitting to the dominant process. This has the advantage of also providing a ground truth of the eigenspectrum to gauge the appropriateness of the TD assumption. Another approach, based on the *a priori* TD assumption, is to maximize the linear correlation coefficient between polarized measurements and measurements simulated from the MJM model defined by the material constants.

CHAPTER 6

Depolarization Measurement and Mueller Matrix Extrapolation

The objective of this work is to use prior knowledge about a material to extrapolate its MM from a small quantity of measurements. This is achieved by relating polarimetric measurements to the two degrees of a freedom of a TD MM model when the dominant process is known, rather than to relate measurements to the MM directly. The primary contribution of this work is a linear estimator for a MM's dominant coherency eigenvalue which requires as few as two polarimetric measurements. This is the first method known to the author for extrapolating depolarizing MMs with rank four coherency matrices from fewer than 16 measurements. A single illumination polarization state and a commercial DoFP linear Stokes camera is used for the partial polarimetric measurement, meaning that four measurements can be performed in a single snapshot acquisition. Experimental results using measurements taken in a snapshot configuration with a Sony Triton 5.0MP Polarization Camera are presented and compared to the RGB950.

6.1 Motivation

A handful of approaches for extrapolating MMs exist in the literature. In 2013 Swami et al. showed that, for a non-depolarizing MM, symmetry arguments can be applied to the linear partial MM to obtain the full $4{\times}4$ matrix.[95] In 2019, Ossikovski and Arteaga showed symmetry arguments for obtaining a full $4{\times}4$ MM from 12 elements where a row or column is missing[1] or from nine elements where a row and column are missing.[74] In the 12-element case, it is possible to recover a depolarizing MM but only if it obeys certain symmetry constraints and has only two non-zero coherency eigenvalues. All of these methods for extrapolating MMs from partial polarimetric data rely on strong prior information, as does the work presented here. In this Chapter, the enabling prior information is the knowledge or assumption of a pBRDF model for the dominant MJM in a TD

approximation.

6.2 Depolarization Measurement Method

A noise-free model for flux measurements $\mathbf{P}$ of a TD MM can be written as a linear system

$$\mathbf{P} = \mathbf{\Phi}^\mathsf{T}\boldsymbol{\beta}. \tag{6.1}$$

Here $\mathbf{\Phi}$ is a matrix with rows that are the measurement matrix $\mathbf{W}$ applied to the dominant process $\widehat{\mathbf{m}}_0$ and ideal depolarizer $\mathbf{m}_{ID}$ from the TD model as in

$$\mathbf{\Phi} = \begin{pmatrix} \mathbf{P}_0^\mathsf{T} \\ \mathbf{P}_{ID}^\mathsf{T} \end{pmatrix} = \begin{pmatrix} [\mathbf{W}\widehat{\mathbf{m}}_0]^\mathsf{T} \\ [\mathbf{W}\mathbf{m}_{ID}]^\mathsf{T} \end{pmatrix}, \tag{6.2}$$

and the elements of $\boldsymbol{\beta}$ are the weights in the TD model as in

$$\boldsymbol{\beta} = \begin{pmatrix} \beta_0 \\ \beta_{ID} \end{pmatrix} = \frac{4M_{00}}{3} \begin{pmatrix} \xi_0 - \frac{1}{4} \\ 1 - \xi_0 \end{pmatrix}. \tag{6.3}$$

It is worth reiterating that a benefit of the TD model is that the relative weights are controlled by a single depolarization parameter ξ_0, rather than varying independently. An estimate of the coefficients $\widetilde{\boldsymbol{\beta}}$ can be recovered with the Moore-Penrose pseudoinverse of $\mathbf{\Phi}^\mathsf{T}$ as in

$$\widetilde{\boldsymbol{\beta}} = [\mathbf{\Phi}^\mathsf{T}]^+ \mathbf{P} = \begin{pmatrix} \mathbf{W}\widehat{\mathbf{m}}_0 & \mathbf{W}\mathbf{m}_{ID} \end{pmatrix}^+ \mathbf{P}, \tag{6.4}$$

where $\mathbf{P}$ here is a vector of noisy flux measurements. Solving the system in Eq. 6.3 for the model parameters, estimates for $\widetilde{\xi}_0$ and $\widetilde{M}_{00}$ are

$$\widetilde{\xi}_0 = \frac{\frac{1}{4} + \widetilde{\beta}_0/\widetilde{\beta}_{ID}}{1 + \widetilde{\beta}_0/\widetilde{\beta}_{ID}}, \quad \widetilde{M}_{00} = \frac{3\widetilde{\beta}_0}{4\widetilde{\xi}_0 - 1} \tag{6.5}$$

where $\widetilde{\beta}_0$ and $\widetilde{\beta}_{ID}$ are the elements of $\widetilde{\boldsymbol{\beta}}$. $\widetilde{\xi}_0$ is the parameter of interest because it determines the fractional contributions of the dominant coherent process and the ideal depolarizer. This fractional contribution adjusts the depolarization of the MM which changes with scattering geometry, albedo, and surface texture.[50]
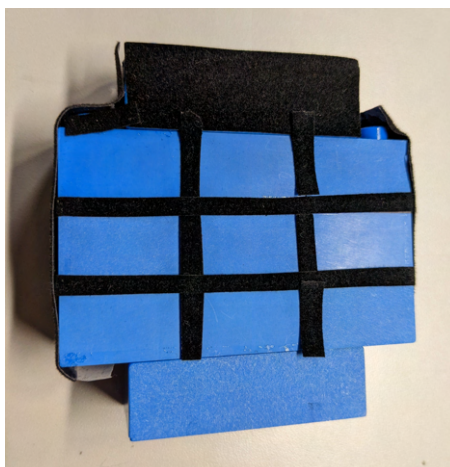
Figure 6.1: A tower of blue plastic LEGO bricks that have each been sanded with different grits of sandpaper. This represents a group of objects with similar properties and albedos for a given wavelength but with different surface textures. The roughness averages (Ra) in microns for each brick are top: 0.49, 0.56, 3.35, middle: 3.55, 2.62, 0.35, bottom: 1.68, 1.26, 6.32.

6.3 Roughened Plastic Bricks with the First-Surface Model

The samples measured in this work are a collection of blue LEGO bricks shown in Fig. 6.1. These are the same LEGOs used by Li and Kupinski and are a collection of individual objects with the same material properties and albedo but with varying texture.[55] The surface roughness of each brick was measured using a white light interferometer. The roughness averages (Ra) in microns for each brick are top: 0.49, 0.56, 3.35, middle: 3.55, 2.62, 0.35, bottom: 1.68, 1.26, 6.32. Since the bricks are blue, the different wavelengths represent different albedo cases: 662 nm illumination is low albedo and 451 nm illumination is high albedo. Umov's effect states that the amount of depolarization is expected to trend positively with albedo, so these albedo cases also represent cases with different amounts of depolarization.[103]

Figure 6.2 shows a comparison of MM images calculated using traditional Mueller polarimetry with 40 polarimetric measurements versus partial polarimetric extrapolations using 4 polarimetric measurements. Depolarization can be qualitatively observed by comparing the magnitude of M_{00} to other matrix elements: regions of the image where all matrix elements have a smaller magnitude than M_{00} have larger depolarization. Depo-

Table 6.1: 30 acquisition geometries specified on-axis where ϕ_i and ϕ_o are 0°. For each angle between the sample surface normal and source, θ_i, measurements are performed for six angles between the surface normal and the camera, θ_o. The scattering geometries across the field of view of an image will have θ_i, ϕ_i, θ_o, and ϕ_o that deviate from these on-axis values. Some acquisition geometries are omitted from analysis because exposure issues with the linear Stokes camera produced non-physical MM extrapolations.

θ_i	$\theta_{o,1}$	$\theta_{o,2}$	$\theta_{o,3}$	$\theta_{o,4}$	$\theta_{o,5}$	$\theta_{o,6}$
-10°	10°	20°	30°	40°	50°	60°
-25°	15°	25°	35°	45°	55°	65°
-40°	20°	30°	40°	50°	60°	70°
-55°	25°	35°	45°	55°	65°	75°
-70°	30°	40°	50°	60°	70°	80°

larization is expected to be stronger for the high albedo case of blue bricks under blue illumination, and this can be seen by the relatively lower magnitudes across the field of view in both the reconstruction and extrapolation. Likewise, the expectation of lower depolarization is met for the low albedo case of the blue bricks under red illumination. The trend of increased depolarization with surface roughness is also captured by the extrapolation.

Figure 6.3 shows the estimated values of $\widetilde{\xi}_0$ for the smoothest and roughest textured bricks. Larger values correspond to a larger estimated contribution of the dominant process, or equivalently lower depolarization. For both brick textures, estimates of $\widetilde{\xi}_0$ are larger in the low albedo case of 662 nm illumination than in the high albedo case of 451 nm illumination. This is in agreement with expectations from Umov's effect where depolarization trends positively with albedo. Furthermore, for both wavelengths, estimates of $\widetilde{\xi}_0$ are larger for the smooth brick and smaller for the rough brick. This trend matches the expectation of a rougher texture resulting in higher depolarization.

(a) Full reconstruction 451 nm

(b) Extrapolation 451 nm

(c) Full reconstruction 662 nm

(d) Extrapolation 662 nm
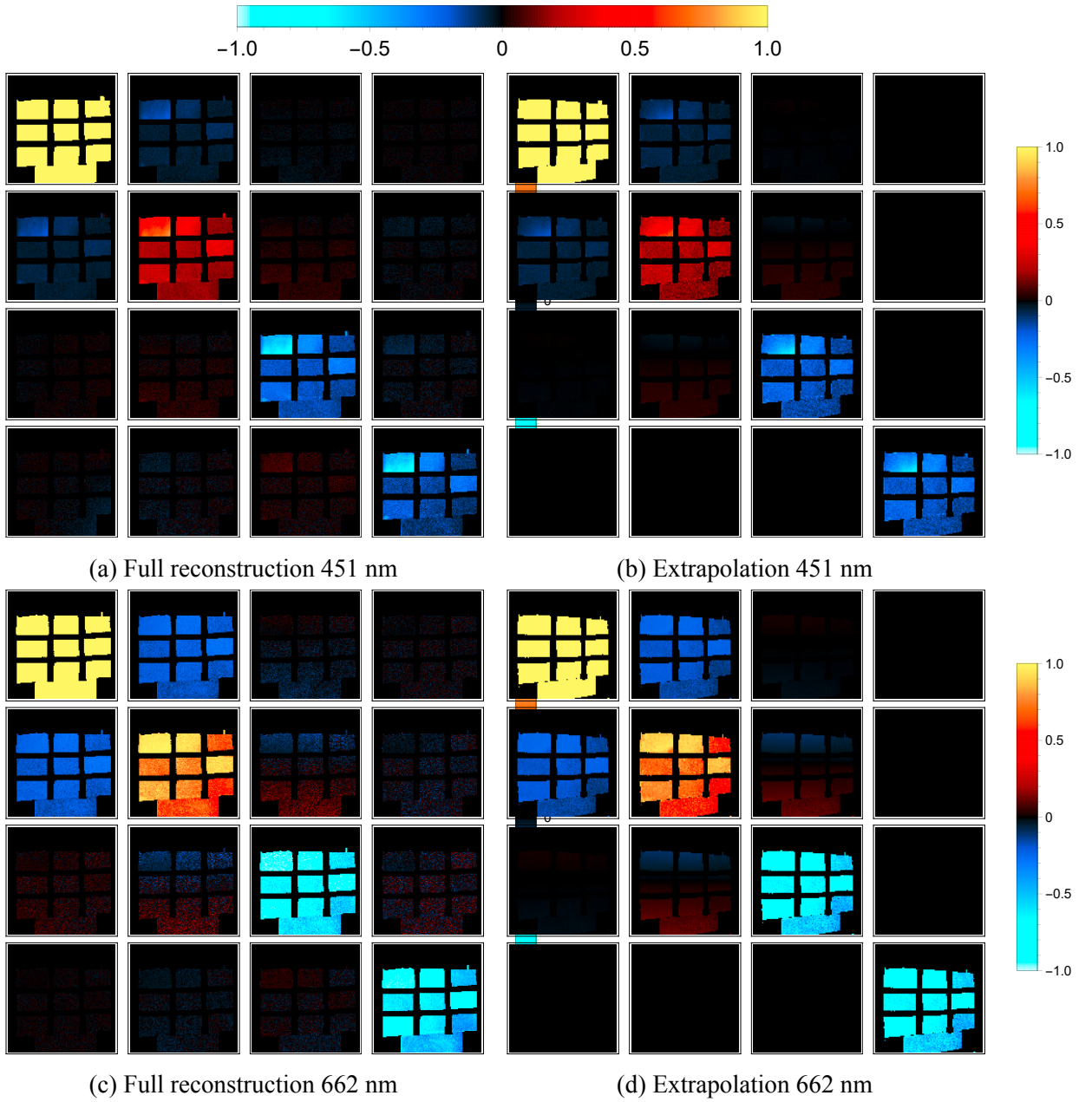
Figure 6.2: Comparison of the MM image results at 451 nm of (a) full reconstruction with 40 polarimetric measurements to (b) MM image results of partial polarimetric extrapolation and at 662 nm of (c) full reconstruction and (d) extrapolation for the geometry $\theta_i = -25°$, $\theta_o = 25°$.
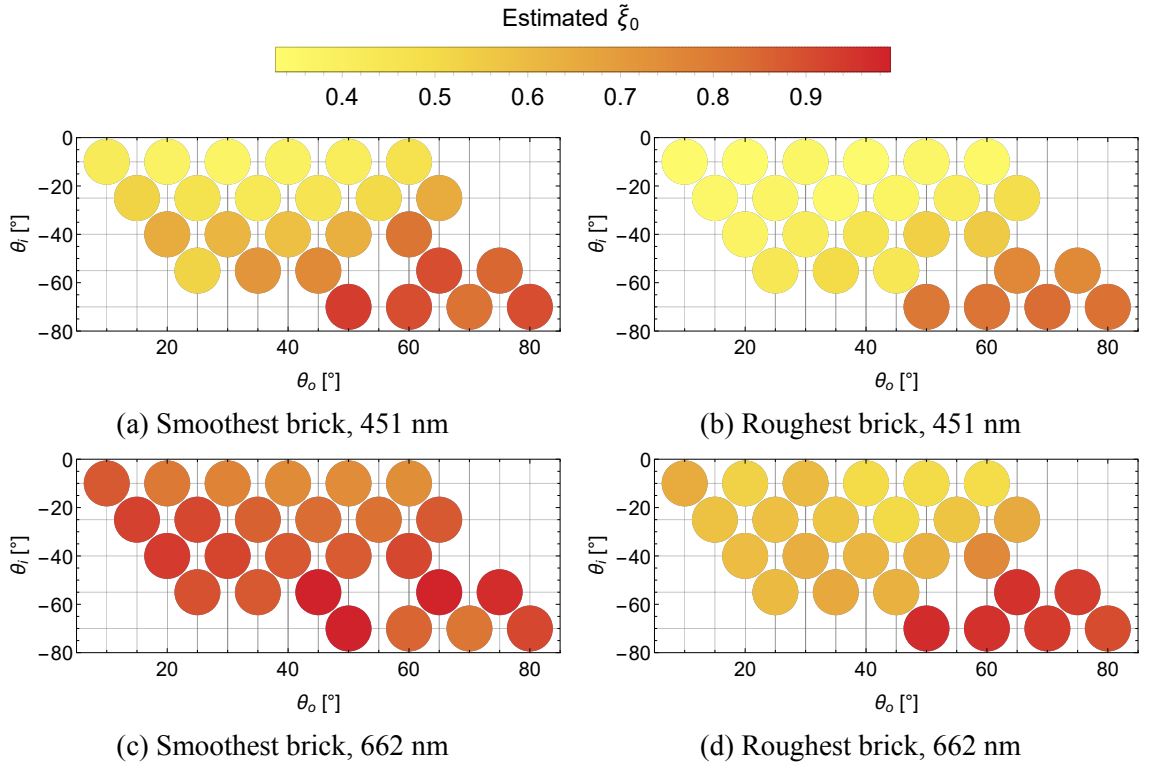
Figure 6.3: The estimate $\widetilde{\xi}_0$ calculated as in Eq. 6.5 for two different brick textures at both wavelengths. Geometries at which the dynamic range of the linear Stokes camera caused non-physical MM extrapolations are omitted.

6.3.1 Error in Dominant Eigenvalue Estimate

Figure 6.4 shows the difference between the true value of ξ_0 from the complete MM reconstruction and the estimated $\widetilde{\xi}_0$ from the linear Stokes measurements. Positive-valued differences correspond to an overestimation of the dominant non-depolarizing process or equivalently an underestimation of the amount of depolarization.

Extrapolations at 451 nm tended to overestimate $\widetilde{\xi}_0$ at more geometries than at 662 nm. 662 nm is the low-albedo case, where Umov's effect indicates that depolarization is lower, so it is possible that the method is most successful for low-depolarization cases.
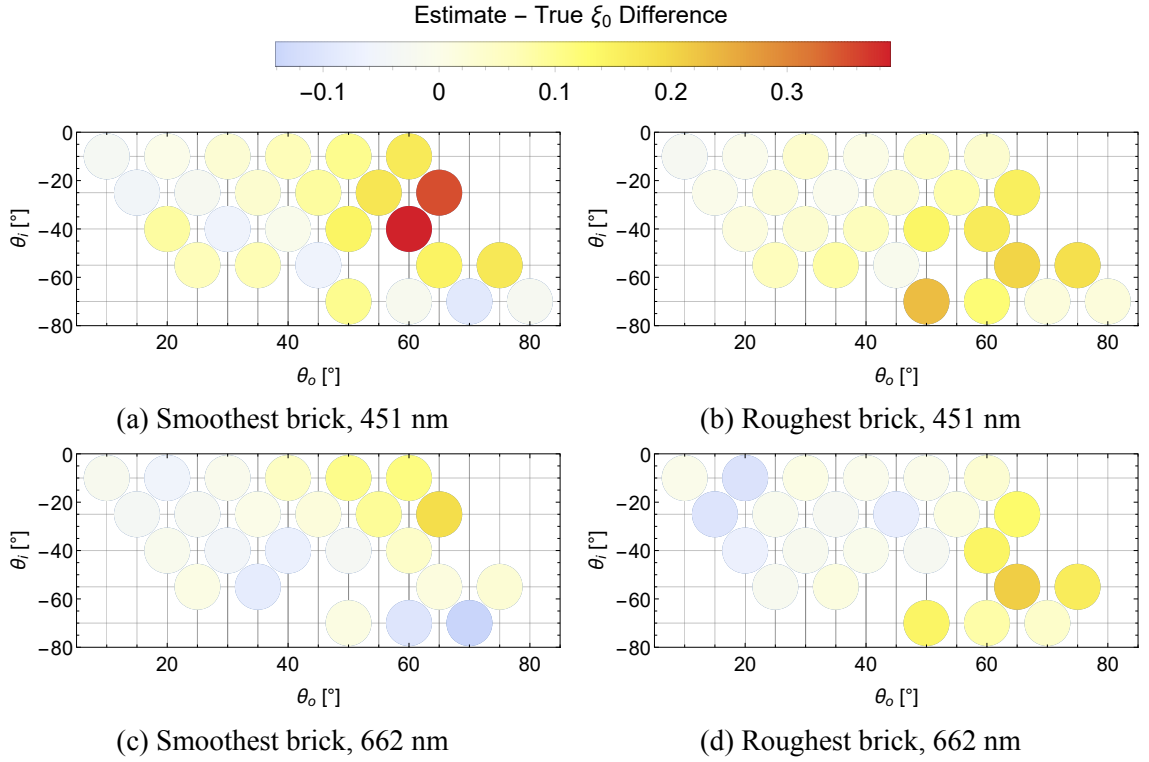
Figure 6.4: The estimate $\widetilde{\xi_0}$ calculated as in Eq. 6.5 minus the true ξ_0 versus acquisition geometry. When the difference is positive valued, the contribution of the dominant non-depolarizing term is overestimated. Geometries at which the dynamic range of the linear Stokes camera caused non-physical MM extrapolations are omitted.

6.3.2 Simulated Flux Vectors

To compare the MMs, the measurement matrix of the RGB950 $\mathbf{W}_{40}$ is applied to a 2×2 pixel average of the normalized extrapolated MM and the full reconstructed MM to simulate the flux measurements that the RGB950 would take. Additionally, the measurement noise is indicated by the standard deviation error bar on each flux measurement. The resulting flux vectors are shown in Fig. 6.5. Also shown in Fig. 6.5 is the nearest TD approximation of the reconstructed MM. This is calculated by setting the three smallest coherency eigenvalues to $\frac{1-\xi_0}{3}$. This TD approximation has the exact correct dominant process $\widehat{\mathbf{m}}_0$ and represents the best possible extrapolation based on a TD model. Flux vectors where the TD approximation and extrapolation show a similar deviation from the full reconstruction could indicate that the TD assumption is not valid. However, the movie

(a) Smoothest brick, 451 nm

(b) Roughest brick, 451 nm

(c) Smoothest brick, 662 nm

(d) Roughest brick, 662 nm
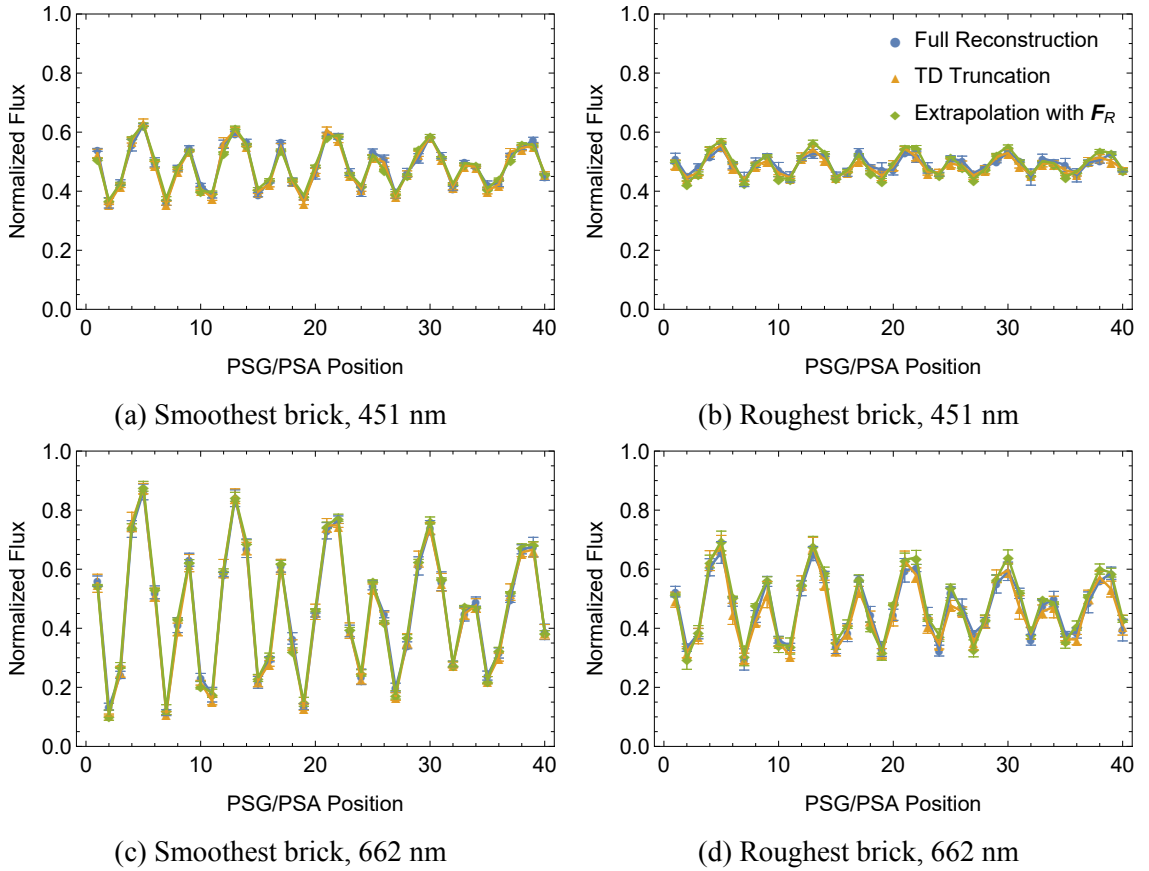
Figure 6.5: Flux vectors at 451 nm of (a) the smoothest brick and (b) the roughest brick and at 662 nm of (c) smoothest brick and (d) the roughest brick at $\theta_i = -25°$, $\theta_o = 25°$. Flux vectors are calculated by averaging the normalized MM on a 2×2 pixel ROI then applying $\mathbf{W}_{40}$ to simulate what the RGB950 would measure. The error bars are ± 1 standard deviation in the ROI. The flux vectors shown here are for the full MM reconstructions (blue), the nearest TD approximation of the reconstruction (orange), and the extrapolated MMs (green).

of flux vectors over acquisition geometry does not show consistent disagreement between the reconstruction and the TD approximation, where the extrapolation also deviates. The measurements at 662 nm (the low albedo case) exhibit larger error bars for both the smooth and rough brick as compared to measurements at 451 nm (high albedo). This matches expectations since, despite larger polarization modulation for low albedo per Umov's effect, the overall amount of light is lower.[103] The largest realizations of measurement noise occur for the rough brick at scattering geometries near those with non-physical results but

(a) Extrapolation using $\mathbf{F}^R$ (b) TD truncation of true MM
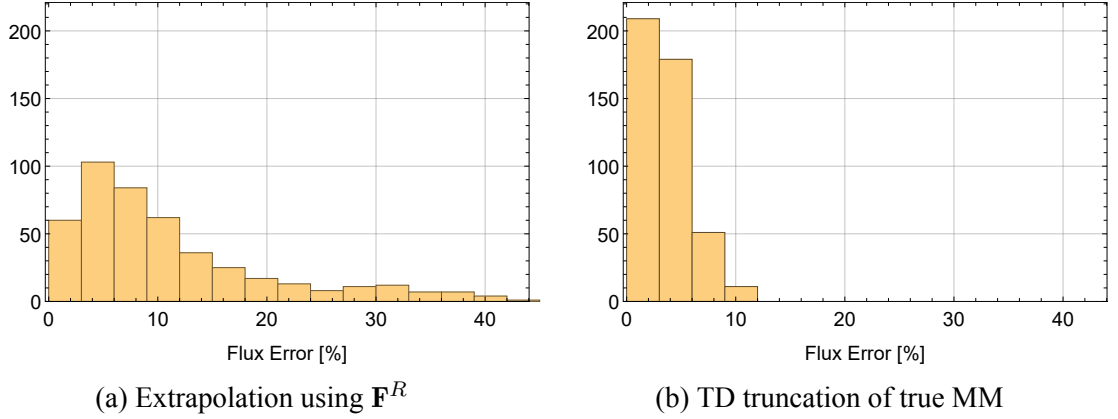
Figure 6.6: Histograms of flux error, as defined in Eq. 6.6, of (a) the extrapolated MMs based on assuming the dominant process is Fresnel reflection and (b) the nearest TD truncations of the true MMs relative to the true MMs. Each histogram contains the data over all textures, all geometries, and both wavelengths. The narrower distribution in (b) as compared to (a) indicates that the assumption of a TD eigenspectrum is not the largest source of error. The mean of (a) is 11.06% and the mode is 1.03%. The mean of (b) is 3.61% and the mode is 0.54%.

are not yet themselves non-physical. However, for all other measurements the disagreement between the extrapolations and the full reconstruction is larger than the error bars. This means that errors in the extrapolation are more likely the result of discrepancies in the assumed dominant process.

To compare MMs with a single-valued metric, the flux error ϵ is defined as

$$\epsilon = \frac{\sum_j^{40} |p_j - \widetilde{p}_j|}{\sum_j^{40} p_j}, \tag{6.6}$$

where p_j are the elements of the flux vector simulated by applying the RGB950 measurement matrix $\mathbf{W}_{40}$ to the ground truth MM (*i.e.* the full reconstruction) and $\widetilde{p}_j$ are the elements of the flux vector simulated by applying $\mathbf{W}_{40}$ to the MM being tested. This can be interpreted as adding up all the discrepancies and normalizing by the total expected flux. A flux error $\epsilon = 0$ would mean that the two MMs yield the same RGB950 measurements. This physical interpretation is the motivation for choosing the Eq. 6.6 as the figure of merit instead of a sum of squared differences between two MMs. Furthermore, small disagreements in multiple off-diagonal MM elements could yield a small squared difference in MM elements, but be an appreciable retardance difference.

Figure 6.6 shows histograms of flux errors calculated from the same flux vectors as in Fig. 6.5 but also includes the other textures. Figure 6.6a is the histogram of flux errors between the full reconstruction MMs and the MMs extrapolated from linear Stokes images using an assumed Fresnel reflection dominant process. The sources of error are measurement noise, the assumed dominant process, and the assumption of a TD eigenspectrum. The mean is 11.65% and the mode is 1.03%. Figure 6.6b is the histogram of flux errors between the full reconstruction MMs and those same MMs truncated to have a TD eigenspectrum. The process of TD truncation, explained above, preserves the exact dominant process and is not a new noise-realization, so the only source of error is the difference in eigenspectrum. The mean is 3.61% and the mode is 0.54%. The narrower distribution in Fig. 6.6b as compared to Fig. 6.6a indicates that the assumption of a TD eigenspectrum is not the largest source of error.

For both bricks and both wavelengths, Fig. 6.7 shows that the larger flux errors tend to occur for the larger incident and scattering angles. The maximum flux error is 0.42 which occurs for the rough brick under 662 nm illumination at $\theta_i = -60°$, $\theta_o = 65°$, despite the maximum error in ξ_0 occurring for the smooth brick at 451 nm at $\theta_i = -40°$, $\theta_o = 60°$.

Tab. 6.2 reports the flux error ϵ averaged over acquisition geometry for each brick and at both wavelengths. Both the overall minimum and maximum flux errors occur for 662 nm illumination on the 0.56 micron and 3.35 micron Ra bricks, respectively. Since these extrema do not correspond to the smoothest or roughest textures, it is likely that texture is not the dominant contributing factor to the error. Averaging over texture, the high-albedo case has an error of 10.50% and the low-albedo case has an error of 11.65%.

Table 6.2: The flux error ϵ, as defined in Eq. 6.6 averaged over acquisition geometry for each brick. Acquisition geometries that produced non-physical MM extrapolations due to the dynamic range of the linear Stokes camera are omitted.

Brick Ra [microns]	0.35	0.49	0.56	1.26	1.68	2.62	3.35	3.55	6.32
ϵ at 451 nm [%]	11.50	11.40	8.96	8.33	7.79	11.06	13.28	12.28	9.93
ϵ at 662 nm [%]	10.42	8.42	7.23	12.82	8.75	12.95	15.55	15.16	14.89
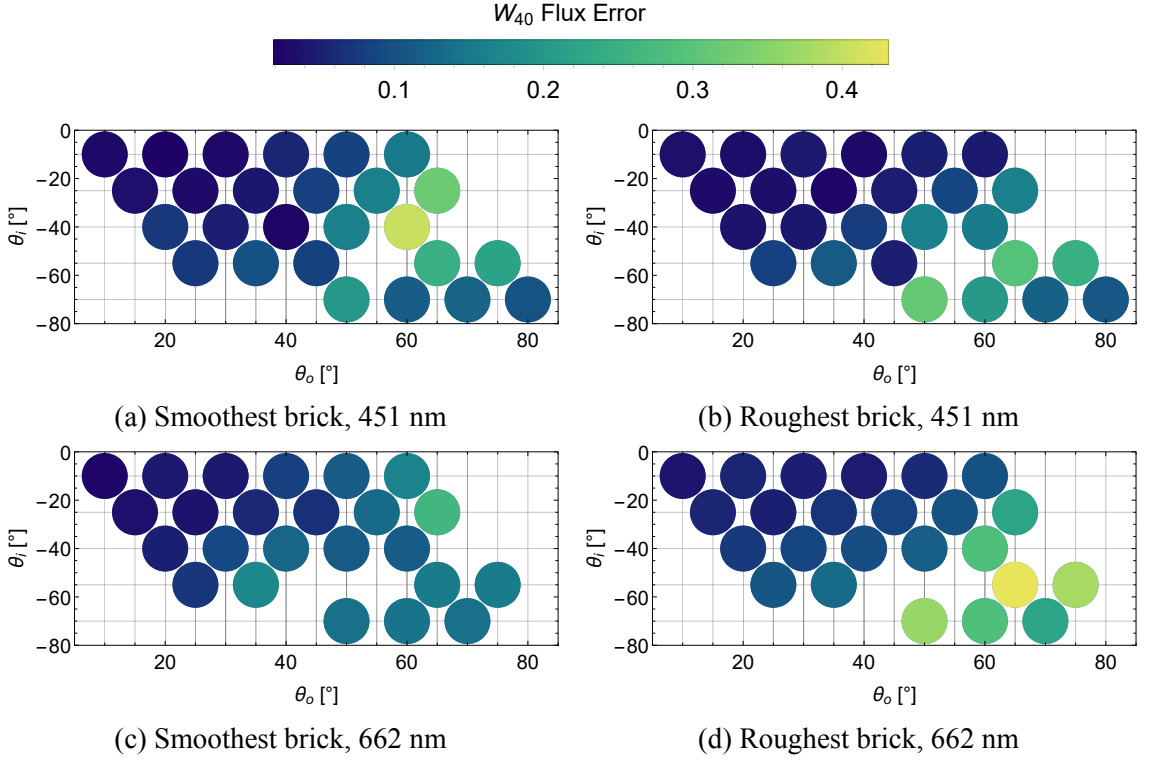
Figure 6.7: Flux vector error ϵ, as defined in Eq. 6.6, of the LEGO brick MMs extrapolated from linear Stokes images and MMs reconstructed by the RGB950 plotted versus acquisition geometry for (a,c) the smoothest brick and (b,e) the roughest brick. (a) and (b) are the high albedo case and (c) and (d) are the low albedo case. Each flux vector was calculated by averaging the normalized MM on a 2×2 pixel region then applying $\mathbf{W}_{40}$ to simulate what the RGB950 would measure. Each point corresponds to an acquisition geometry according to Tab. 6.1. Geometries at which the dynamic range of the linear Stokes camera caused non-physical MM extrapolations are omitted.

6.4 3D Printed Objects with the Mixed Model

6.4.1 Coherency Eigenspectrum

To demonstrate the appropriateness of a TD assumption for the red 3D printing material used in this work, Fig. 6.8 shows the deviation of the coherency eigenspectrum from TD of a printed Stanford bunny at two wavelengths. Since the eigenvalues are normalized to sum to unity, the difference of a given eigenvalue from $\overline{\xi}$ can be thought of as the fraction of light that is not described by a TD model. The low albedo case of 451 nm illumination

deviates from TD for as much as 9% of the light while the high albedo case of 662 nm illumination only deviates as much as 3%. For both wavelengths, the deviation from TD is larger in regions of high curvature. This could be due to increased likelihood of multiple ray bounces resulting in more complex polarized light scattering behavior. Furthermore, in regions where an object's geometry varies rapidly within a pixel's instantaneous field-of-view, errors such as the point-wise evaluation of the pBRDF described in Sect. 5.3.1 will result in greater deviate from the true polarized scattering behavior. In regions with high deviation from a TD eigenspectrum, tasks such as estimation of ξ_0 will be less accurate even when $\widehat{\mathbf{M}}_0$ is perfectly known.

6.4.2 Estimation of Dominant Eigenvalue from Stokes for a Sphere

To measure polarized behavior at many scattering geometries in fewer acquisitions, the measured object was a red 3D printed sphere of 1-inch diameter. The sphere was positioned at the center of rotation of a goniometric arm which was used to perform polarimetric measurements at fifteen angles between the camera and the light source denoted with Ω. Polarimetric measurements were performed at 662 nm and 451 nm. These two wavelengths represent high and low albedo cases, respectively, for the red sphere. Per Umov's effect, these correspond to an expectation of high depolarization (low ξ_0) and low depolarization (high ξ_0), respectively.

The RGB950 and linear Stokes camera were both used with 8mmm focal length lenses but have different detector sizes and resolutions. Additionally, the alignment for positioning the two cameras to have the same view proved challenging. A pixel-to-pixel comparison between RGB950 and Stokes camera images would therefore mean comparing polarimetric behavior at different scattering geometries. Instead, the estimated $\widetilde{\xi}_0$ from the linear Stokes camera is compared to the values from the RGB950 by tabulating a lookup table of ξ_0 values with respect to scattering geometry for each polarimeter. These LUTs are binned according , θ_h, θ_d, and ϕ_d with 91, 91, and 361 bins assigned respectively in a Cartesian representation as described in Chapter 4. The cylindrical representation had not yet been developed at the time of this work. The lookup table is then evaluated at the scattering geometries of a virtual sphere matching the linear Stokes camera measurement

−0.09   0   0.09

(a) $\xi_1 - \bar{\bar{\xi}}$ 451 nm   (b) $\xi_2 - \bar{\bar{\xi}}$ 451 nm   (c) $\xi_3 - \bar{\bar{\xi}}$ 451 nm

−0.03   0   0.03

(d) $\xi_1 - \bar{\bar{\xi}}$ 662 nm   (e) $\xi_2 - \bar{\bar{\xi}}$ 662 nm   (f) $\xi_3 - \bar{\bar{\xi}}$ 662 nm
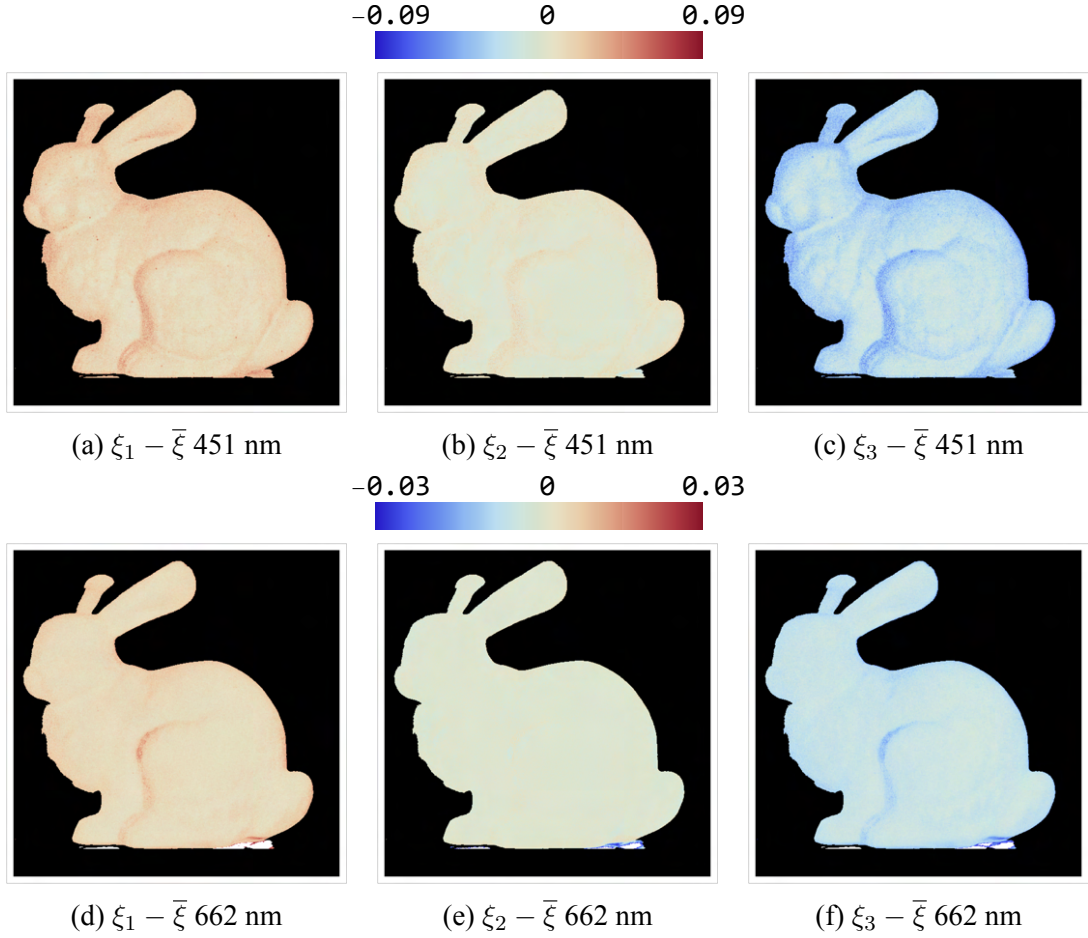
Figure 6.8: Deviation of each of the smaller three coherency eigenvalues ξ_1, ξ_2, and ξ_3 from $\bar{\bar{\xi}} = (1 - \xi_0)/3$ for a red 3D printed bunny. Values shown in (a-c) are at 451 nm and values shown in (b-f) are at 662 nm. Each row shares a colorbar. When ξ_1, ξ_2, and ξ_3 are all equal to $\bar{\bar{\xi}}$, then the coherency eigenspectrum is TD and the depolarizing MM can be exactly described as a sum of a dominant MJM and an ideal depolarizer (see Fig. 2.2). The eigenspectrum for the red 3D printed bunny under 451 nm illumination (low albedo, low depolarization per Umov's effect) has larger deviation from TD than 662 nm (high albedo, high depolarization). This trend with wavelength suggests that even if the dominant MJM model $\widehat{\mathbf{m}}_0$ is accurate, the error in assuming the MM fits Eq. 2.18 would be greater at 451 nm than 662 nm. In particular, regions of high curvature deviate more from TD as shown on the left side of the bunny's hind leg.

to compare the true and estimated ξ_0 at identical points.

The estimations of $\widetilde{\xi_0}$ from the linear Stokes camera over the sphere at $\Omega = 35°$ are shown in Fig. 6.9a and d, the ground truth values measured in the RGB950 are shown

(a) True ξ_0 451 nm   (b) Estimated $\widetilde{\xi}_0$ 451 nm   (c) ξ_0 deviation 451 nm

(d) True ξ_0 662 nm   (e) Estimated $\widetilde{\xi}_0$ 662 nm   (f) ξ_0 deviation 662 nm
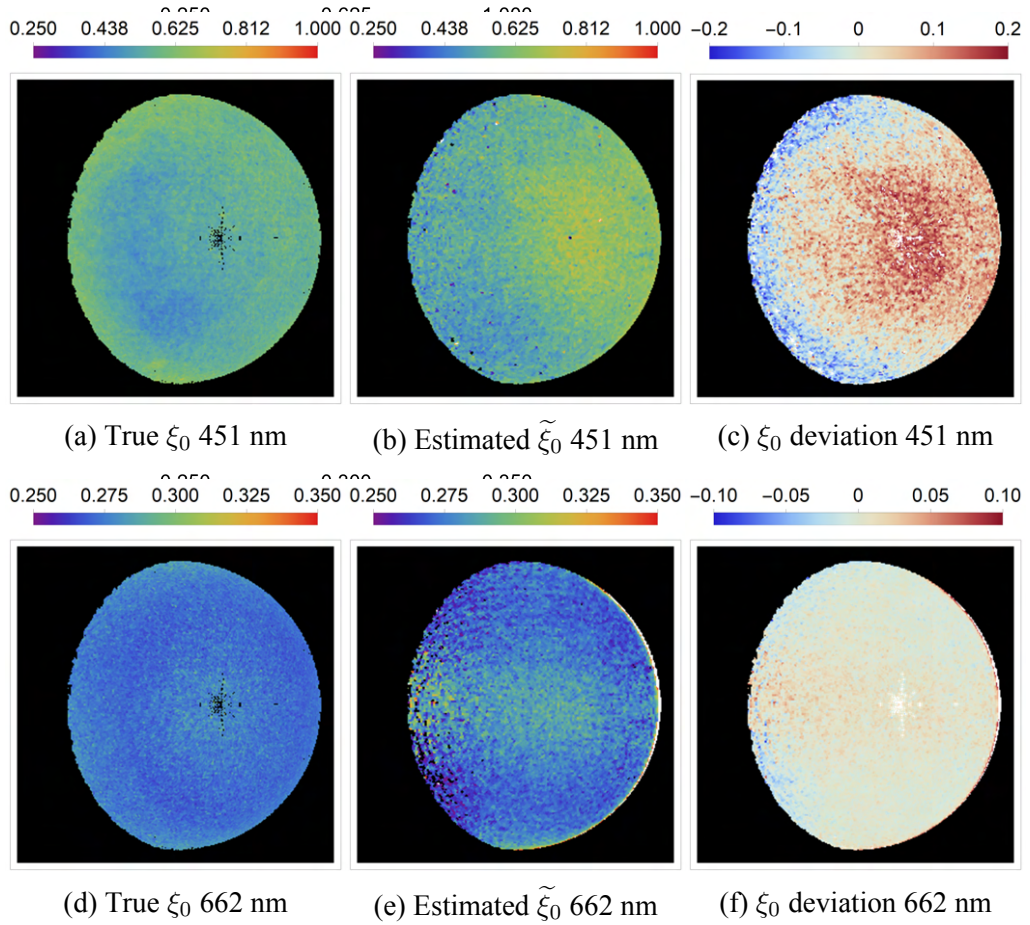
Figure 6.9: Results for the estimation of $\widetilde{\xi}_0$ for angle between the camera and light source $\Omega = 35°$. The ground truth values from the DRR polarimeter in (a) and the estimated values from the linear Stokes camera in (b) at 451 nm are compared in (c) by taking their difference. The ground truth values from the DRR polarimeter in (d) and the estimated values from the linear Stokes camera in (e) at 662 nm are compared in (f) by taking their difference. 662 nm is high albedo for the red sphere, so depolarization is high and ξ_0 is low. 451 nm is low albedo, so ξ_0 is larger. In (c) and (f), positive values indicate an overestimation of the contribution of $\widehat{\mathbf{m}}_0$ while negative values indicate an overestimation of the contribution of $\mathbf{m}_{ID}$. Because the eigenvalues are normalized to sum to unity, the errors shown in (c) and (f) can be thought of as related to the fraction of the light that is attributed to the wrong MM component.

in Fig. 6.9b and e, and the difference between estimate and ground truth are shown in Fig. 6.9c and f. The white region in the center consists of specific Rusinkiewicz coordinates that the instruments do not have in common. 662 nm is high albedo for the red
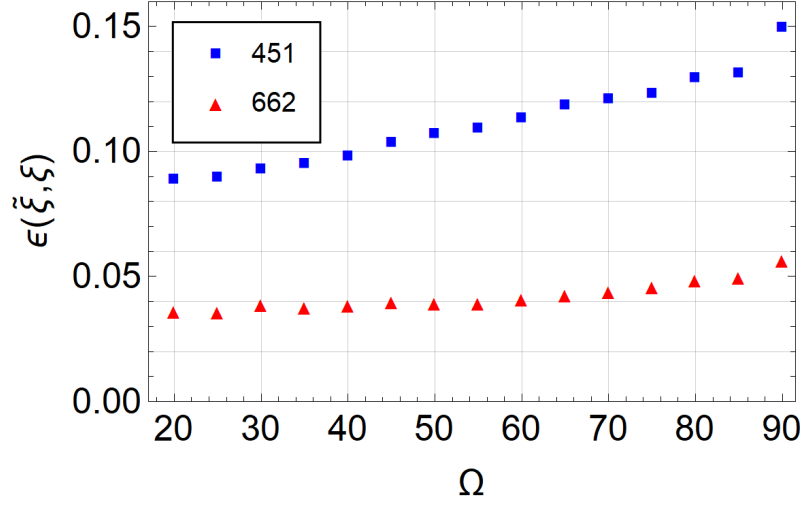
Figure 6.10: RMSD in $\widetilde{\xi}_0$ estimate from Stokes imaging as compared to ground truth from DRR MM imaging according to Eq. 6.7 at 451 nm (blue squares) and 662 nm (red triangles) at the fifteen acquisition geometries Ω. RMSD values at 451 nm, the low albedo case, are strictly greater than those for 662 nm. This is potentially explained by the material being less depolarizing according to Umov's effect than at 662 nm and therefore more sensitive to disagreement between the ground truth and modeled $\widehat{\mathbf{m}}_0$. Additionally, the eigenspectrum at 451 nm is further from TD than for 662 nm, so a TD model may be less appropriate. The lower throughput due to the low albedo could exacerbate the effects of noise and degrade the estimation due to the smaller dynamic range of the linear Stokes camera.

sphere, so the expectation according to Umov's effect is that depolarization is high and ξ_0 is low. Conversely, 451 nm is low albedo so ξ_0 is expected to be larger. Both of these trends are observed in the ground truth measurements as well as in the estimations. In Fig. 6.9c and f, positive values indicate an overestimation of the contribution of $\widehat{\mathbf{m}}_0$ while negative values indicate an overestimation of the contribution of $\mathbf{m}_{ID}$. Because the eigenvalues are normalized to sum to unity, the errors shown in Fig. 6.9c and f can be thought of as related to the fraction of the light that is attributed to the wrong MM component.

The error averaged over the image of the sphere is summarized quantitatively by the RMSD

$$\epsilon(\widetilde{\xi}_0, \xi_0) = \sqrt{\frac{1}{K}\sum_{k=1}^{K}||\widetilde{\xi}_{0,k} - \xi_{0,k}||^2}, \tag{6.7}$$

where K is the total number pixels, and k is the pixel index. Figure 6.10 shows the trend of

$\epsilon(\widetilde{\xi}_0, \xi_0)$ as a function of the angle between the camera and light source Ω. The error at 451 nm is larger than at 662 nm for every Ω. According to Umov's effect, the depolarization at 451 nm for a red object should be lower, suggesting that the estimation is more sensitive to disagreement between the ground truth and model $\widehat{\mathbf{M}}_0$. Additionally, the relatively lower overall reflectance at 451 nm also makes the linear Stokes camera measurements more susceptible to noise.

Despite the MJM model diattenuation properties matching the measurement better at 451 nm than at 662 nm, using the MJM models to estimate ξ_0 resulted in RMSD values (see Fig. 6.10) averaged over acquisition geometry of 11.11% at 451 nm and 4.24% at 662 nm. This performance difference can be understood by noting that the depolarization magnitude at 662 nm is higher and therefore the estimation is less sensitive to MJM model accuracy.

6.4.3 Mueller Extrapolation from Stokes for a Stanford Bunny

To extend the demonstration of the efficient TD-MM model to non-spherical objects, the MM image of a Stanford bunny was extrapolated from linear Stokes camera measurements. This Stanford bunny was printed from the same material as the sphere in Chapter 5, so the same pBRDF models were used.

Linear Stokes measurements are performed using the COTS camera and one polarized illumination state from the RGB950 light source as in Sect. 6.4.2. The $\widehat{\mathbf{M}}_0$ models are evaluated at the Rusinkiewicz angles calculated from the .stl file used to 3D print the Stanford bunny. The $\widehat{\mathbf{M}}_0$ model and Stokes data are used to estimate $\widetilde{\xi}_0$ following Sect. 6.2. MM extrapolation is performed by plugging the estimated $\widetilde{\xi}_0$ back into Eq. 2.18.

Figure 6.11 shows a visual comparison of the Stanford bunny between various polarizers using the DRR measurements (left) and extrapolated MM image from linear Stokes data (right). Each pair of images is on the same color scale. Crossed linear, aligned linear, and crossed circular measurements are simulated. The MM images are normalized, so variation in the throughput of the second polarizer is due to the diattenuation, depolarization, and geometric transformation of the incident polarizer. The overall appearance between the results from DRR measurement and Stokes extrapolation are in agreement,

particularly with respect to wavelength. At 451 nm, shown in Fig. 6.11a-c, the smaller amount of depolarization expected for a low albedo material appears as greater polarimetric modulation as compared to 662 nm, shown in Fig. 6.11d-f. The overall geometry trends match as well shown by the regions of the bunny which appear brighter or darker are in the results from DRR measurement correspond to brighter or darker regions in the results extrapolation from Stokes data. Notably, the region with the most significant difference is the left side of the bunny's leg. This is the region where the TD assumption is weakest due to a higher angle of scattering, as shown in Fig. 6.8. Additionally, this region of high curvature is where misregistration between the modeled geometry shown in Fig. 5.2b, d, and f and the geometry measured with the Stokes camera would cause large deviation in the modeled and measured $\widehat{\mathbf{M}}_0$, reducing the quality of the extrapolation. There is unavoidable disagreement between the DRR simulations and the linear Stokes images due to even slight differences in viewing geometry, resolution, and camera properties of the two polarimeters. An example of such disagreement due to different camera systems can clearly be seen on the left ear which has a significantly different shadow between DRR and Stokes results.

6.5   Conclusions and Discussion

For materials described by the simple triple-degenerate polarized light scattering model, this work proposes a new and simplified way to measure the Mueller matrix. While typical Mueller polarimetry requires 16 or more polarimetric measurements to reconstruct a MM, the TD MM model allows for extrapolation from as few as 2 measurements when the dominant process is known *a priori*. Existing methods for extrapolating full MMs from partial polarimetry require non-depolarizing MMs[74,95] or, at most, a rank-two coherency matrix.[1] This work is the only method known to the authors for extrapolating full-rank depolarizing MMs. Additionally, this method is compatible with existing DoFP polarimeter technology and therefore can be made into a snapshot polarimeter.

   To demonstrate the method with respect to surface texture, extrapolations at different geometries of LEGO bricks with varying roughness are performed with a commer-

cial linear Stokes camera and compared to the full MM polarimeter reconstructions. The depolarization, which varies with surface roughness, is apparent even on visual inspection of the diagonal elements of the extrapolated MMs. Over varying texture, geometry, and albedo, the partial polarimetric extrapolations achieve flux error mean and mode of 11.06% and 1.03%, respectively, despite a $10\times$ reduction in the number of polarimetric measurements.

To demonstrate the generalization of the TD-MM model to more complicated geometry, MM images of a 3D printed Stanford bunny were extrapolated from linear Stokes images. To compare extrapolated MM images to ground truth from DRR polarimetry, Fig. 6.11 shows simulated measurements of the bunny between various polarizers. Overall agreement is good, with regions of high and low transmitted intensity in the extrapolated results corresponding to those of the DRR results. The largest deviations occur on the left side of the hind leg where Fig. 6.8 shows the TD eigenspectrum assumption is weakest as well as being the region where registration between the geometry modeled (shown in Fig. 5.2 (b,d,f)) and the actual measured geometry is most sensitive.

The quantitative results for the sphere and the visual assessment performed on the Stanford bunny highlight an important point: the accuracy of a polarimetric model does not need to exceed the accuracy of the polarimeter in use. For example, the polarimetric accuracy of a model required to approach photorealism in a polarization-aware physics-based rendering is lower than the accuracy required in silicon wafer metrology. In the former application, a COTS Stokes polarimeter might be used to characterize a material based on an efficient, reduced parameterization with sufficient accuracy. Facilitating the characterization of many materials according to a simple model in a reduced length of time may present a significant benefit over the cost of more rigorous characterization.

(a) Crossed linear polarizers 451 nm

(b) Aligned linear polarizers 451 nm

(c) Crossed circular polarizers 451 nm

(d) Crossed linear polarizers 662 nm

(e) Aligned linear polarizers 662 nm

(f) Crossed circular polarizers 662 nm
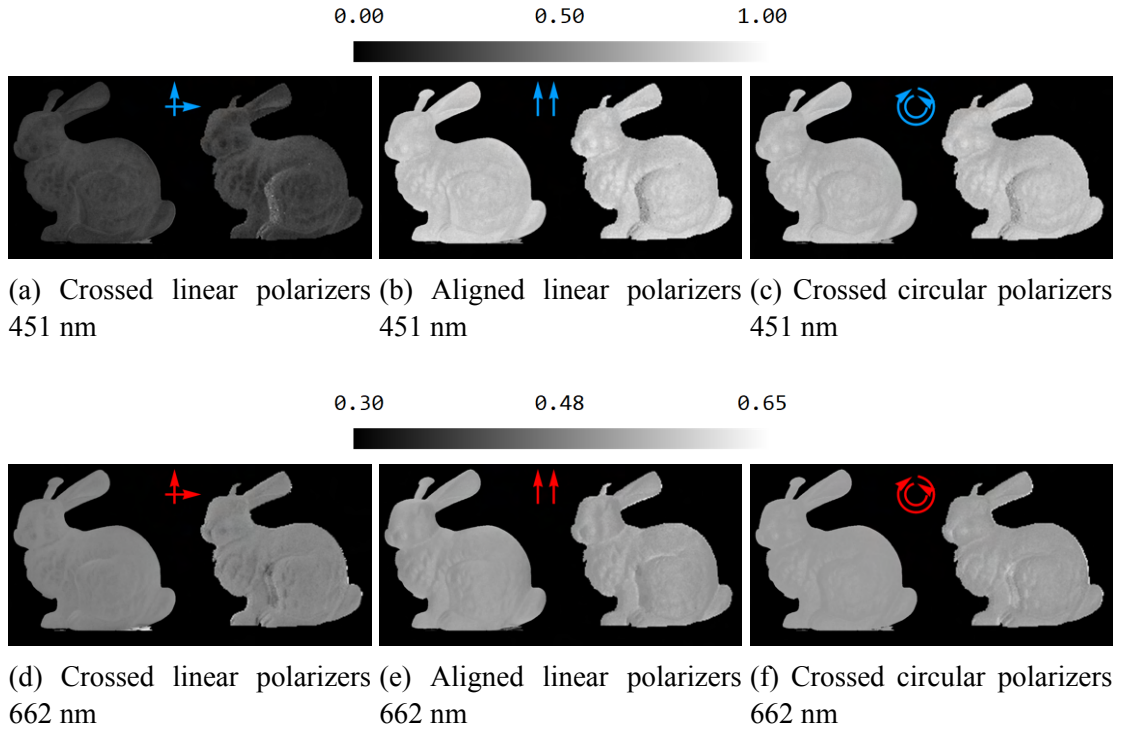
Figure 6.11: Each image pair in (a-f) is arranged so that the simulated measurements are on the left the normalized MM image of the Stanford bunny from the DRR polarimeter and (right) the normalized extrapolated MM image from linear Stokes data at 451 nm. In (a) vertically polarized illumination and a horizontal analyzer, in (b) vertically polarized illumination and a vertical polarizer, and (c) between left circular polarization illumination and a right circular polarizer denoted between each image pair. In (d-f) the same experiments is repeated at 662 nm. The MM images were normalized, so variation in the intensity transmitted through the second polarizer is due to diattenuation, depolarization, and geometric transformation of the illumination polarization. If the estimate of ξ_0 were too close to 0.25 (*i.e.* extrapolating to the ideal depolarizer), then there would be no variation and all three polarizer conditions would look flat. Overall, there is good visual agreement, with regions of high and low intensity in the DRR results tending to correspond to high and low intensity in the Stokes camera extrapolated results. It is interesting to note that, despite the MJM models having only residual circular polarization properties from the complex refractive indices, the crossed circular polarizer images show some agreement. This is because of the variation in the depolarization due to the ξ_0 estimate. There is inherent disagreement between the measurement simulated from DRR data and from the linear Stokes data due to the slightly different viewing geometry, resolution, and camera properties between the two polarimeters. Qualitatively, the agreement between DRR and Stokes results is lowest on the side of the leg. This is the region where the TD assumption is weakest, as shown in Fig. 6.8. Additionally, this region of high curvature is where misregistration between the modeled geometry shown in Fig. 5.2b, d, and f and the geometry measured with the Stokes camera would cause large deviation in the modeled and measured $\widehat{\mathbf{m}}_0$, reducing the quality of the extrapolation.

CHAPTER 7

Conclusion

Mueller characterization provides a complete description of how polarization is transformed upon a linear light-matter interaction. However, full Mueller polarimeters are generally complex and may require trade-offs in spatial or temporal resolution which are not ideal for certain applications. In these cases, partial polarimeters can be useful tools to capture application-relevant polarization information. Effective partial polarimetry is enabled by leveraging *a priori* knowledge about the subset of MMs which could be measured in a given application. This dissertation has discussed techniques for using that data for specific partial polarimetric measurements as well as a method for efficiently acquiring and storing MM data. As polarimetric sensing technologies become more mature and widely accessible, there will be an abundance of new potential applications for polarization imaging. Full MM polarimetry may be required to realize some applications, others may only require partial polarimetric information.

For example, some of the partial polarimetric experiments presented in this dissertation made use of a COTS linear Stokes camera. These cameras have only become widely available in recent years, and they have already found use in fields such as biomedical imaging and computer vision. More unique polarimetric information could be acquired without any increase in data acquisition time by using a full Stokes polarimeter. Such technologies are currently in development and will certainly enable new partial polarimetric applications.[77,83,98,99] These technologies would be particularly useful for partial polarimetric experiments involving targets with birefringence such as human corneas or metallic objects. These targets can potentially have a significant and useful circular polarization signal which strictly linear polarization measurements are insensitive to. However, circularly polarized measurements likely would not have improved the depolarization magnitude estimates of the rough LEGO bricks. An assessment of which partial polarimetric technologies and strategies are most useful for a particular application depend on an un-

derstanding of the polarization phenomena at play.

The contributions in this dissertation provide a framework for acquiring MM characterizations and for performing several partial polarimetric experiments based on insights from such characterizations. It is the author's hope that the polarization sensing technologies which make polarimetry broadly accessible will continue to develop in tandem with MM-informed partial polarimetric design. The remainder of this conclusion chapter summarizes the findings of this dissertation.

In Chapter 3, the human eye is used as a target with spatially-varying birefringence to demonstrate the optimization of a polarimeter which performs only one polarimetric measurement. The cornea in the eye is known to consist of anisotropic structures called collagen fibrils. The orientation of these fibrils changes over the spatial extent of the cornea, resulting in birefringence which varies in magnitude and orientation. Eyes are subject to random, unconscious movements which makes time-modulated Mueller polarimetry poorly suited for efficient measurement. In this work, an initial MM image is performed over the course of 15 seconds. From this MM image, two regions are selected based on their retardance orientation to maximize their contrast. A geometric construction is then performed on the to determine the illumination and analyzer polarization states which produce a polarimetric image with maximum contrast between the two regions. Three of these pairs are selected based on what measurements can be performed in the RGB950 polarimeter and are shown to capture the desired polarimetric information with snapshot acquisition. The specific application of the optimization method for corneal birefringence may find use in eye tracking, but the generality of the optimization means it may also be used for any spatially-varying birefringent targets.

In Chapter 4, a original representation for empirically acquired isotropic pBRDFs is discussed. The dependence of an isotropic pBRDF on scattering geometry is typically parameterized with three Rusinkiewicz angles. When tabulating measured data into an empirical pBRDF, these angles are interpreted as forming a 3D Cartesian grid, where one MM is associated with each point on the grid. By interpreting the three angles as cylindrical coordinates, the tabulation is made more compact and more convex. Compactness is increased by excluding non-reflection geometries and redundant geometries. Convexity is

desirable for ease of interpolation. An empirical pBRDF is acquired by taking MM images at some sequence of goniometer positions. A given set of goniometer positions generally does not capture MM data for every discrete triplet of Rusinkiewicz angles. The percentage of triplets with at least one MM data point is used as a figure of merit for comparing goniometer sequences. An efficient goniometer sequence is determined and executed for a given set of object and camera parameters. Efficient acquisition and representation of pBRDFs has implications for fields such as computer vision. More material characterizations can be obtained and stored with the same amount of resources, which increases the diversity of objects that can be used in a rendering.

In Chapter 5, pBRDF models for two different materials are discussed. The first model is for first-surface reflection based on microfacet theory. The second model is a original model introduced in this work which combines first-surface and diffuse reflection in a MJM model in order to decouple depolarization. The mixed model combines first-surface and diffuse reflection as a function of geometry based on four material constants. The model is compared to DRR polarimeter measurements in terms of diattenuation orientation and magnitude.

In Chapter 6, models for the dominant MJMs of two different objects are used to estimate depolarization magnitude from partial polarimetry. Using a TD assumption for the depolarization structure of the MM image, a linear estimator is created which can recover the depolarization magnitude from as few as two polarimetric measurements. This depolarization magnitude parameter and the dominant MJM model can then be combined to extrapolate the full-rank depolarizing MM. This is demonstrated using a commercial linear Stokes camera with a single polarized illumination state. The depolarization parameter is estimated for plastic LEGO bricks with variable surface roughness using a purely first-surface Fresnel reflection model. The original reflection model which combines first-surface reflection and diffuse reflection from Chapter 5 is used to estimate the depolarization parameter from a 3D printed red sphere and extrapolate the MM image for the Stanford bunny.

APPENDIX A

Calculation of Scattering Geometry and Transverse Plane Bases

Many of the Chapters in this dissertation relied on the calculation of scattering geometry and related quantities at each pixel within an image. The geometric derivations of these equations are not a novel contribution of this dissertation, but are collected here so that others may use this as a resource when performing similar or related work. Included in this Appendix are equations to define the observation vectors for a given a goniometric measurement configuration, equations to find the points where these vectors intersect objects of various shapes and the surface normals at those points, and equations for determining the transverse plane bases for polarization states based on the measurement and scattering geometry.

A.1 Observation, Illumination, and Normal Vectors

Except in the special case of a telecentric camera lens, the observation vectors vary in direction over the image plane. For each pixel indexed (u, v), the corresponding observation vector is given

$$\boldsymbol{\omega}_o(u, v) = \left[\left(-u + \frac{N_u}{2} \right) \mu, \;\; \left(-v + \frac{N_v}{2} \right) \mu, \;\; f_{eff} \right]^\mathsf{T}, \tag{A.1}$$

where N_u and N_v are the number of pixels in the u and v dimensions respectively, μ is the pixel pitch, and f_{eff} is the effective focal length of the camera in the same units as μ. Equation A.1 is then normalized to be a unit vector $\widehat{\boldsymbol{\omega}}_o$. The set of observation vectors for a given camera is invariant to the shape of the object, so $\widehat{\boldsymbol{\omega}}_o$ is used as the starting point for other calculations. The point where the observation ray intersects the object is calculated

$$\mathbf{r}_{obj} = \mathbf{r}_{cam} - l\widehat{\boldsymbol{\omega}}_o, \tag{A.2}$$

where l is the depth along the observation vector from $\mathbf{r}_{cam}$, the position of the camera entrance pupil. It is assumed that $\mathbf{r}_{cam}$ is known. The illumination vector is then found

$$\widehat{\boldsymbol{\omega}}_i = \frac{\mathbf{r}_{src} - \mathbf{r}_{obj}}{\|\mathbf{r}_{src} - \mathbf{r}_{obj}\|}, \tag{A.3}$$

where $\mathbf{r}_{src}$ is the position of the light source which is also assumed to be known. The following subsections provide the equations needed to calculate the depth l along the observation vector to the point of intersecting with the object as well as the equations for the surface normals $\widehat{\mathbf{n}}$ for different shapes.

A.1.1   Sphere

For a spherical object centered at the origin, a dummy variable Δ is calculated

$$\Delta = \left(-\widehat{\boldsymbol{\omega}}_o \cdot \mathbf{r}_{cam}\right)^2 - \left(\mathbf{r}_{cam} \cdot \mathbf{r}_{cam} - \rho^2\right), \tag{A.4}$$

where ρ is the radius of the sphere. When Δ is non-negative, the ray intersects the sphere. It is assumed that the ray hits the first surface of the sphere. The distance l from the camera to the sphere is given by

$$l = \widehat{\boldsymbol{\omega}}_o \cdot \mathbf{r}_{cam} - \sqrt{\Delta}. \tag{A.5}$$

The point of intersection is found by plugging l into Eq. A.2. The surface normal of the sphere is simply the vector of the intersection point normalized to a unit vector as in

$$\widehat{\mathbf{n}} = \frac{\mathbf{r}_{obj}}{\|\mathbf{r}_{obj}\|}. \tag{A.6}$$

A.1.2   Plane

For a plane, the object must be specified in terms of its surface normal, so $\widehat{\mathbf{n}}$ is assumed to be known. The distance from the camera to the planar surface centered at the origin is

$$l = \frac{\mathbf{r}_{cam} \cdot \widehat{\mathbf{n}}}{\widehat{\boldsymbol{\omega}}_o \cdot \widehat{\mathbf{n}}}. \tag{A.7}$$

The point of intersection is found by plugging l into Eq. A.2.

A.1.3 Cylinder

For a cylindrical object centered at the origin of length L_{cyl} and axis oriented at $\widehat{\mathbf{a}}_{cyl}$, a dummy variable Δ is calculated

$$\Delta = (-\widehat{\boldsymbol{\omega}}_o \times \widehat{\mathbf{a}}_{cyl}) \cdot (-\widehat{\boldsymbol{\omega}}_o \times \widehat{\mathbf{a}}_{cyl})\rho^2 - (\widehat{\mathbf{a}}_{cyl} \cdot \widehat{\mathbf{a}}_{cyl})(-\mathbf{r}_{cam} \cdot (-\widehat{\boldsymbol{\omega}}_o \times \widehat{\mathbf{a}}_{cyl})), \qquad \text{(A.8)}$$

where ρ is the radius of the cylinder. When Δ is non-negative, the ray intersects the cylinder. It is assumed that the ray hits the first surface of the cylinder. The distance l from the camera to the cylinder is given by

$$l = \frac{(-\widehat{\boldsymbol{\omega}}_o \times \widehat{\mathbf{a}}_{cyl}) \cdot (-\mathbf{r}_{cam} \times \widehat{\mathbf{a}}_{cyl}) - \sqrt{\Delta}}{(-\widehat{\boldsymbol{\omega}}_o \times \widehat{\mathbf{a}}_{cyl}) \cdot (-\widehat{\boldsymbol{\omega}}_o \times \widehat{\mathbf{a}}_{cyl})}. \qquad \text{(A.9)}$$

Equation A.2 is used to find the intersection point. If $-L_{cyl}/2 \leq \mathbf{r}_{obj} \cdot \widehat{\mathbf{a}}_{cyl} \leq L_{cyl}/2$, then the ray intersects the curved surface of the cylinder. If the ray intersects the curved surface, then the surface normal is calculated

$$\widehat{\mathbf{n}} = \frac{\mathbf{r}_{obj} - \widehat{\mathbf{a}}_{cyl}(\widehat{\mathbf{a}}_{cyl} \cdot \mathbf{r}_{obj})}{\|\mathbf{r}_{obj} - \widehat{\mathbf{a}}_{cyl}(\widehat{\mathbf{a}}_{cyl} \cdot \mathbf{r}_{obj})\|}. \qquad \text{(A.10)}$$

A.2 Rusinkiewicz Coordinate System

Once $\widehat{\boldsymbol{\omega}}_i$, $\widehat{\boldsymbol{\omega}}_o$, and $\widehat{\mathbf{n}}$ are found per the previous section, the Rusinkiewiciz angles, see Fig. 4.1, can be calculated. The halfway vector, $\widehat{\mathbf{h}}$, is the bisector of $\widehat{\boldsymbol{\omega}}_i$ and $\widehat{\boldsymbol{\omega}}_o$

$$\widehat{\mathbf{h}} = \frac{\widehat{\boldsymbol{\omega}}_o + \widehat{\boldsymbol{\omega}}_i}{\|\widehat{\boldsymbol{\omega}}_o + \widehat{\boldsymbol{\omega}}_i\|}. \qquad \text{(A.11)}$$

Different conventions exist for the direction of $\widehat{\boldsymbol{\omega}}_i$ (*i.e.*, pointing toward the source or in the direction of photon-travel), however the equations provided here are consistent. The halfway angle and difference angle, θ_h and θ_d, respectively, are simply calculated

$$\theta_h = \arccos(\widehat{\mathbf{h}} \cdot \widehat{\mathbf{n}}) \qquad \text{(A.12)}$$

and

$$\theta_d = \arccos(\widehat{\mathbf{h}} \cdot \widehat{\boldsymbol{\omega}}_0). \qquad \text{(A.13)}$$

The angle between the plane spanned by $\widehat{\mathbf{n}}$ and $\widehat{\mathbf{h}}$ and the plane spanned by $\widehat{\boldsymbol{\omega}}_o$ and $\widehat{\mathbf{h}}$ is given by

$$\phi_d = \arccos\left[\left(\widehat{\mathbf{h}} \times \widehat{\mathbf{n}}\right) \cdot \left(\widehat{\mathbf{h}} \times \widehat{\boldsymbol{\omega}}_o\right)\right] \operatorname{sgn}\left[\left(\left(\widehat{\mathbf{h}} \times \widehat{\mathbf{n}}\right) \times \left(\widehat{\mathbf{h}} \times \widehat{\boldsymbol{\omega}}_o\right)\right) \cdot \widehat{\mathbf{h}}\right], \qquad \text{(A.14)}$$

where the signum function is used to give ϕ_d the correct handedness.

A.3 Transverse Plane Bases

In this work, there are three transverse plane bases which are used to define the orientation of polarization states: the polarimeter basis, the local basis, and the microfacet basis. These bases determine what polarization state in 3D is meant by "horizontal" and "vertical" polarization. Measured MMs and Stokes vectors are in a basis which is determined by the PSG and PSA which produced them. Tabulated and analytic pBRDFs need to be in the local basis so that the data can be generalized to other geometries and measurement configurations. The microfacet basis is used to define directions for s- and p-polarization when evaluating the Fresnel reflection coefficients from Eq. 2.4

The change of basis of a MM is equivalent to applying rotation matrices of the form

$$\mathbf{R}(\alpha) = \begin{bmatrix} 1 & 0 & 0 & 0 \\ 0 & \cos(2\alpha) & -\sin(2\alpha) & 0 \\ 0 & \sin(2\alpha) & \cos(2\alpha) & 0 \\ 0 & 0 & 0 & 1 \end{bmatrix}, \qquad \text{(A.15)}$$

where α is the angle of rotation. A MM in one basis a is rotated to another basis b by $\mathbf{M}_b = \mathbf{R}(\alpha_o)\mathbf{M}_a\mathbf{R}(\alpha_i)$, where α_i and is the angle from the input basis of b to the input basis of a, and α_o is the angle from the output basis of a to the output basis of b.

A.3.1 Polarimeter Basis

The polarimeter basis vectors are defined using a double-pole coordinate system. A set of reference polarization basis vectors are defined for the on-axis rays and parallel transport is used to determine the basis vectors for other ray directions. With the object centered

at the origin, the illumination and observation axis directions, $\widehat{\mathbf{a}}_i$ and $\widehat{\mathbf{a}}_o$, respectively, are calculated

$$\widehat{\mathbf{a}}_i = -\frac{\mathbf{r}_{src}}{\|\mathbf{r}_{src}\|} \quad \text{and} \quad \widehat{\mathbf{a}}_o = \frac{\mathbf{r}_{cam}}{\|\mathbf{r}_{cam}\|}. \tag{A.16}$$

A $3{\times}3$ rotation matrix is used to perform the parallel transport. The rotation matrix $\mathbf{R}_3$ for an angle ϕ about the axis $\widehat{\mathbf{r}} = (r_x, r_y, r_z)$ is calculated

$$\mathbf{R}_3(\widehat{\mathbf{r}}, \phi) = \begin{bmatrix} r_x^2(1 - \cos\phi) + \cos\phi & r_x r_y(1 - \cos\phi) - r_z\sin\phi & r_x r_z(1 - \cos\phi) + r_y\sin\phi \\ r_y r_x(1 - \cos\phi) + r_z\sin\phi & r_y^2(1 - \cos\phi) + \cos\phi & r_y r_z(1 - \cos\phi) - r_x\sin\phi \\ r_z r_x(1 - \cos\phi) - r_y\sin\phi & r_z r_y(1 - \cos\phi) + r_x\sin\phi & r_z^2(1 - \cos\phi) + \cos\phi. \end{bmatrix} \tag{A.17}$$

The rotation axis and angle, $\widehat{\mathbf{r}}_i$ and ϕ_i, respectively, for transforming the PSG reference basis are calculated

$$\widehat{\mathbf{r}}_i = \frac{\widehat{\mathbf{a}}_i \times \widehat{\boldsymbol{\omega}}_i}{\|\widehat{\mathbf{a}}_i \times \widehat{\boldsymbol{\omega}}_i\|} \quad \text{and} \quad \phi_i = \arccos(\widehat{\boldsymbol{\omega}}_i \cdot \widehat{\mathbf{a}}_i). \tag{A.18}$$

Similarly, the rotation axis and angle, $\widehat{\mathbf{r}}_o$ and ϕ_o, respectively, for transforming the PSA reference basis are calculated

$$\widehat{\mathbf{r}}_o = \frac{\widehat{\mathbf{a}}_o \times \widehat{\boldsymbol{\omega}}_o}{\|\widehat{\mathbf{a}}_o \times \widehat{\boldsymbol{\omega}}_o\|} \quad \text{and} \quad \phi_o = \arccos(\widehat{\boldsymbol{\omega}}_o \cdot \widehat{\mathbf{a}}_o). \tag{A.19}$$

Both $\widehat{\boldsymbol{\omega}}_i$ and $\widehat{\boldsymbol{\omega}}_o$ vary per-pixel in an image, therefore $\widehat{\mathbf{r}}_i$, ϕ_i, $\widehat{\mathbf{r}}_o$ and ϕ_o all vary per-pixel as well.

The reference polarization basis vectors for the PSG and PSA must be perpendicular to $\widehat{\mathbf{a}}_i$ and $\widehat{\mathbf{a}}_o$, respectively. If the source and camera rotate about the origin in the x-z plane, then a convenient choice the vertical polarization reference vectors for the PSG and PSA is simply $\widehat{\mathbf{y}} = (0, 1, 0)$. The vertical polarization basis vector for the PSG and PSA, $\widehat{\mathbf{y}}_{PSG}$ and $\widehat{\mathbf{y}}_{PSA}$ respectively, at each pixel are then calculated

$$\widehat{\mathbf{y}}_{PSG} = \mathbf{R}_3(\widehat{\mathbf{r}}_i, \theta_i)\widehat{\mathbf{y}} \quad \text{and} \quad \widehat{\mathbf{y}}_{PSA} = \mathbf{R}_3(\widehat{\mathbf{r}}_o, \theta_o)\widehat{\mathbf{y}}. \tag{A.20}$$

For each ray, the horizontal basis vectors are found

$$\widehat{\mathbf{x}}_{PSG} = \widehat{\mathbf{y}}_{PSG} \times \widehat{\boldsymbol{\omega}}_i \quad \text{and} \quad \widehat{\mathbf{x}}_{PSA} = \widehat{\mathbf{y}}_{PSA} \times \widehat{\boldsymbol{\omega}}_o. \tag{A.21}$$

A.3.2 Local and Microfacet Bases

The local and microfacet bases are similar as they are both defined relative to planes of incidence and exitance. The polarization basis vectors are those in the transverse plane which are parallel and perpendicular to the planes of incidence or exitance. The polarization basis vectors are in the transverse plane and either perpendicular to the incident/exitant plane (s-polarization) or parallel to the incident/exitant plane (p-polarization).

For the local basis, the incident and exitant planes contain the surface normal $\widehat{\mathbf{n}}$. The vectors $\widehat{\boldsymbol{\omega}}_i, \widehat{\boldsymbol{\omega}}_o$, and $\widehat{\mathbf{n}}$ are generally non-coplanar so the incident and exitant planes must be treated separately. The s-polarization directions, which are used as horizontal polarization by convention, are calculated

$$\widehat{\mathbf{s}}_i = \frac{\widehat{\boldsymbol{\omega}}_i \times \widehat{\mathbf{n}}}{\|\widehat{\boldsymbol{\omega}}_i \times \widehat{\mathbf{n}}\|} \quad \text{and} \quad \widehat{\mathbf{s}}_o = \frac{\widehat{\mathbf{n}} \times \widehat{\boldsymbol{\omega}}_o}{\|\widehat{\mathbf{n}} \times \widehat{\boldsymbol{\omega}}_o\|}. \tag{A.22}$$

The p-polarization basis vectors are mutually perpendicular with the ray direction and s-direction, so they are calculated

$$\widehat{\mathbf{p}}_i = \widehat{\boldsymbol{\omega}}_i \times \widehat{\mathbf{s}}_i \quad \text{and} \quad \widehat{\mathbf{p}}_o = \widehat{\boldsymbol{\omega}}_o \times \widehat{\mathbf{s}}_o. \tag{A.23}$$

The microfacet basis is calculated similarly to the local basis using Eqs. A.22 and A.23, with the exception that in Eq. A.22, the surface normal $\widehat{\mathbf{n}}$ is replaced with the halfway vector $\widehat{\mathbf{h}}$, which serves as the surface normal for the hypothetical microfacet. The vectors $\widehat{\boldsymbol{\omega}}_i, \widehat{\boldsymbol{\omega}}_o$, and $\widehat{\mathbf{h}}$ are all coplanar, so $\widehat{\mathbf{s}}_i$ and $\widehat{\mathbf{s}}_o$ are parallel.

APPENDIX B

Linear Correlation Coefficient Optimization of Mixed Polarized Reflection Model

As shown in Chapter 3, the polarimetric measurement of the ideal depolarizer is constant $\mathbf{aM}_{ID}\mathbf{g} = \frac{1}{2}$, regardless of the PSG and PSA states. Any variations in polarimetric measurement P of a TD-MM are due to the dominant MJM term. Therefore, the individual polarimetric measurements P_n of a TD-MM, (*i.e.*, the elements of the flux vector from Chapter 6) are linearly related to the polarimetric measurements $P_{n,0}$ of the MJM. Using the notation of Eqs. 6.2 and 6.3, this is written

$$\mathbf{P} = \beta_0\mathbf{P}_0 + \frac{\beta_{ID}}{2} \tag{B.1}$$

The slope and offset of the linear relation, β_0 and $\beta_{ID}/2$, respectively, depend on ξ_0 and M_{00}, which in turn each depend on scattering geometry. However the material constants n_λ, a_λ, and b_λ are assumed to be geometry-independent. Therefore, n_λ, a_λ, and b_λ could be globally tuned to optimize the linear fit of $\mathbf{P}$ to $\mathbf{P}_0$ across the pixel-dependent scattering geometry simultaneously. This method is appealing because the linearity of $\mathbf{P}$ versus $\mathbf{P}_0$ can be assessed with fewer than 16 polarimetric measurements. In other words, the material parameters in the mixed polarization model can be estimated using partial polarimetry. Being able to determine the MJM model, $\widetilde{\xi}_0$, and $\widetilde{M}_{00}$ from the same set of partial polarimetric measurements would enable the extrapolation of a MM as described in Chapter 6 with less assumed prior knowledge.

 A preliminary demonstration of this method was performed on the MM images in Dataset 3.[37] The material constants which maximized the linear correlation coefficient are shown in Tab. B.1. These optimized constants produced correlation coefficients of 0.8693 and 0.7677 for measurements performed at 451 nm and 662 nm, respectively. These correlation coefficients are larger than those for the *ad hoc* material constants, which were 0.8390 and 0.7328 for 451 nm and 662 nm, respectively. This means that the optimization

Table B.1: Material constants optimized to match the models to the observed MM measurements. These parameters are constant with respect to scattering geometry.

Material constants	451 nm	662 nm
$n_\lambda + i\kappa_\lambda$	$1.92367 - i0.112273$	$0.393544 - i1.07656$
a_λ	0.201423	1.28083
b_λ	6.99784	5.38966

found solutions which improved agreement between measurements and the model, as far as this particular figure of merit.

Figures B.1 and B.2 show a comparison of ground truth MJM images for a red sphere determined by analyzing DRR measurements versus the mixed polarization model using *ac hoc* and optimized material constants at $\Omega = 65°$ and $\Omega = 20°$, respectively. At $\Omega = 65°$, the *ad hoc* model has significant erroneous values in the m_{32} and m_{23} elements which the optimized model does not. For any polarimetric measurements which involve elliptical PSG/PSA states, this may cause meaningful errors. Conversely, the optimized model at 662 nm introduces greater deviation in the m_{31}, m_{13}, m_{32}, and m_{23} elements which were not present in the *ad hoc* model. For the range of scattering geometries present in the image of a sphere at $\Omega = 65°$, the optimized model agrees with the measurement at 451 nm more than 662 nm.

At $\Omega = 20°$, the sign and magnitude errors at 662 nm in the m_{31}, m_{13}, m_{32}, and m_{23} elements persist. There is also large disagreement in diattenuation magnitude near the center of the sphere where θ_h is small, meaning that the large value of b_λ is suppressing the diffuse polarization term too much. The agreement between measurement and the optimized model at 451 nm is still better than at 662 nm, but the diattenuation magnitude increases rapidly at the edges of the sphere. This is again the result of the larger value of b_λ suppressing the diffuse term where θ_h is small, but rapidly increasing the weight on diffuse when θ_h is large.

The variability in agreement between the measured MJM and the optimized model MJM suggests that, while the optimized material parameters maximize the linearity of $\mathbf{P}$ to $\mathbf{P}_0$ over all geometries, better agreement may be achieved by not considering the

Figure B.1: MJM images of the red sphere at (a-c) 451 nm and (d-f) 662 nm at $\Omega = 65°$. The different MJMs are (a,d) the dominant MJM from DRR measurements and the models (see Eq. 5.3) using (b,e) the *ad hoc* material constants in Tab. 5.1 and (c,f) the optimized material constants in Tab. B.1.

material parameters to be constant. The degree to which the material parameters may be considered constant depends on the accuracy requirement for any given application.

(a) Measured 451 nm   (b) Ad hoc model 451 nm   (c) Optimized model 451 nm

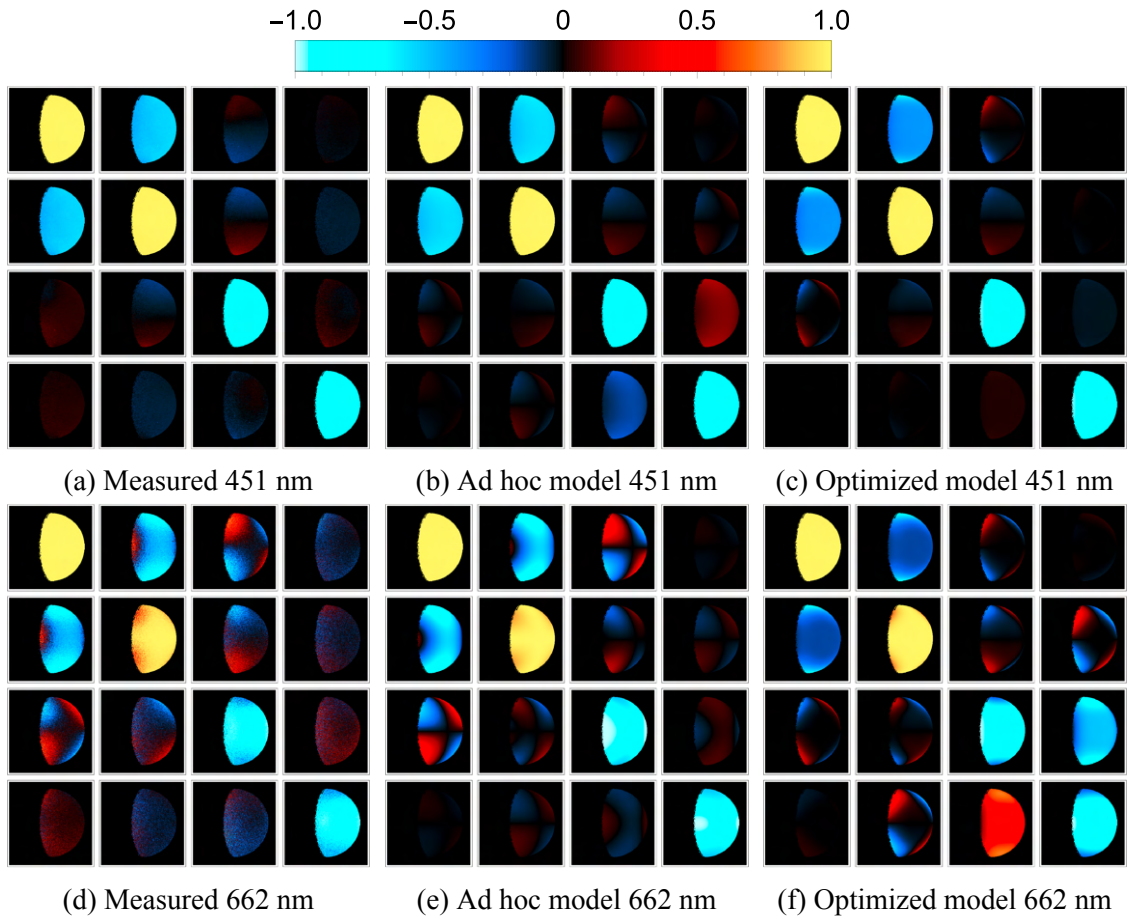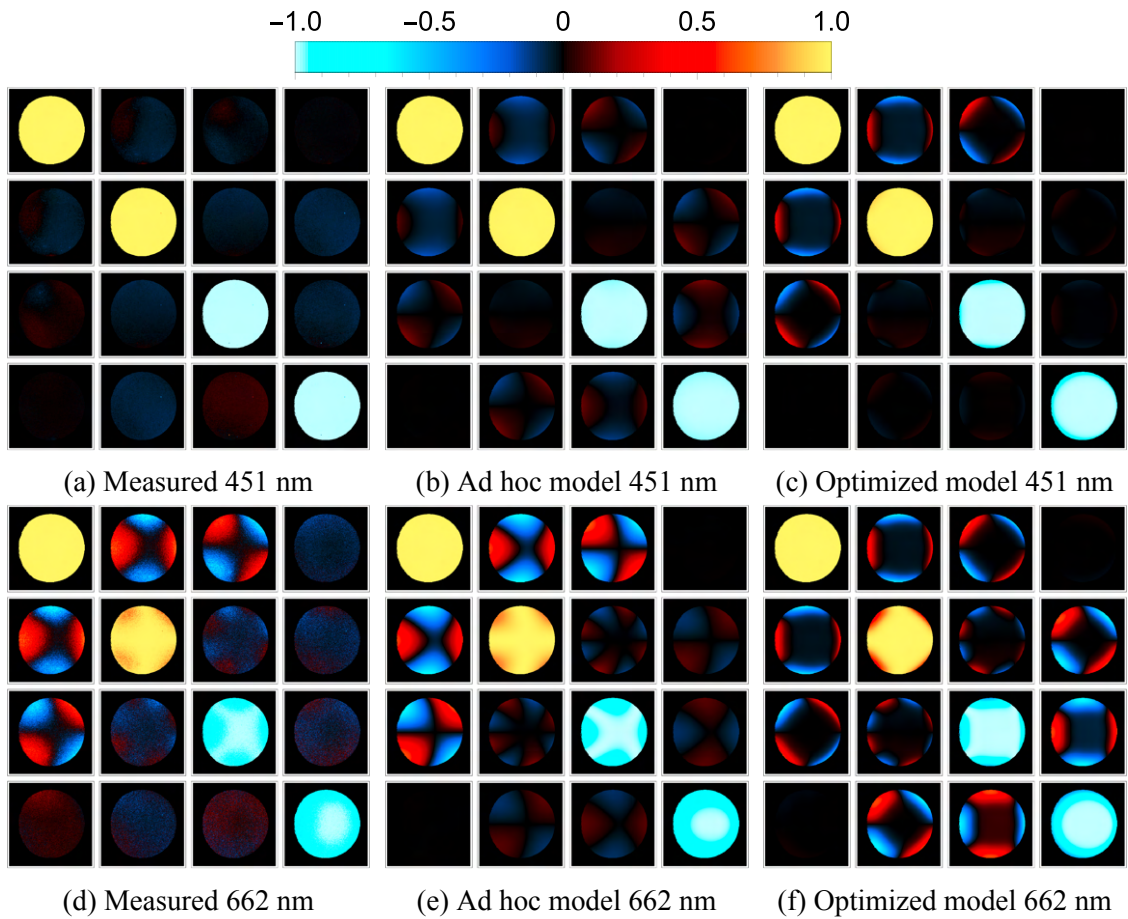(d) Measured 662 nm   (e) Ad hoc model 662 nm   (f) Optimized model 662 nm

Figure B.2: MJM images of the red sphere at (a-c) 451 nm and (d-f) 662 nm at $\Omega = 20°$. The different MJMs are (a,d) the dominant MJM from DRR measurements and the models (see Eq. 5.3) using (b,e) the *ad hoc* material constants in Tab. 5.1 and (c,f) the optimized material constants in Tab. B.1.

REFERENCES

[1] Arteaga, O., and Ossikovski, R. Complete Mueller matrix from a partial polarimetry experiment: the 12-element case. *J. Opt. Soc. Am. A 36*, 3 (Mar 2019), 416–427.

[2] Ashcraft, J. N., Douglas, E. S., Kim, D., Riggs, A. J. E., Anche, R., Brendel, T., Derby, K., Dube, B. D., Jarecki, Q., Jenkins, E., and Milani, K. S. Poke: an open-source, ray-based physical optics platform. In *Optical Modeling and Performance Predictions XIII* (2023), M. A. Kahan, Ed., vol. 12664, International Society for Optics and Photonics, SPIE, p. 1266404.

[3] Ashikmin, M., Premože, S., and Shirley, P. A microfacet-based BRDF generator. In *Proceedings of the 27th annual conference on Computer graphics and interactive techniques* (2000), pp. 65–74.

[4] Atkinson, G., and Hancock, E. Recovery of surface orientation from diffuse polarization. *IEEE transactions on image processing 15*, 6 (2006), 1653–1664.

[5] Azzam, R. M. A. Photopolarimetric measurement of the Mueller matrix by fourier analysis of a single detected signal. *Optics Letters 2*, 6 (Jun 1978), 148.

[6] Ba, Y., Gilbert, A., Wang, F., Yang, J., Chen, R., Wang, Y., Yan, L., Shi, B., and Kadambi, A. Deep shape from polarization. In *Computer Vision – ECCV 2020* (2020), A. Vedaldi, H. Bischof, T. Brox, and J.-M. Frahm, Eds., Springer International Publishing, pp. 554–571.

[7] Baek, S.-H., Jeon, D. S., Tong, X., and Kim, M. H. Simultaneous acquisition of polarimetric SVBRDF and normals. *ACM Trans. Graph. 37*, 6 (2018).

[8] Baek, S.-H., Zeltner, T., Ku, H. J., Hwang, I., Tong, X., Jakob, W., and Kim, M. H. Image-based acquisition and modeling of polarimetric reflectance. *ACM Trans. Graph. 39*, 4 (2020).

[9] Billings, B. H. A monochromatic depolarizer. *J. Opt. Soc. Am. 41*, 12 (Dec 1951), 966–975.

[10] Breon, F.-M., and Maignan, F. A BRDF–BPDF database for the analysis of earth target reflectances. *Earth System Science Data 9*, 1 (2017), 31–45.

[11] Brewster, D. III. Experiments on the depolarisation of light as exhibited by various mineral, animal, and vegetable bodies, with a reference of the phenomena to the general principles of polarisation. *Philosophical Transactions of the Royal Society of London 105* (1815), 29–53.

[12] Bréon, F. An analytical model for the cloud-free atmosphere/ocean system reflectance. *Remote sensing of environment 43*, 2 (1993), 179–192.

[13] Bueno, J. M. Measurement of parameters of polarization in the living human eye using imaging polarimetry. *Vision Research 40*, 28 (Dec. 2000), 3791–3799.

[14] Chipman, R., Lam, W., and Young, G. *Polarized Light and Optical Systems*. Optical Sciences and Applications of Light. CRC Press, 2018.

[15] Chipman, R. A. Mechanics of polarization ray tracing. *Optical Engineering 34*, 6 (1995), 1636–1645.

[16] Chipman, R. A. Metrics for depolarization. In *Polarization Science and Remote Sensing II* (2005), J. A. Shaw and J. S. Tyo, Eds., vol. 5888, International Society for Optics and Photonics, SPIE, p. 58880L.

[17] Chipman, R. A. Degrees of freedom in depolarizing Mueller matrices. In *Polarization Science and Remote Sensing III* (2007), J. A. Shaw and J. S. Tyo, Eds., vol. 6682, International Society for Optics and Photonics, SPIE, p. 66820I.

[18] Chipman, R. A., and Lam, W. S. T. The Polaris-M ray tracing program. In *Polarization Science and Remote Sensing VII* (2015), vol. 9613, SPIE, p. 96130J–96130J–18. Conference Location: San Diego, California, United States.

[19] Clarke, F., and Parry, D. Helmholtz reciprocity: its validity and application to reflectometry. *Lighting Research & Technology 17*, 1 (1985), 1–11.

[20] Cloude, S. R. Group theory and polarisation algebra. *Optik 75* (1986), 26–36.

[21] Cloude, S. R. Conditions for the physical realisability of matrix operators in polarimetry. In *Polarization Considerations for Optical Systems II* (1990), R. A. Chipman, Ed., vol. 1166, International Society for Optics and Photonics, SPIE, pp. 177 – 187.

[22] Cloude, S. R., and Pottier, E. Concept of polarization entropy in optical scattering. *Optical Engineering 34*, 6 (1995), 1599 – 1610.

[23] Compain, E., Poirier, S., and Drevillon, B. General and self-consistent method for the calibration of polarization modulators, polarimeters, and Mueller-matrix ellipsometers. *Applied optics 38*, 16 (1999), 3490–3502.

[24] Cui, Z., Gu, J., Shi, B., Tan, P., and Kautz, J. Polarimetric multi-view stereo. In *2017 IEEE Conference on Computer Vision and Pattern Recognition (CVPR)* (2017), pp. 369–378.

[25] DeBoo, B. J., Sasian, J. M., and Chipman, R. A. Depolarization of diffusely reflecting man-made objects. *Appl. Opt. 44*, 26 (Sep 2005), 5434–5445.

[26] Dupuy, J., and Jakob, W. An adaptive parameterization for efficient material acquisition and rendering. *ACM Transactions on Graphics 37*, 6 (Dec. 2018), 1–14.

[27] Fanjul-Vélez, F., Pircher, M., Baumann, B., Götzinger, E., Hitzenberger, C. K., and Arce-Diego, J. L. Polarimetric analysis of the human cornea measured by polarization-sensitive optical coherence tomography. *Journal of Biomedical Optics 15*, 5 (2010), 056004.

[28] Germann, J. A., Martinez-Enriquez, E., and Marcos, S. Quantization of collagen organization in the stroma with a new order coefficient. *Biomed. Opt. Express 9*, 1 (Jan 2018), 173–189.

[29] Germann, J. A., Martínez-Enríquez, E., Martínez-García, M. C., Kochevar, I. E., and Marcos, S. Corneal Collagen Ordering After In Vivo Rose Bengal and Riboflavin Cross-Linking. *Investigative Ophthalmology & Visual Science 61*, 3 (03 2020), 28–28.

[30] Germer, T. A. pySCATMECH: a Python interface to the SCATMECH library of scattering codes. In *Reflection, Scattering, and Diffraction from Surfaces VII* (2020), L. M. Hanssen, Ed., vol. 11485, International Society for Optics and Photonics, SPIE, p. 114850J.

[31] Gil, J. J., and Bernabeu, E. Depolarization and polarization indices of an optical system. *Optica Acta: International Journal of Optics 33*, 2 (1986), 185–189.

[32] Gil Perez, J. J., and Ossikovski, R. *Polarized light and the Mueller matrix approach*, second edition. ed. CRC Press, 2022.

[33] Goudail, F., and Bénière, A. Optimization of the contrast in polarimetric scalar images. *Optics Letters 34*, 9 (May 2009), 1471.

[34] Heitz, E. Understanding the masking-shadowing function in microfacet-based BRDFs. *Journal of Computer Graphics Techniques Vol 3*, 2 (2014).

[35] Huang, T., Meng, R., Qi, J., Liu, Y., Wang, X., Chen, Y., Liao, R., and Ma, H. Fast Mueller matrix microscope based on dual DoFP polarimeters. *Opt. Lett. 46*, 7 (Apr 2021), 1676–1679.

[36] Jarecki, Q., and Kupinski, M. Extrapolating Mueller matrices from linear Stokes images. In *Polarization: Measurement, Analysis, and Remote Sensing XV* (2022), D. B. Chenault and M. K. Kupinski, Eds., vol. 12112, International Society for Optics and Photonics, SPIE, p. 121120D.

[37] Jarecki, Q., and Kupinski, M. Data for "efficient modeling of depolarizing Mueller BRDFs", 2023. https://dx.doi.org/10.21227/3q77-z917.

[38] Jarecki, Q., and Kupinski, M. Optimizing near-infrared polariscopic imaging for the living human eye. *Opt. Express 32*, 10 (May 2024), 18113–18126.

[39] Jarecki, Q., and Kupinski, M. Polarized representation for depolarization-dominant materials. *Opt. Express 32*, 5 (Feb 2024), 8262–8283.

[40] Jarecki, Q., and Kupinski, M. K. Underdetermined polarimetric measurements for Mueller extrapolations. *Optical Engineering 61*, 12 (2022), 123104.

[41] Jarecki, Q. T., and Kupinski, M. K. Compact tabulation of isotropic polarized scattering, 5 2024. DOI: 10.25422/azu.data.25769397.v1, Accessed: May 16, 2024.

[42] Jin, Y.-Q., and Cloude, S. Numerical eigenanalysis of the coherency matrix for a layer of random nonspherical scatterers. *IEEE Transactions on Geoscience and Remote Sensing 32*, 6 (1994), 1179–1185.

[43] Kadambi, A., Taamazyan, V., Shi, B., and Raskar, R. Polarized 3d: High-quality depth sensing with polarization cues. In *2015 IEEE International Conference on Computer Vision (ICCV)* (2015), pp. 3370–3378.

[44] Kalra, A., Taamazyan, V., Rao, S. K., Venkataraman, K., Raskar, R., and Kadambi, A. Deep polarization cues for transparent object segmentation. In *Proceedings of the IEEE/CVF Conference on Computer Vision and Pattern Recognition (CVPR)* (June 2020).

[45] Kondo, Y., Ono, T., Sun, L., Hirasawa, Y., and Murayama, J. Accurate polarimetric BRDF for real polarization scene rendering. In *European Conference on Computer Vision* (2020), Springer, pp. 220–236.

[46] Kupinski, M., Boffety, M., Goudail, F., Ossikovski, R., Pierangelo, A., Rehbinder, J., Vizet, J., and Novikova, T. Polarimetric measurement utility for pre-cancer detection from uterine cervix specimens. *Biomed. Opt. Express 9*, 11 (Nov 2018), 5691–5702.

[47] Kupinski, M., Bradley, C., Diner, D., Xu, F., and Chipman, R. Applying a microfacet model to polarized light scattering measurements of the Earth's surface. In *Polarization Science and Remote Sensing VII* (2015), J. A. Shaw and D. A. LeMaster, Eds., vol. 9613, International Society for Optics and Photonics, SPIE, p. 96130T.

[48] Kupinski, M., Bradley, C., Diner, D., Xu, F., and Chipman, R. Estimating surface orientation from microfacet Mueller matrix bidirectional reflectance distribution

function models in outdoor passive imaging polarimetry. *Optical Engineering 58*, 8 (2019), 082416.

[49] Kupinski, M. K., Bankhead, J., Stohn, A., and Chipman, R. Binary classification of Mueller matrix images from an optimization of Poincaré coordinates. *Journal of the Optical Society of America A 34*, 6 (June 2017), 983.

[50] Kupinski, M. K., Bradley, C. L., Diner, D. J., Xu, F., and Chipman, R. A. Angle of linear polarization images of outdoor scenes. *Optical Engineering 58*, 8 (2019), 1 – 12.

[51] Lam, W.-S. T., Chipman, R. A., Twietmeyer, K. M., Zhou, Y., Denninghoff, K. R., Elsner, A. E., and Burns, S. A. Depolarization properties of the normal human fovea. In *Optical Coherence Tomography and Coherence Domain Optical Methods in Biomedicine XIII* (2009), J. G. Fujimoto, J. A. Izatt, and V. V. Tuchin, Eds., vol. 7168, International Society for Optics and Photonics, SPIE, p. 716829.

[52] Lam, W.-S. T., Chipman, R. A., Twietmeyer, K. M., Zhou, Y., Denninghoff, K. R., Elsner, A. E., and Burns, S. A. Depolarization properties of the normal human fovea measured by the GDx-MM. In *Polarization Science and Remote Sensing IV* (2009), J. A. Shaw and J. S. Tyo, Eds., vol. 7461, International Society for Optics and Photonics, SPIE, p. 74610D.

[53] Leroy, M. Deviation from reciprocity in bidirectional reflectance. *Journal of Geophysical Research: Atmospheres 106*, D11 (2001), 11917–11923.

[54] Li, D., Ma, D., Guo, K., and Guo, Z. Polarization characteristics motivating target detection in different polarization spaces. *Optics & Laser Technology 171* (Apr. 2024), 110430.

[55] Li, L., and Kupinski, M. Merit functions and measurement schemes for single parameter depolarization models. *Opt. Express 29*, 12 (Jun 2021), 18382–18407.

[56] Li, X., Goudail, F., and Chen, S.-C. Self-calibration for Mueller polarimeters based on dofp polarization imagers. *Opt. Lett. 47*, 6 (Mar 2022), 1415–1418.

[57] Liang, J., Tian, X., Tu, X., Spires, O., Brock, N., Wang, D., Wu, H., Ren, L., Yao, B., Pau, S., and Liang, R. Color full Stokes polarization fringe projection 3d imaging. *Optics and Lasers in Engineering 130* (2020), 106088.

[58] López-Téllez, J. M., Chipman, R. A., Li, L. W., McEldowney, S. C., and Smith, M. H. Broadband extended source imaging Mueller-matrix polarimeter. *Opt. Lett. 44*, 7 (Apr 2019), 1544–1547.

[59] Lu, S.-Y., and Chipman, R. A. Interpretation of Mueller matrices based on polar decomposition. *J. Opt. Soc. Am. A 13*, 5 (May 1996), 1106–1113.

[60] Marschner, S. R., Westin, S. H., Lafortune, E. P. F., and Torrance, K. E. Image-based bidirectional reflectance distribution function measurement. *Applied Optics 39*, 16 (June 2000), 2592.

[61] Matusik, W., Pfister, H., Brand, M., and McMillan, L. A data-driven reflectance model. Association for Computing Machinery. doi:10.1145/882262.882343.

[62] Matusik, W., Pfister, H., Brand, M., and McMillan, L. *Efficient Isotropic BRDF Measurement*. Eurographics Association, 2003. http://portal.acm.org/citation.cfm?id=882439.

[63] Mccafferty, S. J., Schwiegerling, J. T., Koch, T. L., and Wyant, J. *Analysis and Application of Opto-Mechanics to the Etiology of Sub-Optimal Outcomes in Laser Corrective Eye Surgery and Design Methodology of Deformable Surface Accommodating Intraocular Lenses*. The University of Arizona., 2015.

[64] Miyazaki, D., and Ikeuchi, K. Shape estimation of transparent objects by using inverse polarization ray tracing. *IEEE transactions on pattern analysis and machine intelligence 29*, 11 (2007), 2018–2030. ObjectType-Article-2.

[65] Newton, R. H., and Meek, K. M. The integration of the corneal and limbal fibrils in the human eye. *Biophysical Journal 75*, 5 (Nov. 1998), 2508–2512.

[66] Nimier-David, M., Vicini, D., Zeltner, T., and Jakob, W. Mitsuba 2: A retargetable forward and inverse renderer. *Transactions on Graphics (Proceedings of SIGGRAPH Asia) 38*, 6 (12 2019).

[67] Noble, H., Lam, W.-S., and Chipman, R. A. Inferring the orientation of texture from polarization parameters. In *Polarization Science and Remote Sensing IV* (2009), J. A. Shaw and J. S. Tyo, Eds., vol. 7461, International Society for Optics and Photonics, SPIE, p. 746109.

[68] Noble, H. D., and Chipman, R. A. Mueller matrix roots algorithm and computational considerations. *Opt. Express 20*, 1 (Jan 2012), 17–31.

[69] Noble, H. D., McClain, S. C., and Chipman, R. A. Mueller matrix roots depolarization parameters. *Appl. Opt. 51*, 6 (Feb 2012), 735–744.

[70] Novikova, T., and Ramella-Roman, J. C. Is a complete Mueller matrix necessary in biomedical imaging? *Opt. Lett. 47*, 21 (Nov 2022), 5549–5552.

[71] Novikova, T., Ramella-Roman, J. C., Felger, L., Gros, R., Hewer, E., Maragkou, T., McKinley, R., Moriconi, S., Murek, M., Pierangelo, A., nez, O. R.-N., Zubak, I., and Schucht, P. Partial Mueller polarimetry for the complete optical diagnosis of biological tissue. In *Emerging Technologies for Cell and Tissue Characterization II* (2023), Optica Publishing Group, p. 1262902.

[72] Omer, K., and Kupinski, M. Compression, interpolation, and importance sampling for polarized BRDF models. *Opt. Express 30*, 14 (Jul 2022), 25734–25752.

[73] Ossikovski, R., and Arteaga, O. Integral decomposition and polarization properties of depolarizing Mueller matrices. *Opt. Lett. 40*, 6 (Mar 2015), 954–957.

[74] Ossikovski, R., and Arteaga, O. Complete Mueller matrix from a partial polarimetry experiment: the nine-element case. *J. Opt. Soc. Am. A 36*, 3 (Mar 2019), 403–415.

[75] Ossikovski, R., and Vizet, J. Eigenvalue-based depolarization metric spaces for Mueller matrices. *J. Opt. Soc. Am. A 36*, 7 (Jul 2019), 1173–1186.

[76] Pandolfi, A., and Manganiello, F. A model for the human cornea: Constitutive formulation and numerical analysis. *Biomechanics and modeling in mechanobiology 5* (12 2006), 237–46.

[77] Pau, S., Hsu, W.-L., Davis, J., Tu, X., Brock, N., Kroto, S., and Ibn-Elhaj, M. Full Stokes imaging polarimeter. In *Frontiers in Optics 2015* (2015), Optica Publishing Group, p. FW5D.1.

[78] Pircher, M., Goetzinger, E., Leitgeb, R., and Hitzenberger, C. K. Transversal phase resolved polarization sensitive optical coherence tomography. *Physics in Medicine and Biology 49*, 7 (Apr. 2004), 1257–1263.

[79] Pircher, M., Hitzenberger, C. K., and Schmidt-Erfurth, U. Polarization sensitive optical coherence tomography in the human eye. *Progress in Retinal and Eye Research 30*, 6 (Nov. 2011), 431–451.

[80] Priest, R., and Germer, T. *Polarimetric BRDF in the Microfacet Model: Theory and Measurements*. Proceedings of the Military Sensing Symposia (MSS) Specialty Group Meeting on Passive Sensors, Undefined, 2000-03-01 00:03:00 2000.

[81] Ramella-Roman, J. C., Saytashev, I., and Piccini, M. A review of polarization-based imaging technologies for clinical and preclinical applications. *Journal of Optics 22*, 12 (nov 2020), 123001.

[82] Rodríguez-Núñez, O., and Novikova, T. Polarimetric techniques for the structural studies and diagnosis of brain. *Advanced Optical Technologies 11*, 5-6 (2022), 157–171.

[83] Rubin, N. A., Chevalier, P., Juhl, M., Tamagnone, M., Chipman, R., and Capasso, F. Imaging polarimetry through metasurface polarization gratings. *Opt. Express 30*, 6 (Mar 2022), 9389–9412.

[84] Rusinkiewicz, S. M. *A New Change of Variables for Efficient BRDF Representation*. Springer Vienna, Vienna, 2011, p. 11–22.

[85] Schönhofer, A., and Kuball, H.-G. Symmetry properties of the mueller matrix. *Chemical Physics 115*, 2 (1987), 159–167.

[86] Sekera, Z. Scattering matrices and reciprocity relationships for various representations of the state of polarization. *J. Opt. Soc. Am. 56*, 12 (Dec 1966), 1732–1740.

[87] Sheppard, C. J. R. Parameterization of the Mueller matrix. *J. Opt. Soc. Am. A 33*, 12 (Dec 2016), 2323–2332.

[88] Sheppard, C. J. R., Gratiet, A. L., and Diaspro, A. Factorization of the coherency matrix of polarization optics. *J. Opt. Soc. Am. A 35*, 4 (Apr 2018), 586–590.

[89] Smith, M. H. Optimization of a dual-rotating-retarder Mueller matrix polarimeter. *Applied Optics 41*, 13 (2002), 2488–2493.

[90] Sobczak, M., and Asejczyk, M. Birefringent properties of the cornea measured by a Mueller type polarimeter in healthy adults and children. *Biomedical Optics Express 12*, 12 (Dec. 2021), 7872.

[91] Sobczak, M., Asejczyk, M., and Wilczyński, M. The effect of pupil size on the measurement of corneal birefringence properties: preliminary study. *Scientific Reports 13*, 1 (Oct. 2023), 17439.

[92] Sobczak, M., Asejczyk-Widlicka, M., Szafraniec, A., and Kurzynowski, P. Analysis of torsional eye movements using the corneal birefringence pattern. *Journal of the Optical Society of America A 36*, 4 (Apr. 2019), B23.

[93] Sobczak, M., Owczarek, M., Woźniak, W. A., and Kurzynowski, P. In vivo measurements of corneal birefringence properties using the one-way reflective Mueller polarimetry. *Optics Express 29*, 10 (May 2021), 15356.

[94] Stanworth, A., and Naylor, E. J. The polarization optics of the isolated cornea. *British Journal of Ophthalmology 34*, 4 (1950), 201–211.

[95] Swami, M., Patel, H., and Gupta, P. Conversion of 3×3 Mueller matrix to 4×4 Mueller matrix for non-depolarizing samples. *Optics Communications 286* (2013), 18–22.

[96] Tai, A., Jarecki, Q., and Kupinski, M. Near-infrared human eye Mueller matrix images. DOI: 10.25422/azu.data.24722358, Accessed: Dec. 4, 2023.

[97] Torrance, K. E., and Sparrow, E. M. Theory for off-specular reflection from roughened surfaces. *J. Opt. Soc. Am. 57*, 9 (Sep 1967), 1105–1114.

[98] Tu, X., McEldowney, S., Zou, Y., Smith, M., Guido, C., Brock, N., Miller, S., Jiang, L., and Pau, S. Division of focal plane red–green–blue full-stokes imaging polarimeter. *Appl. Opt. 59*, 22 (Aug 2020), G33–G40.

[99] Tu, X., Spires, O. J., Tian, X., Brock, N., Liang, R., and Pau, S. Division of amplitude RGB full-Stokes camera using micro-polarizer arrays. *Opt. Express 25*, 26 (Dec 2017), 33160–33175.

[100] Twietmeyer, K., and Chipman, R. Condition number as a metric for the effectiveness of polarimetric algorithms. In *Frontiers in Optics* (2005), Optica Publishing Group, p. FMB5.

[101] Twietmeyer, K. M., and Chipman, R. A. Optimization of Mueller matrix polarimeters in the presence of error sources. *Opt. Express 16*, 15 (Jul 2008), 11589–11603.

[102] Tyo, J. S. Design of optimal polarimeters: maximization of signal-to-noise ratio and minimization of systematic error. *Applied optics 41*, 4 (2002), 619–630.

[103] Umow, v. N. Chromatische depolarisation durch lichtzerstreuung. *Physikalische Zeitschrift 6*, 20 (1905), 674–676.

[104] Upadhyay, D., Mondal, S., Lacot, E., and Orlik, X. Full analytical solution of adapted polarisation state contrast imaging. *Optics Express 19*, 25 (Dec. 2011), 25188.

[105] Walter, B., Marschner, S. R., Li, H., and Torrance, K. E. Microfacet models for refraction through rough surfaces. *Rendering techniques 2007* (2007), 18th.

[106] Wolff, L. Using polarization to separate reflection components. In *1989 IEEE Computer Society Conference on Computer Vision and Pattern Recognition* (Jun 1989), IEEE Computer Society, pp. 363–369.

[107] Wolff, L. B. Diffuse-reflectance model for smooth dielectric surfaces. *J. Opt. Soc. Am. A 11*, 11 (Nov 1994), 2956–2968.

[108] Wu, X., Li, P., Zhang, X., Chen, J., and Huang, F. Three dimensional shape reconstruction via polarization imaging and deep learning. *Sensors 23*, 10 (2023).

[109] Yun, G., Chipman, R. A., Tyo, J. S., and Gmitro, A. *Polarization Ray Tracing*. PhD thesis, The University of Arizona., 2012.

[110] Yun, G., Crabtree, K., and Chipman, R. A. Three-dimensional polarization ray-tracing calculus I: definition and diattenuation. *Applied Optics 50*, 18 (2011), 2855.

[111] Yun, G., McClain, S. C., and Chipman, R. A. Three-dimensional polarization ray-tracing calculus II: retardance. *Applied Optics 50*, 18 (2011), 2866.